3-2-2015

Verification of the dissipated energy based fatigue model using field data

Thomas Redles

VERIFICATION OF THE DISSIPATED ENERGY BASED FATIGUE MODEL USING FIELD DATA

by
Thomas A. Redles

A Thesis

Submitted to the
Department of Civil Engineering
College of Engineering
In partial fulfillment for the requirement
For the degree of
Master of Science in Civil Engineering
At
Rowan University
October 2014

Thesis Chair: Yusuf Mehta, Ph.D.

Dedication

I would like to dedicate this manuscript to my parents, professors, and friends

Acknowledgements

I would like to thank Dr. Yusuf Mehta and Dr. Ayman Ali from Rowan University, as well as Dr. David Brill and Dr. Navneet Garg from the Federal Aviation Administration (FAA), and Dr. Injun Song from SRA International, for their assistance in my work. I would also like to thank my thesis committee, including Dr. Douglas Cleary. Although this project has been sponsored by the FAA, it should be known that the contents of the thesis reflect the views of the author, who is responsible for the facts and accuracy of the data presented within. The contents do not necessarily reflect the official views and policies of the FAA. The thesis does not constitute a standard, specification, or regulation.

Abstract

Thomas A. Redles
VERIFICATION OF THE DISSIPATED ENERGY BASED FATIGUE MODEL USING FIELD DATA
2013/14
Yusuf Mehta, Ph.D.
Master of Science in Civil Engineering

Damage can be limited to the top layer in perpetual pavements through the use of a very thick surface layer or a binder-rich intermediate layer. To achieve this goal, tensile strains at the bottom of the top hot-mix asphalt (HMA) layer must be limited to below a certain value known as the fatigue endurance limit (FEL). In this thesis, a method for estimating the allowable strain in the asphalt layers of flexible airfield pavements is proposed based on the concept that HMA fatigue failure is associated with a significant reduction in HMA layer modulus, usually taken as 50 percent. Falling Weight Deflectometer (FWD) testing results collected from flexible pavements at the FAA's National Airport Pavement Test Facility (NAPTF) were analyzed to determine the loading pass for each section that the HMA layer modulus was reduced by 50%. NAPTF tensile strain data was then used to determine the strain at the critical pass for each pavement section by averaging the two or three peaks in the strain profile at the critical loading pass. The proposed approach was validated by comparing the results to those obtained from Shen and Carpenter's Rate of Dissipated Energy Change (RDEC) model to estimate the theoretical N_{f50} tensile strain. In addition, it was also observed that the variability of peak tensile strain values increased at pass corresponding to a 50% reduction in HMA modulus, confirming that the proposed criterion in fact relates to observable damage.

Table of Contents

Table of Contents (Continued)

Table of Contents (Continued)

Table of Contents (Continued)

List of Figures

List of Tables

Chapter 1

Introduction

1.1 Problem Statement

The concept of perpetual pavements has been around since the 1990s. This concept was first introduced as a way to ensure that all damage happening in pavement structures is limited to the top several inches while the underlying pavement remains structurally intact. The goal of perpetual pavement construction is to limit rutting at the top of the HMA structure and limit fatigue cracking in the lower HMA layers. Since base layer failures ideally would not occur, perpetual pavements were expected to last 50 years or more with only occasional minor resurfacing [1]. One approach to limit damage only to the surface layer in perpetual pavements is by increasing the thickness of the hot-mix asphalt (HMA) layer. However, increasing the thickness of the HMA is very expensive and so another, more cost-efficient, method is used for perpetual pavement construction. This method involves the use of a rut-resistant layer that can withstand high compressive strains and a binder rich layer that can withstand high tensile strains. An example of this type of pavement construction is the Extended Life Hot-Mix Asphalt Pavement, or ELHMAP [2]. ELHMAP pavement consists of a highly rut-resistant top HMA layer (typically stone matrix asphalt, SMA, mix) above a traditional HMA layer which is laid on top of a binder-rich bottom HMA layer that is designed to resist fatigue failure.

The basis for designing perpetual pavements, however, is still uncertain. For example, the design of perpetual pavements involves determining how thick a binder-rich layer should be in order to withstand the repeated loading that leads to fatigue cracking. After reviewing the literature, it was discovered that fatigue damage can be limited to the

surface HMA layer in perpetual pavements by limiting the tensile strain at the bottom of the binder-rich layer below a specific value known as the fatigue endurance limit (FEL) [2]. The FEL is the strain level at which the number of loading cycles required to cause failure (i.e. a 50 percent reduction in modulus) is practically infinite. To determine a value for the FEL, researchers utilized the concept of dissipated energy to describe the fatigue behavior of viscoelastic materials such as asphalt mixtures [3] [4] [5]. Dissipated energy is defined as the energy consumed during a fatigue test, which can be determined based on the stress-strain curves for loading and unloading. The use of dissipated energy in these studies was based on the assumption that all dissipated energy produces damage in the material [6]. However, this assumption is not true, as not all dissipated energy contributes to damage, as some of the energy is instead dissipated in the form of heat, plasticity, and other forms, and does not contribute to damage. In a more recent study, Carpenter et al. [2] introduced the concept of rate of dissipated energy change (RDEC); which is a rate of change in dissipated energy between two consecutive loading cycles, defined as the ratio of the difference in dissipated energy between loading cycles n and $n+1$ to the dissipated energy in loading cycle n. In this study, it was observed that when RDEC is plotted versus number of loading cycles, the RDEC values reached a plateau value (PV) in the central portion of the curve [2] [6]. This plateau value was found to have a unique relationship with the number of cycles to failure that is independent of the mixture, loading type, and test condition [2] [6]. In addition, when plotting PV versus the flexural strain, non-linear behavior was observed at low strain values [2].

In the RDEC model developed by Carpenter et al., not all dissipated energy contributes to damage in the material. Shen and Carpenter [6] developed a refined RDEC

model where the RDEC, rather than the dissipated energy itself, is directly correlated to fatigue damage in the pavement [6]. Shen and Carpenter also related mixture material properties and loading effects to fatigue. The refined RDEC model related PV to mixture properties such as the volumetric and gradation properties, as well as stiffness. The log of PV was also related linearly to the log of the flexural tensile strain until the flexural tensile strain reaches below the FEL [2].

In summary, researchers agree that the concept of dissipated energy can be utilized to determine a tensile strain limiting value, or FEL, that can be used in the structural design of perpetual pavements [2] [3] [4] [5] [6]. The RDEC-based model developed by Shen and Carpenter [6] provides a promising approach for predicting the value of the limiting strain in flexible pavements. This model was validated using limited laboratory tests on mixes including NAPTF HMA mixes from Construction Cycle Six (CC6) [6]. These laboratory results might not be representative of actual field conditions. Therefore, there is a need to develop an approach to estimate HMA fatigue criteria based on the analysis of full-scale testing results. There is also a need to verify the accuracy of predictions made by the refined RDEC model and the proposed field-based approach. Construction Cycle Seven (CC7) at the NAPTF is currently being performed in order to examine the effects of these perpetual pavements. The NAPTF construction cycles analyzed in this study, which will be discussed further in Chapter 3, were not originally intended to produce fatigue failure [7]. The FAA believes that the earlier tests, which provided data mainly on subgrade (structural) failure, may, on a second look, yield additional data on HMA fatigue in full-scale airport pavements.

1.2 Study Objectives

The objectives of this study are listed below as follows:

- Develop an approach to estimate a limiting asphalt strain for airfield pavements based on fatigue concepts. This was accomplished utilizing data collected by the Federal Aviation Administration (FAA) at the National Airport Pavement Test Facility (NAPTF). Field data such Falling Weight Deflectometer (FWD) results and variability in peak strain profile data collected from the NAPTF website were analyzed.
- Compare the predictions made using the refined RDEC model and the proposed approach.
- Re-examine the earlier NAPTF Construction Cycles (CC1, CC3, and CC5) for data that contributes to an understanding of the perpetual pavement problem as it relates to airports.

1.3 Thesis Organization

This thesis is organized into seven chapters. In chapter one, the problem statement, objectives, and outline of the thesis are presented. In chapter two, an in-depth review of literature is presented. This review is pertinent to dissipated energy fatigue prediction models and pavement fatigue characterizations. In chapter three, the layout of construction cycles one, three, and five (CC1, CC3, and CC5) of the National Airport Pavement Test Facility (NAPTF) is discussed. In chapter four, a detailed discussion of the research approach and methodology is presented. In chapter five, the results of Falling Weight Deflectometer (FWD) testing are discussed. In chapter six, the results obtained from the analysis of FWD results are compared to results from the RDEC

model. Finally, chapter seven provides a summary and presents the conclusions and recommendations made.

Chapter 2

Review of Literature

2.1 Introduction

This chapter includes a comprehensive discussion of previous studies pertinent to dissipated energy, fatigue endurance limits, and ratio of dissipated energy change. In addition, the Falling Weight Deflectometer (FWD) and back-calculation procedure implemented in this study are also presented in this chapter.

Specifically, the most commonly used laboratory tests that are typically performed to characterize fatigue cracking are presented. The major pavement fatigue prediction models are presented. These include: (1) the phenomenological model, (2) the continuum damage model, (3) the fracture mechanics model, and (4) the Rate of Dissipated Energy Change (RDEC) model. Finally, a discussion of the Falling Weight Deflectometer device and its potential uses are discussed.

2.2 Fatigue Behavior Models

Researchers have developed several models to characterize fatigue behavior. These models include (1) the phenomenological model, (2) the continuum damage model, (3) the fracture mechanics model, and (4) the RDEC model. The following subsections provide a detailed discussion of these models.

2.2.1 Phenomenological Model

This model relates stresses and strains in the HMA layer directly to the number of cycles to failure. The original model, which is a simple power curve, is listed in the following equations. The number of cycles to failure is determined from Equation 1 for controlled-stress testing and Equation 2 for controlled-strain testing [6].

$$N_f = A(1/\epsilon)^b \qquad \textit{Equation 1}$$

$$N_f = C(1/\sigma)^d \qquad \textit{Equation 2}$$

In these equations, N_f is the number of cycles to failure, ε and σ are strain and stress, respectively, and *A*, *b*, *C*, and *d* are parameters based on the mixture.

This model was modified by Pell [8], where he determined that tensile strain was the primary cause of fatigue cracking. This relationship is presented as Equation 3, where ε_t is the tensile strain, and k_1 and k_2 are parameters based on the mixture:

$$N_f = k_1(1/\epsilon_t)^{k_2} \qquad \textit{Equation 3}$$

The model relating tensile strain to number of cycles to failure was modified by Monismith et al. [9], to include the influence of stiffness on fatigue life. This relationship is presented as Equation 4 [6], where S_0 is the initial stiffness, and *a*, *b*, and *c* are parameters based on the mixture:

$$N_f = a(1/\epsilon_t)^b(1/S_0)^c \qquad \textit{Equation 4}$$

The phenomenological model is limited because it does not account for damage accumulation in the mixture [6]. Therefore, the actual relationship between strain and number of loading cycles to failure will not be a simple power curve. This model is also

limited since it models damage accumulation as linear which is not accurate for low strain levels [2], as will be seen later when discussing the RDEC model.

2.2.2 Continuum Damage Mechanics Model

This approach was based on a mathematical model developed by Kim et al. in 1990 and 1997 relating material properties according to principles of mechanics [10] [11]. In this mathematical model, responses of asphalt concrete under fatigue loading were characterized as being due to linear viscoelasticity, fatigue damage, or micro-damage healing [12]. To remove the effects of linear viscoelasticity and look at only damage, a pseudo-strain was applied to the pavement structure by removing expected linear viscoelastic behavior to account for damage, since it was determined that non-linear-viscoelastic behavior accounted for damage [13]. This model uses a single variable, known as the internal state variable of damage. The use of a single variable to describe damage is important because it is independent of the source of damage, such as fracture or plastic deformation [6]. The model defines stress as a function of this variable and the pseudo-strain.

The relaxation modulus, E^R, which is defined as the stress at a given time divided by the applied strain in a viscoelastic material [14], is assumed to be constant in linear viscoelastic materials due to the fact that relaxation modulus quickly stabilizes with time [14]. As a result, in the original mathematical model, damage is correlated to the change in stiffness, and all changes in stiffness are assumed to be damage [6]. The relationship was therefore given as Equation 5.

$$\boldsymbol{\sigma = I(\epsilon_r)[F + G + H]} \qquad \textbf{\textit{Equation 5}}$$

In Equation 5, the variable I is the initial pseudo-stiffness, ε_r is the pseudo-strain, and F, G, and H are functions representing change in pseudo-stiffness of each hysteresis loop, loading versus unloading paths, and change in pseudo-stiffness due to healing, respectively [6].

Due to the complications of this model, Kim et al. [11] developed what is known as a continuum model, which is comprised of a pseudo-strain energy density function, a stress-strain relationship, and a damage evolution law. This continuum model is more realistic than the previous mathematical model because it analyzes microcracks under realistic loads and healing effects.

While the continuum damage model developed by Kim et al. was used successfully on both monotonic [15] and cyclic loading [16] [11] [12], this model still has several limitations. First the model assumes that all cracks are microcracks and do not develop into macrocracks. As a result of this, the effects of crack propagation are not accounted for in this model. Second, the creep compliance test must be used in addition to the tensile axial controlled-strain fatigue test to obtain model parameters, which requires additional calculations to be performed [6].

2.2.3 Fracture Mechanics Model

Fatigue cracking is divided into three stages: crack initiation, stable crack propagation, and unstable crack fracture. In the fracture mechanics model, the majority of the fatigue life is during the crack propagation phase. Fatigue life during crack propagation is measured based on the size of the crack opening as well as the crack length. The early fracture mechanics models were based on Paris' Law, which relates the rate of crack growth to the stress intensity factor using a simple power law. This original

model was first refined by adding additional terms to the model to increase the model's accuracy.

Schapery's first refinement of the model [13] related surface energy density to the creep compliance (the ratio of strain at a given time divided by constant stress in a viscoelastic material [14]) and the rate of change of dissipated pseudo-strain energy. Schapery then developed a model based on healing [17] for linear viscoelastic materials. This model uses an energy balance where the energy dissipated goes into the creation of new crack surface.

A refined micromechanics fracture healing model [18] [19] was then developed based on Schapery's linear viscoelastic model. Unlike the continuum model of Kim et al., this model links cracking intensity to the mode of dissipated energy change.

One limitation with this model is that a large amount of experimental data, such as notched-beam strength tests, are needed to examine crack initiation and growth. In addition, only crack propagation is examined, and not initiation, since the model assumes the presence of microcracks. Also, crack growth is assumed to be constant and linear elastic according to Paris' law, which is an idealized case and not actually true.

2.2.4 Rate of Dissipated Energy Change Model

Dissipated energy is defined as the energy that is released during loading and unloading of a pavement structure. The stress-strain curves for loading and unloading do not overlap for any material that is not purely elastic. These stress-strain curves are together referred to as the hysteresis loop (Figure 1). The dissipated energy for a given loading cycle is equal to the area inside the hysteresis loop [6]. This dissipated energy is used to calculate the rate of dissipated energy change, or RDEC.

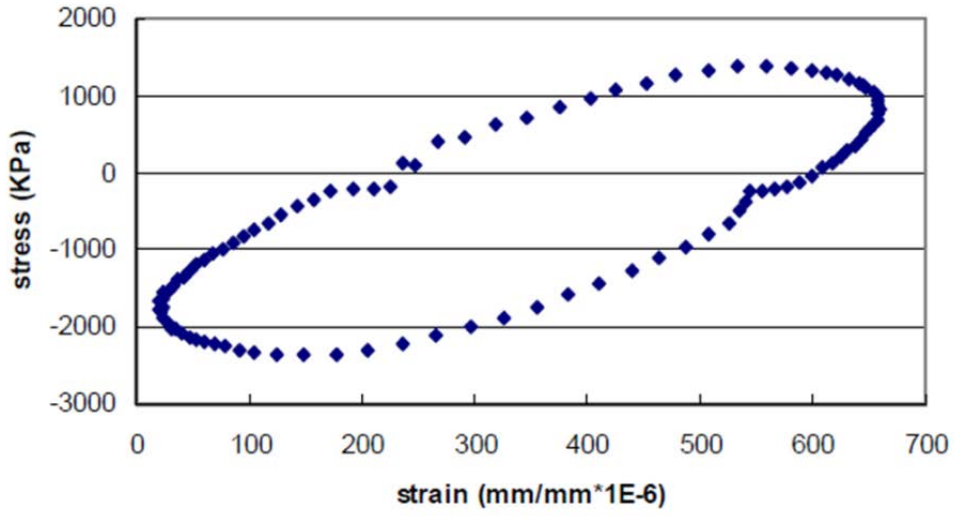

Figure 1: Stress-strain hysteresis loop [6]

The dissipated energy ratio (DER), also known as the rate of dissipated energy change (RDEC), is defined as the rate of change that energy is being dissipated [2]. The concept was first adopted to capture fatigue behavior at high stiffness and low temperatures [20] [21]. RDEC is a ratio of the difference of dissipated energy between load cycles ($DE_{n+1} - DE_n$) to the dissipated energy in the first of the two consecutive load cycles being compared (DE_n), given as Equation 6 [22]. This ratio is a very good tool for predicting fatigue failure. A typical RDEC graph is shown below in Figure 2.

$$RDEC = \frac{DE_{n+1} - DE_n}{DE_n} \qquad \textbf{Equation 6}$$

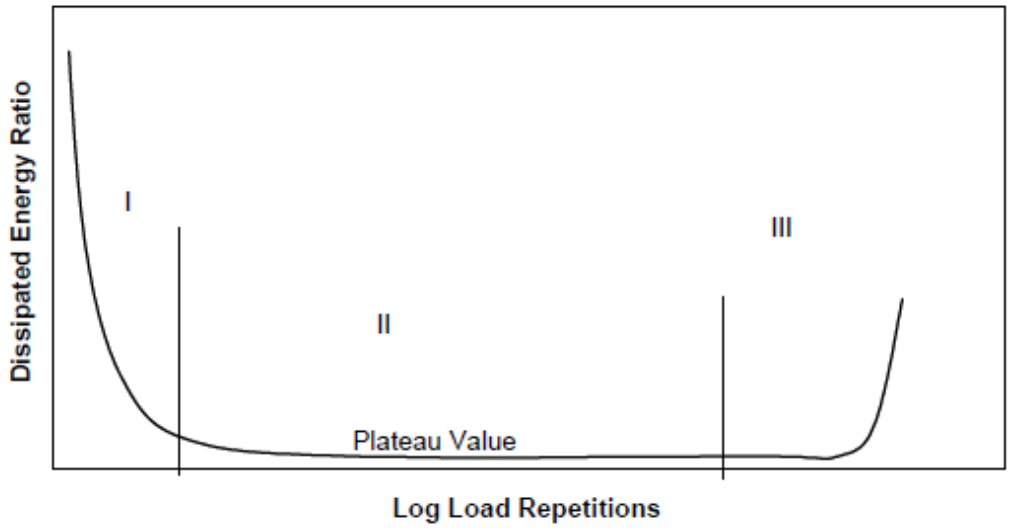

Figure 2: Dissipated Energy Ratio plot [2]

What can be observed from Figure 2 is that the plot is divided into three zones. In zone I, the RDEC is rapidly decreasing, signifying that a high amount of energy is dissipated initially due to the material densification, and the amount of energy dissipated with each repetition decreases until a plateau (zone II) is reached, where the ratio stays a constant for a long period of time. At this point, the pavement structure is no longer densifying, and so energy is released at a constant rate due to steady crack growth. The constant RDEC value in this region is known as the plateau value, or PV. The number of cycles to failure as defined earlier falls in this plateau region. After failure, the RDEC begins to increase again (zone III). This is due to energy being released at a faster rate due to the increased surface area created by unstable crack propagation.

RDEC for each cycle can be determined by plotting the dissipated energy versus number of loading cycles. A dissipated energy versus loading cycles plot typically takes the form of a power curve. The best-fit curve has an equation with loading cycles raised

to the power *k*. This exponent *k* is used to calculate the RDEC. [6] A typical plot is shown in Figure 3.

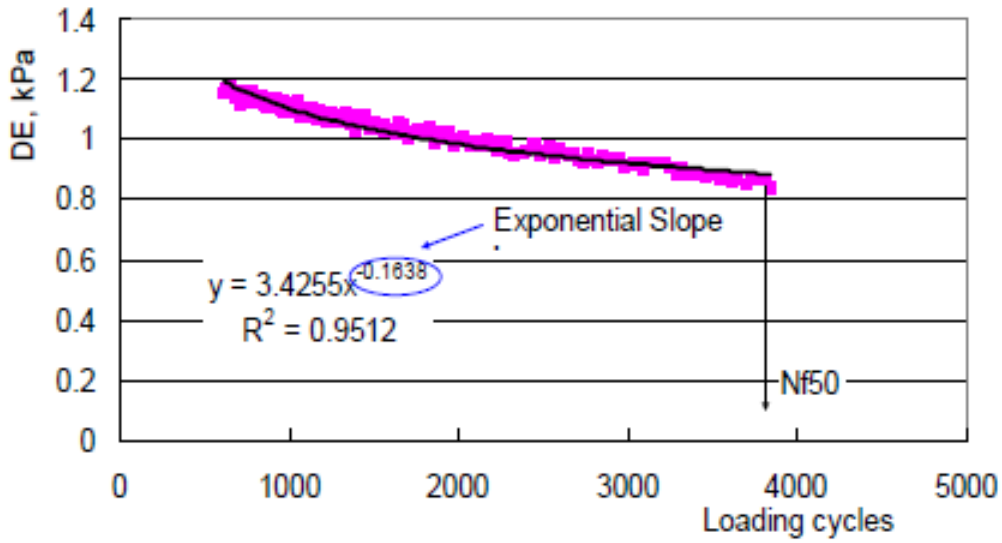

Figure 3: Typical dissipated energy versus number of cycles plot. [23]

The N_{f50} denoted in Figure 3 is defined as the number of cycles it takes for the HMA layer to reach 50 percent of the initial modulus, which has been defined as fatigue failure. This can be measured in the lab at normal strain levels; however, at low strain levels the number of cycles to failure will take a long time to achieve due to the fact that strains would be near or below the fatigue endurance limit [2]. The lab testing that was performed at UIUC was a third-point simple flexure test (AASHTO T-321).

Carpenter et al. discovered linear relationships between the log of the tensile strain and the log of load repetitions to N_{f50} for various binder mixes, as can be shown in

Figure 4 [2]. These relationships usually take a power curve form (linear when plotted on a log-log scale), presented earlier as Equation 3 in the phenomenological model subsection.

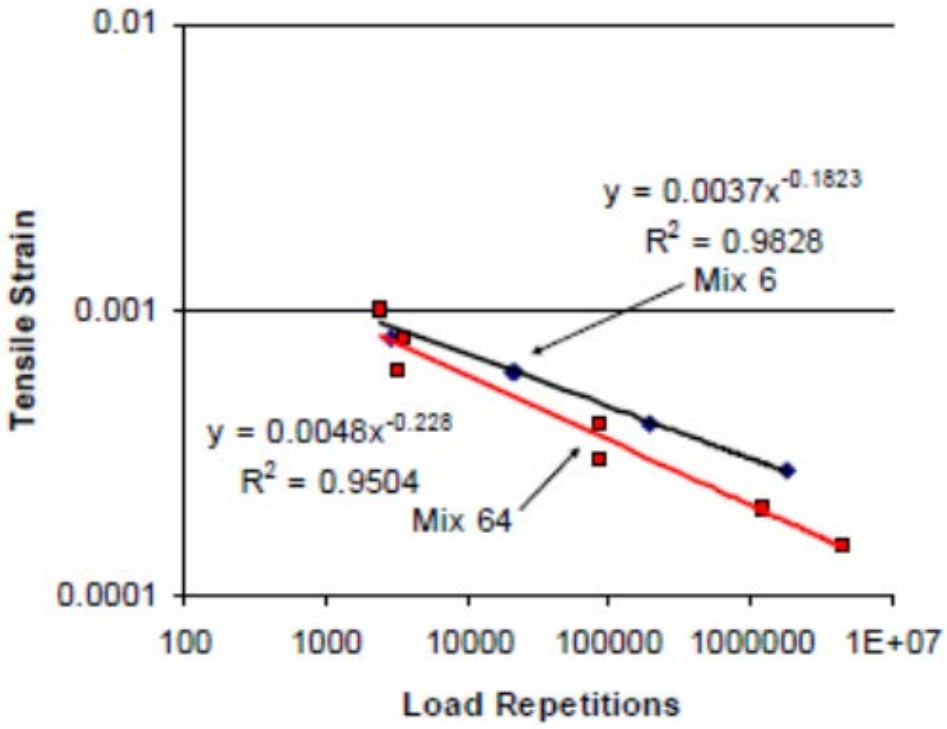

Figure 4: Typical tensile strain vs. loading cycles to failure relationship for asphalt mixes [2]

Figure 5 shows a plot of tensile strain versus number of loading cycles to failure. While Figure 4 examines only normal strain levels above 100 microstrains, Figure 5 examines both normal and low strain levels. When plotted on a log-log scale, the plot is linear for normal strain levels, but at low strain levels, there is a change in slope. The point at which the change in slope occurs is the fatigue endurance limit. It was determined that this value is different for different types of binder mixes. Note that the

data points in the low strain region, beyond 38 to 46 million load cycles [2], were extrapolated, as testing to 10^{38} loading cycles would take an extremely long amount of time [2].

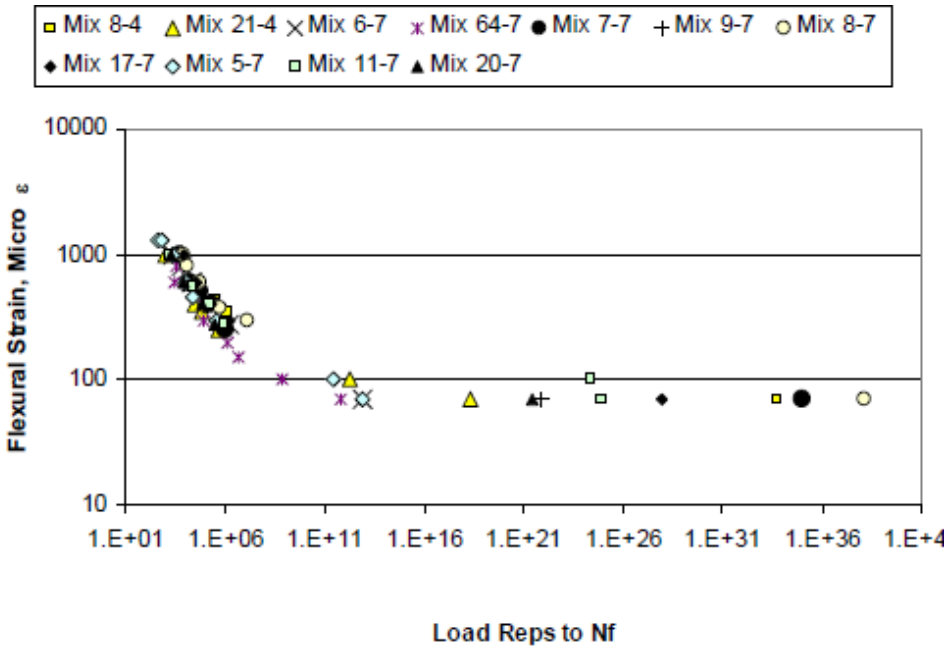

Figure 5: Tensile strain versus number of cycles to failure [2]

From Figure 5, it is seen that the slope change signifying the transition from normal strain to low strain takes place around 70 microstrains for the mixes tested by Carpenter et al. [2] Unlike the tensile strain versus number of cycles to failure relationship, there appears to be a unique relationship between the plateau value and the cycles to failure based on 50 percent drop in modulus, which is true regardless of mixture type, normal or low strain, or strain history, as can be seen in Figure 6.

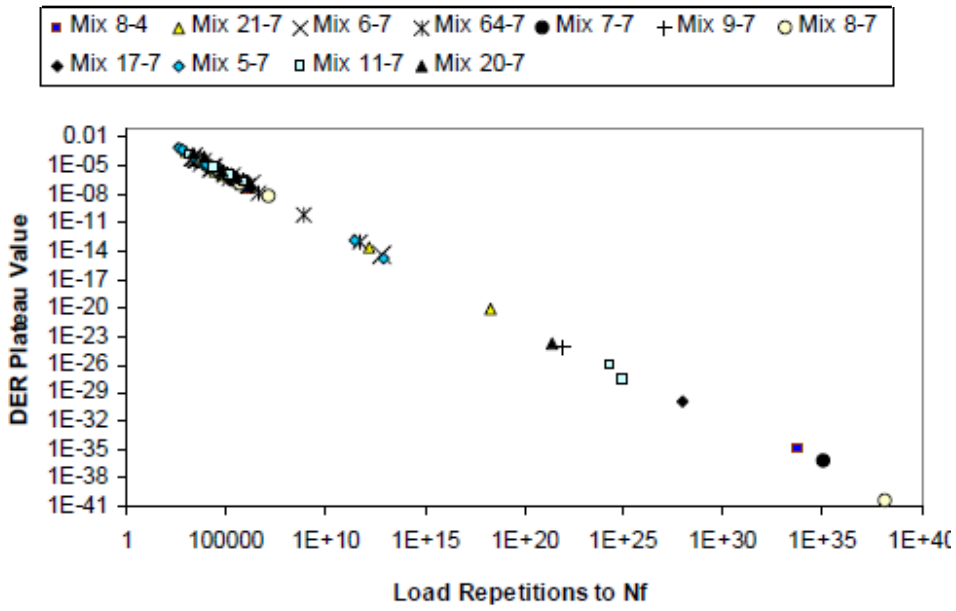

Figure 6: Plateau Value versus N_{f50} relationship [2]

Although the strain-based fatigue endurance limit was mix dependent, the threshold plateau value was unique regardless of mixture. Based on the study from Carpenter et al. [2], the strain-based fatigue endurance limit is 70 microstrains.

Shen and Carpenter refined the original RDEC model of Carpenter et al., and determined that the RDEC, rather than the dissipated energy itself, is responsible for fatigue damage in a pavement structure. Shen and Carpenter developed a fatigue model based on results from 19 different mixtures from the Illinois Department of Transportation. [6] The laboratory at the University of Illinois Urbana-Champaign (UIUC) also prepared beams from samples re-compacted from NAPTF mixes as well as mixes matching the job mix formula used for CC1, CC3, and CC5 NAPTF test sections. The testing that was used was a third-point simple flexure test using controlled-strain

testing [6]. A plateau value versus cycles to failure plot was developed from this model, and is shown in Figure 7. [23]

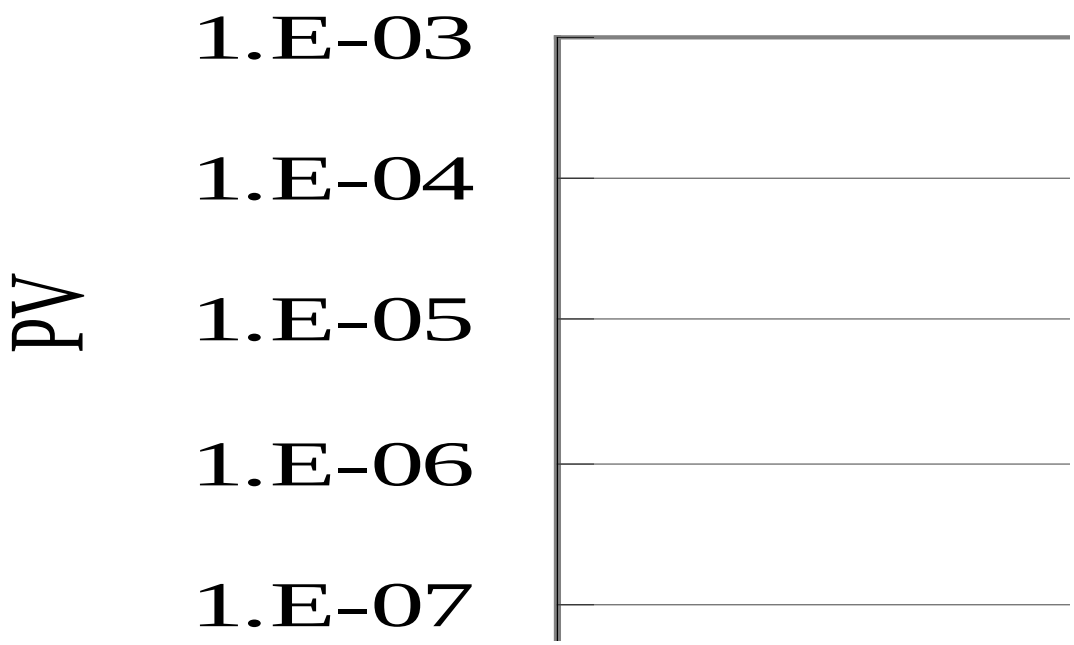

Figure 7: Plateau value vs. cycles to failure for UIUC model [6] [23]

Carpenter and Shen developed a fatigue model for the NAPTF mixes using the following equations: [2] [23]

$$PV = 2.612 \times 10^{-10} IDE^{2.758} S^{2.493} VP^{3.055} GP^{-2.445} \quad \textit{Equation 7}$$

$$PV = 61.336\epsilon^{5.052} S^{2.749} VP^{1.643} GP^{-0.094} \quad \textit{Equation 8}$$

$$N_f = 0.4801 PV^{-0.9007} \quad \textit{Equation 9}$$

$$VP = \frac{AV}{AV+V_b} \quad \textit{Equation 10}$$

$$GP = \frac{P_{NMS}-P_{PCS}}{P_{200}} \quad \textit{Equation 11}$$

$$V_b = 100 \times \frac{G_{mb} \times P_{AC}}{G_b}$$ *Equation 12*

Where ε is the tensile strain (unitless), S is the flexural stiffness of HMA mix at 20 °C and 10 Hz in MPa, VP is the volumetric parameter (unitless), AV is the percent air voids of the mixture, V_b is the asphalt content by volume, expressed as a percent, G_b is the bulk specific gravity of the asphalt binder (unitless), GP is the aggregate gradation parameter (unitless), P_{NMS} is the percent of aggregate passing the nominal maximum sieve size, P_{PCS} is the percent of aggregate passing the primary control sieve (PCS = NMS x 0.22), P_{200} is the percent of aggregate passing number 200 sieve, %, and IDE is the initial dissipated energy in kPa.

Equation 7 is first used to calculate the plateau value based on initial dissipated energy, stiffness, and volumetric and gradation parameters. From this plateau value, Equation 8 is used to calculate the theoretical tensile strain. In addition, Equation 8 can also be used to estimate the fatigue endurance limit by plugging in the value 6.74×10^{-9} for PV and solving for tensile strain. If the plateau value was below 6.74×10^{-9}, the pavement was considered to be a perpetual pavement, as that plateau value corresponded to the transition point between normal strain and low strain [6]. Equation 9 relates plateau value to number of cycles to failure using the relationship displayed in Figure 7. Equations 10 and 11 are used to calculate the volumetric and gradation parameters, respectively, and Equation 12 can be used to calculate voids filled with binder if that parameter is not given. From Shen and Carpenter's model, the fatigue endurance limit was found to vary within a range from 70 to 350 microstrains [6].

2.2.5 Summary of Fatigue Models

Table 1 presents the basic concepts of each model as well as the limitations of each model. From all of these models presented, the RDEC model was selected because it models the entire fatigue life of a pavement structure, it can be used for many different types of asphalt binder mixes, and it examines behavior at both normal strain levels and low strain levels. The mixes used in calibrating the RDEC model were similar to those at the NAPTF.

Table 1: Summary of Fatigue Models

Model	Concepts	Limitations
Phenomenological Model	➢ Relates stresses and strains in HMA layer directly to number of cycles to failure using power law relationship ➢ Later refinement uses tensile strain as the variable correlated to failure, and stiffness is taken into effect	➢ Does not account for damage accumulation in the mixture ➢ Assumes damage accumulation is linear, which is not true at low strain levels
Continuum Damage Model	➢ Original mathematical model based on principles of linear viscoelasticity ➢ Pseudo-strain, or strain not due to linear viscoelastic effects, considered to be contributed to damage ➢ Damage is correlated to change in stiffness, and all changes in stiffness are considered damage ➢ Refined continuum model uses pseudo-strain energy density function, a stress-strain relationship, and a damage evolution law ➢ More realistic because loads are analyzed under realistic conditions and healing effects	➢ Assumes all cracks are microcracks and do not develop into macrocracks. ➢ Creep compliance test must be used in addition to fatigue test to obtain model parameters, requiring additional calculations

Table 1 (cont.): Summary of Fatigue Models

Model	Concepts	Limitations
Fracture Mechanics Model	➢ Divides cracking into initiation, propagation, and fracture ➢ Majority of fatigue life occurs in propagation phase, so this phase is modeled, relating crack size and crack growth rate to stress intensity factor using Paris' Law ➢ Refined micromechanics fracture healing model links cracking intensity to the mode of dissipated energy change	➢ Does not accurately model crack initiation ➢ Large amount of experimental data needed ➢ Assumes crack growth is linear elastic, which is not the case
RDEC Model	➢ Rate of dissipated energy change is used to characterize fatigue behavior ➢ RDEC stays constant during loading, except during initial loading passes and after fatigue failure has occurred ➢ Constant RDEC is known as plateau value, and it corresponds uniquely to the number of cycles to failure ➢ Shen and Carpenter developed equations that can be used to calculate the fatigue endurance limit	➢ Based on laboratory data, and has not yet been verified with field data

2.3 Falling Weight Deflectometer

2.3.1 Falling Weight Deflectometer Device

The falling weight deflectometer (Figure 8) is a device that measures deflections at the surface of a pavement structure. These deflections are used for the purpose of estimating the modulus values of the layers of a pavement structure. The device consists of a variable weight that is dropped on a circular plate with a diameter of 30 cm (11.81

inches). Seven deflection sensors are placed at various distances from the load. The deflections recorded from each of these sensors form what is known as a deflection basin [24]. Figure 9 shows a typical deflection basin recorded by an FWD device. This deflection basin is later used to back-calculate the modulus values of the layers within the pavement structure.

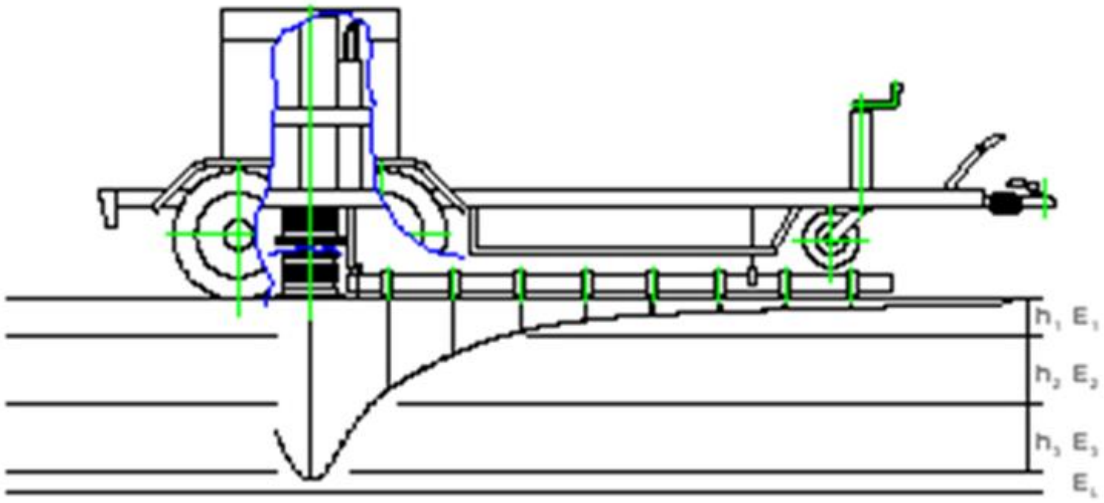

Figure 8: Falling Weight Deflectometer device [25]

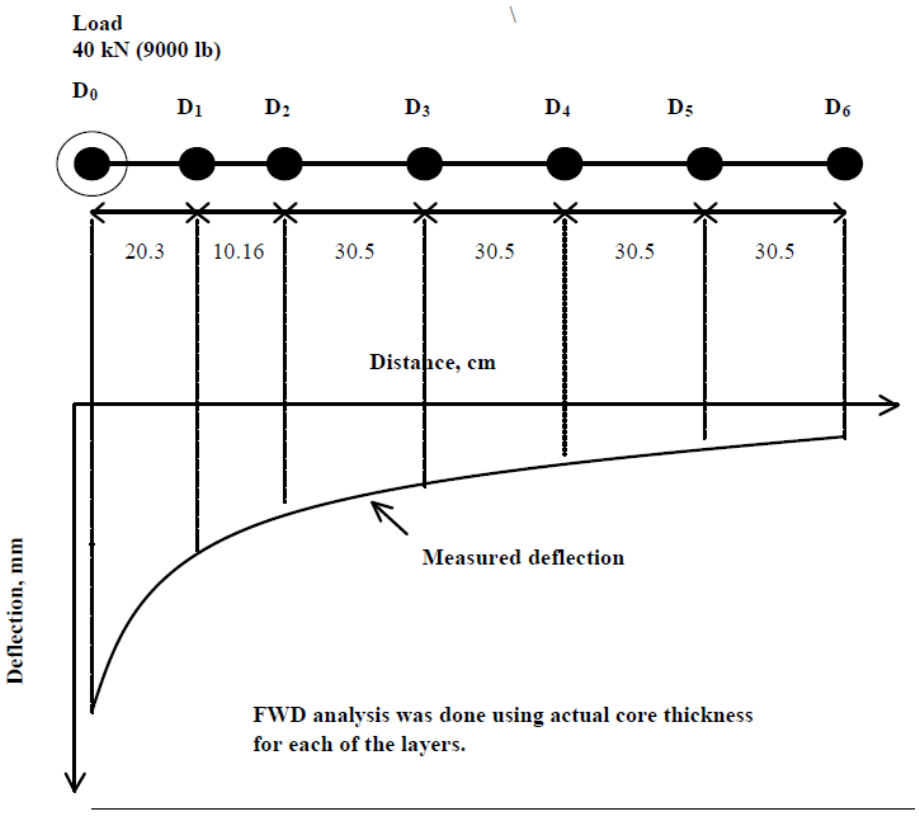

Figure 9: Typical deflection basin for FWD device [24]

2.3.2 Back-calculation of Modulus Values

The analysis of deflection data from a Falling Weight Deflectometer (FWD) is used to predict the modulus values of each layer within a pavement structure. Verification of the moduli output by FWD back-calculation programs is important to ensure accuracy of moduli results. Because there is no closed-form solution for computing layer modulus values given surface deflections, the back-calculation process, which is a trial-and-error process that has no unique solution, must be used. Back-calculation programs do not provide a unique solution and are dependent on user inputs [24]. If the results output by a

back-calculation program are accepted without verification, it often leads to misinterpretation of data [24].

The often inaccurate results output by back-calculation programs are due to the fact that the program minimizes the error between the actual deflection basin and the deflections calculated using linear elastic analysis on the back-calculated moduli [24]. The output modulus values are highly dependent on the initial modulus values input by the user. Often, several different modulus combinations will yield identical deflection basins. In addition, even if the error between the actual and computed deflection basins is very small, the output moduli values can vary significantly [24]. Another drawback with the use of back-calculation is that a linear elastic analysis is used, while the actual pavement behavior is either nonlinear elastic or viscoelastic. However, a linear elastic analysis is performed for simplification of calculations [24]. Because the majority of the surface deflection under the load is attributed to the subgrade, it is important that the modulus of the subgrade is known with confidence. Once the subgrade modulus is known, the moduli of the higher layers can be estimated.

2.4 Summary

In this chapter four fatigue models were discussed. These were the phenomenological model, the continuum damage model, the fracture mechanics model, and the RDEC model. For each of the first three models, there were several limitations to each model. For the phenomenological model, damage accumulation in the mixture is not taken into account. Damage accumulation is also treated as linear, which is not true for low strain levels [2]. For the continuum damage model, it is assumed that all cracks are microcracks and do not develop into macrocracks; and the creep compliance test must be

used in addition to the fatigue test to obtain model parameters, which requires additional calculations to be performed [6]. Finally, for the fracture mechanics model, a large amount of experimental data is needed to examine crack initiation and growth, and only crack propagation is examined and not initiation. Unlike the previous three models, the RDEC model is applicable to the entire fatigue life of a pavement structure, and that is the main reason the RDEC model was selected.

The RDEC model is based on the ratio of dissipated energy change. Ratio of dissipated energy change is the rate of change of dissipated energy between two consecutive loading cycles. Dissipated energy can be calculated from the area within the hysteresis loop, which is a curve created from the stress-strain curves due to loading and unloading. When RDEC is plotted versus number of loading cycles, the curve decreases initially, stays constant, and then increases again. The region of the curve where RDEC is constant is known as the plateau region, and the RDEC value in this region is the plateau value. Fatigue failure, which is defined as a 50 percent decrease in the HMA dynamic modulus, occurs in the plateau region. In addition, this plateau value is important because there is a unique relationship between the plateau value and the number of cycles to failure that is true for all binder mix types and loading conditions. Shen and Carpenter [6] developed equations for estimating the strain-based fatigue endurance limit based on mixture properties. It was determined from this model that the strain-based fatigue endurance limit ranged from 70 to 350 microstrains. However, there is still a limitation to the RDEC model, namely that it was tested only on laboratory data.

A way to predict the 50 percent reduction in modulus in HMA that causes fatigue failure is by analyzing the results of tests performed by a Falling Weight Deflectometer

(FWD) device. These results can be used to back-calculate the modulus values of the layers within a pavement structure. Special care must be taken to ensure that the modulus values output by the back-calculation program are reasonable due to the fact that back-calculation programs are trial-and-error and are dependent on initial seed values. Therefore, several iterations of the program are performed, locking the modulus values of pavement layers from the subgrade upward once the layer modulus values are known with confidence [24].

Chapter 3

Facility Layout and Materials

3.1 Introduction

In this chapter, the NAPTF test facility is discussed. Construction cycles one (CC1), three (CC3), and five (CC5) all contain flexible pavement sections trafficked using four-wheel and six-wheel loading configurations. The layout of each of the pavement sections is discussed in detail, including the strain sensor layout, wheel wander pattern configuration, and dimensions. The materials used in the preparation of the CC1 and CC3 pavement sections are then discussed. Each layer has an HMA surface layer (5 inches prepared in three lifts), a base layer, a subbase layer, and a subgrade.

3.2 Construction Cycle One (CC1)

The CC1 test strip consists of nine pavement sections. Of these nine sections, three are rigid pavement sections and the other six are flexible pavement sections. Each of these pavement sections is referred to by a three-letter abbreviation. The first letter stands for the subgrade strength. H stands for high-strength, M stands for medium-strength, and L stands for low-strength. The second letter can be F for flexible pavement or R for rigid pavement. The final letter can be S for stabilized base or C for crushed stone base. For example, the abbreviation LFS stands for a flexible pavement with a stabilized base and a low-strength subgrade. The layout of the test strip is shown in Figure 10 below, giving the dimensions of each of the pavement sections within CC1. Each neighboring pavement section has a 25-foot transition area between them, for a total test strip length of 900 feet [26].

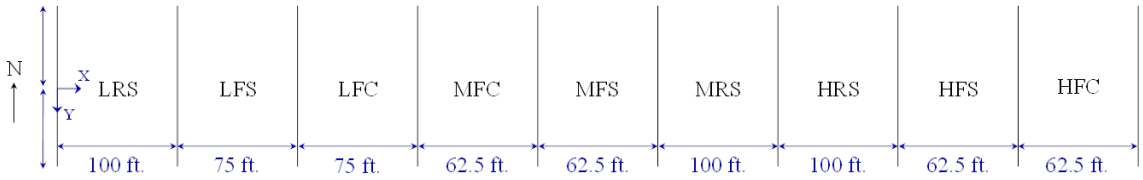

Figure 10: CC1 test strip

Within the test strip, there are numerous gages planted measuring different parameters including pressure, temperature, strain, and deflection. Strain gage data has been taken from the National Airport Pavement Testing Facility (NAPTF) website, and is used both when analyzing peak strain data variability as well as examining the peak strain when the number of loading cycles to failure occurs through the analysis of FWD data. In this study, four sections of the CC-1 test strip were analyzed. They were LFS (low-strength subgrade, flexible pavement, stabilized asphalt base), LFC (low-strength subgrade, flexible pavement, crushed stone base), MFS (medium-strength subgrade, flexible pavement, stabilized asphalt base), and MFC (medium-strength subgrade, flexible pavement, crushed stone base). The LFS and MFS sections have sensors located in both the surface layer as well as the base, while the LFC and MFC sections have sensors located in the surface layer only. The sections labeled HFS and HFC, which have high-strength subgrade, are not examined in this thesis. Data on these sections were analyzed, but it was determined that testing ended after only 3,000 loading cycles with no signs of damage to the pavement structure.

Strain gage sensors were placed in longitudinal (i.e. measuring tensile strains parallel to the direction of trafficking) and transverse (i.e. measuring tensile strains perpendicular to the direction of trafficking) directions. The naming convention for the

strain gage sensors within the CC1 pavement consists of three letters followed by a number. The first letter is L, M, or H; for low-strength, medium-strength, or high-strength subgrade. The second letter is S for surface or B for base. The third letter is S for stabilized base or C for crushed stone base, and the number ranges from 1 to 12, giving the position of the sensor relating to Figure 11 below. While medium-strength and high-strength subgrade flexible pavement sections are not displayed in Figure 11, the layout is identical to that for low-strength subgrade flexible pavement sections.

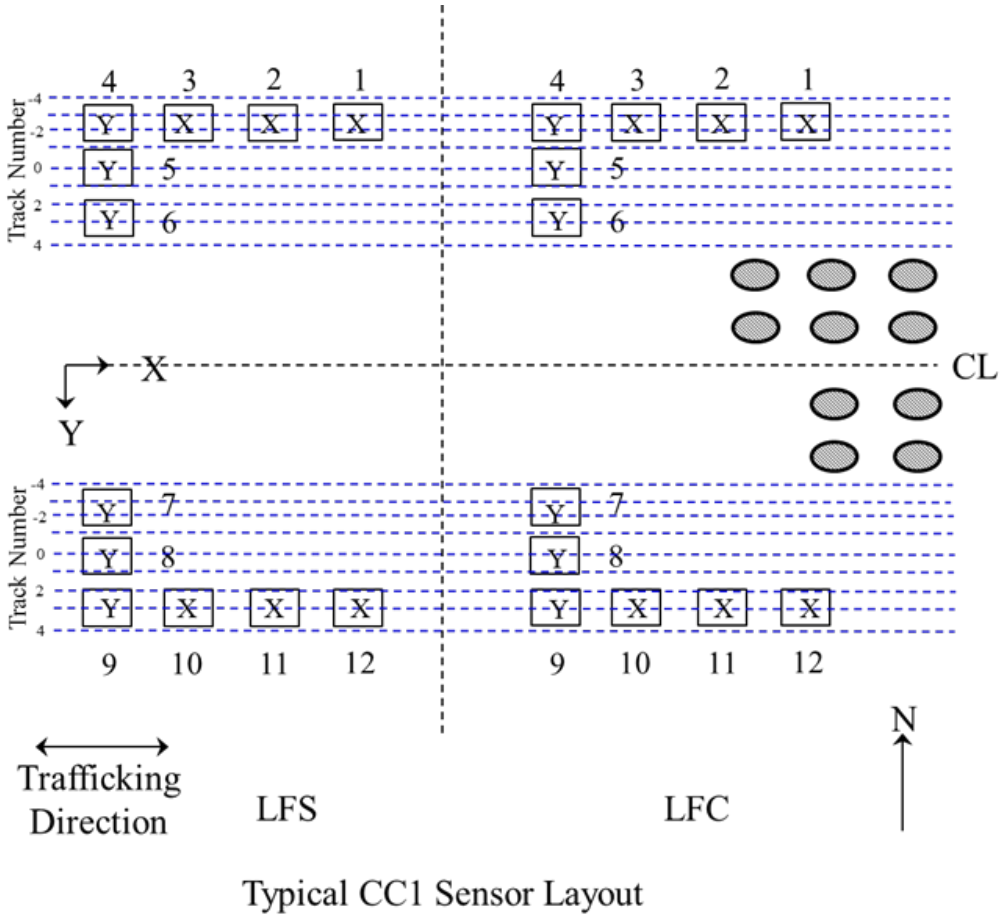

Typical CC1 Sensor Layout

Figure 11: Locations of strain gage sensors in LFS and LFC pavement (Plan view)

The dashed line going horizontally across the center of Figure 11 indicates the centerline of the testing facility pavement. Sensor locations are marked with boxes. The transverse sensors, marked with the letter Y inside the box, are located 10.42, 12.71, and 15 feet from the centerline in either direction. The longitudinal sensors, marked with the letter X inside the box, are spaced approximately 2.37 feet (28.5 inches) apart.

Figure 12 and Figure 13 show the vertical location of the strain sensors within CC1, as well as the depths of each of the pavement layers within the low-strength subgrade and medium-strength subgrade flexible pavement sections, respectively. Each sensor is located half an inch from the bottom of the surface or stabilized base HMA layer.

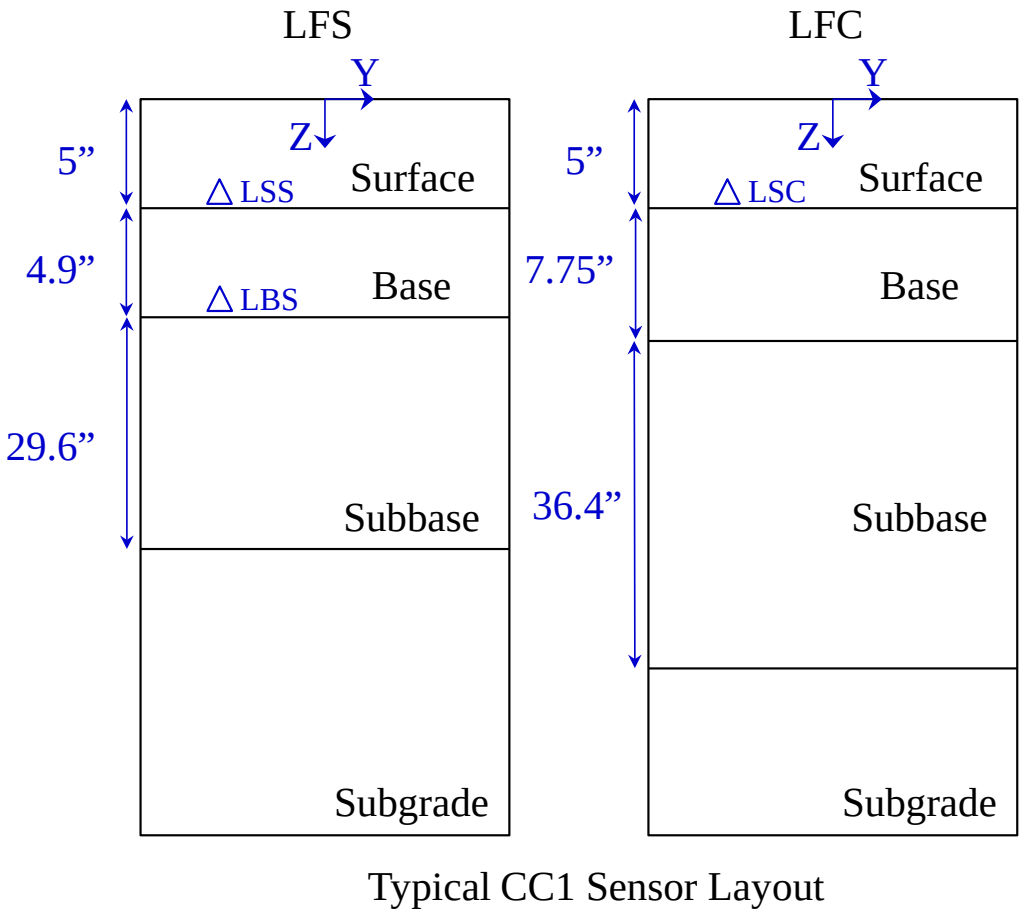

Typical CC1 Sensor Layout

Figure 12: Elevation view of LFS and LFC pavement sections

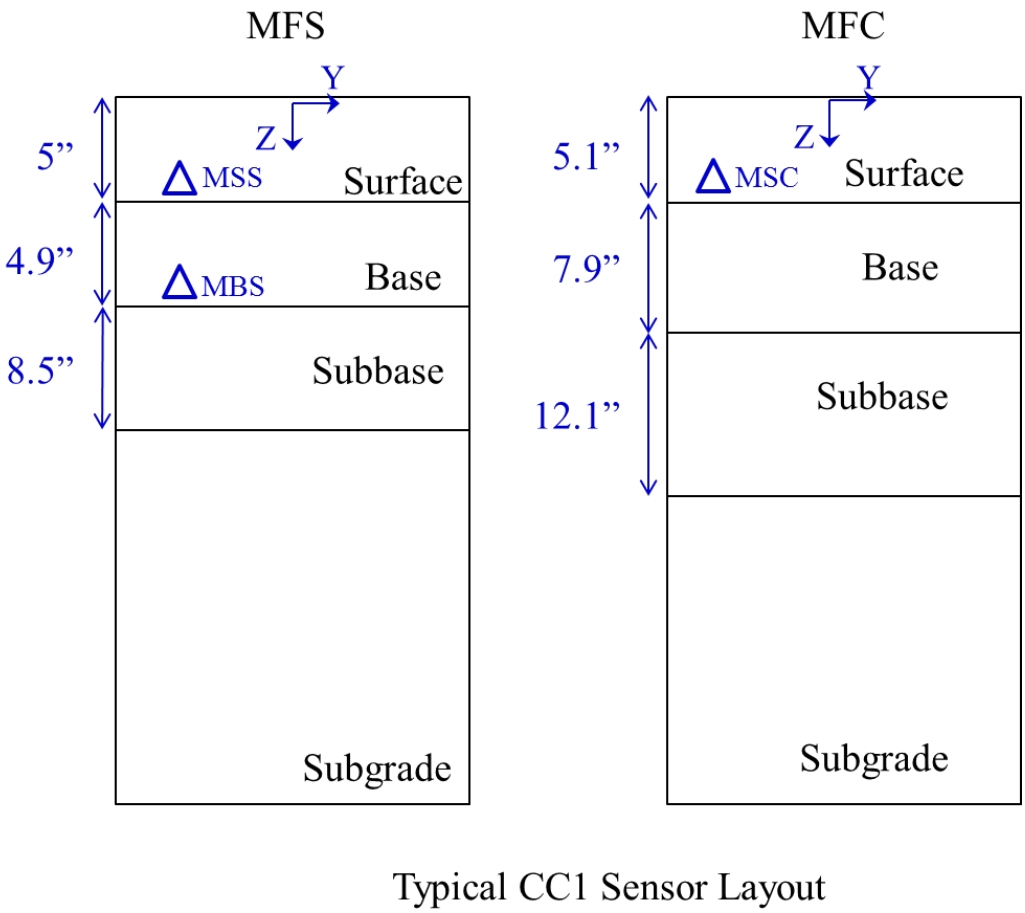

Figure 13: Elevation view of MFS and MFC pavement sections

3.3 Construction Cycle Three (CC3)

The CC3 test strip consists of four flexible pavement sections. The test strips are numbered LFC-1, LFC-2, LFC-3, and LFC-4. The difference between the four sections is the depth of the subbase layer. Figure 14 shows an elevation view of the CC3 test pavement. The materials used for each of the layers are listed, as well as the depth of each layer. Each transition segment is 20 feet long, except for the transition following LFC-4 which is 25 feet in length, for a total length of 345 feet for the entire test strip. [26]

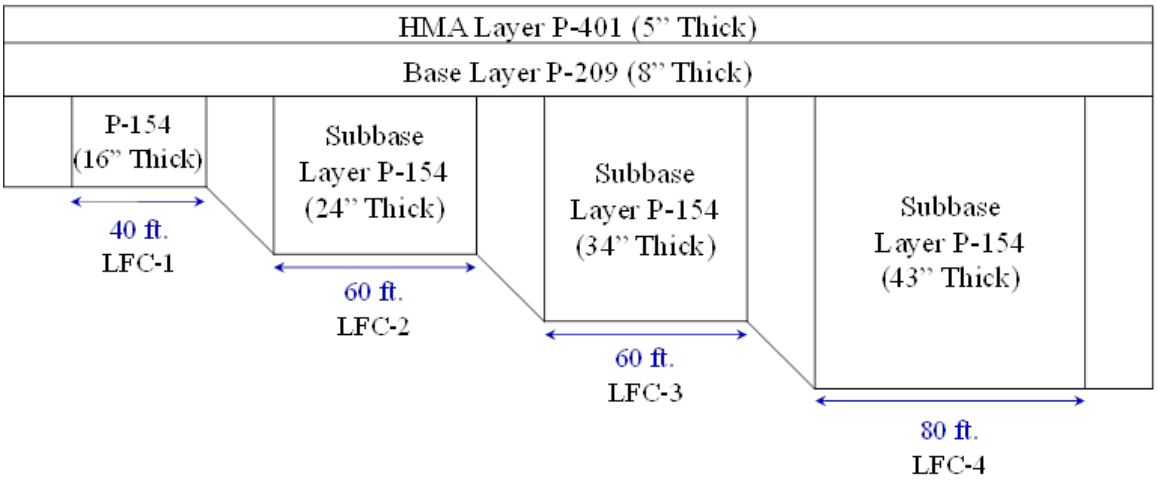

Figure 14: Elevation view of CC3 test pavement. [26]

CC3 test pavement has a total of 36 asphalt strain gages. Gages ASG-1 through ASG-13 are located in section LFC-1, gages ASG-14 through ASG-18 are located in section LFC-2, gages ASG-19 through ASG-23 are located in section LFC-3, and gages ASG-24 through ASG-36 are located in section LFC-4. All strain gages are located 5 inches below the surface. Locations of all strain gages in the CC3 pavement are given in Figure 15.

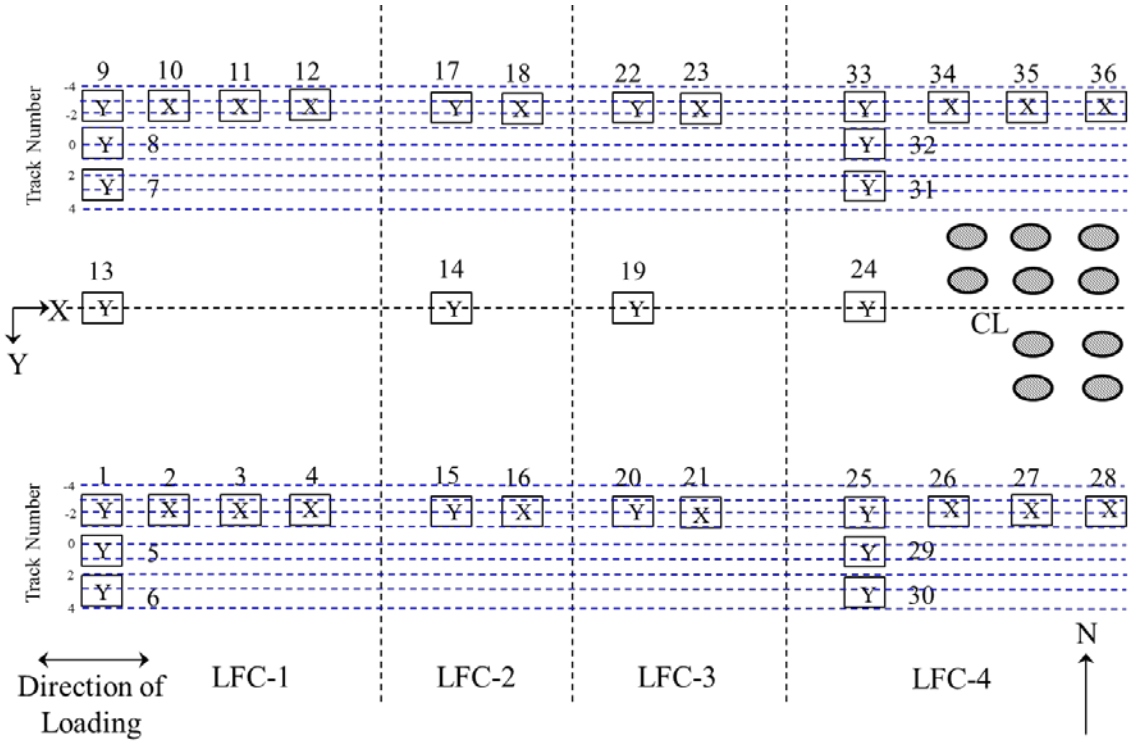

Figure 15: Locations of strain gage sensors in CC3 pavement (Plan view)

3.4 Construction Cycle Five (CC5)

The sections constructed during CC5 included four flexible pavement sections, and like CC3, all sections were constructed on low-strength subgrade. The subbase depths for sections LFC-1 and LFC-4 was 34 inches, while sections LFC-2 and LFC-3 had 38 inches of subgrade. Sections LFC-1 and LFC-2 were tested with different wheel configurations, while sections LFC-3 and LFC-4 were tested with different subbase materials. Sections LFC-1 West and LFC-2 East had a six-wheel load only on the north track, while the south track had both a six-wheel and four-wheel load. Sections LFC-1 East and LFC-2 West had both loads on the north track and only the six-wheel load on the south track. Sections LFC-3 and LFC-4 had six-wheel loads on both the north and

south tracks, however, the north track used a dense-graded aggregate P-154 granular subbase, while the south track used a crushed quarry P-154 subbase. The surface and base layers of CC5 were the same as in CC3, namely, P-401 hot-mix asphalt and P-209 dense-graded crushed aggregate base. CC5 contains 20 strain gages measuring the longitudinal and transverse tensile strains in the pavement. Figure 16 gives the location of all asphalt strain gages within CC5 pavement.

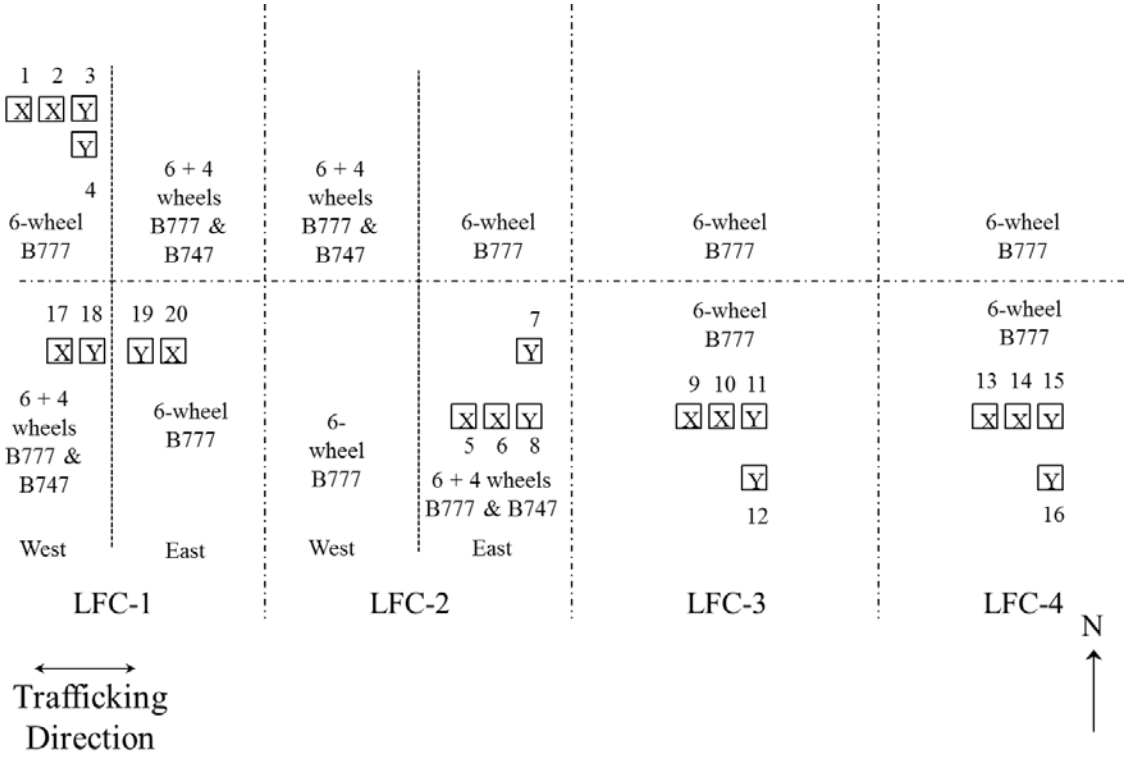

Figure 16: CC5 strain gage layout

3.5 National Airport Test Vehicle

The test vehicle for CC1 and CC3 consists of a three-axle north carriage, simulating the load of a Boeing 777 aircraft, and a two-axle south carriage, simulating the

load of a Boeing 747 aircraft. From looking at the strain gage data over time and seeing whether there are two or three peaks, it can be determined if the sensor is on the north or south track, as there is one peak for each axle passing over the sensor. Figure 17 shows the dimensions and wheel spacing of the test vehicle for CC1 test runs, and Figure 18 shows the dimensions and wheel spacing for CC3 test runs.

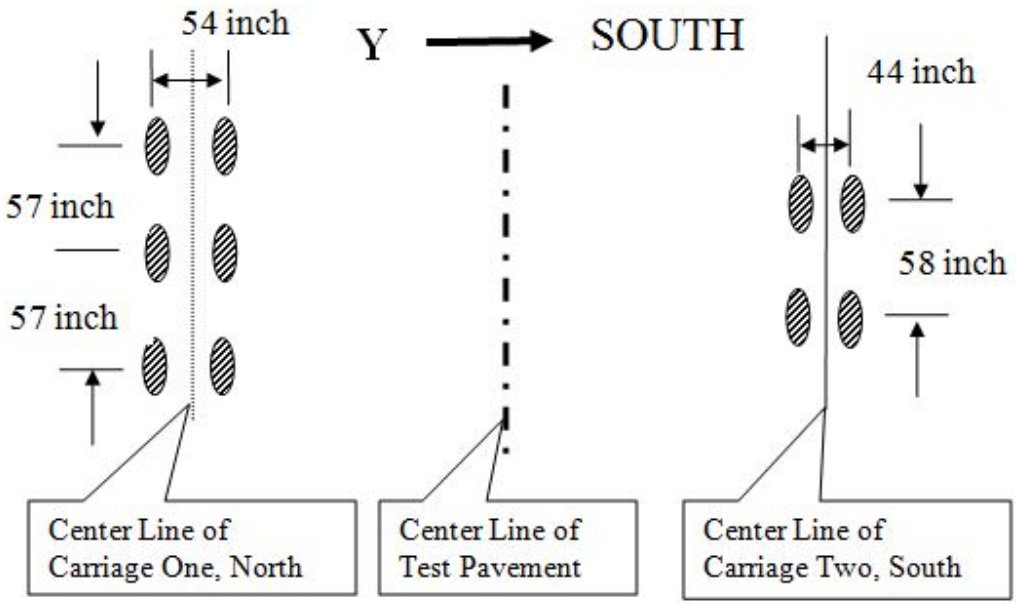

Figure 17: Dimensions of CC1 Test Vehicle [26]

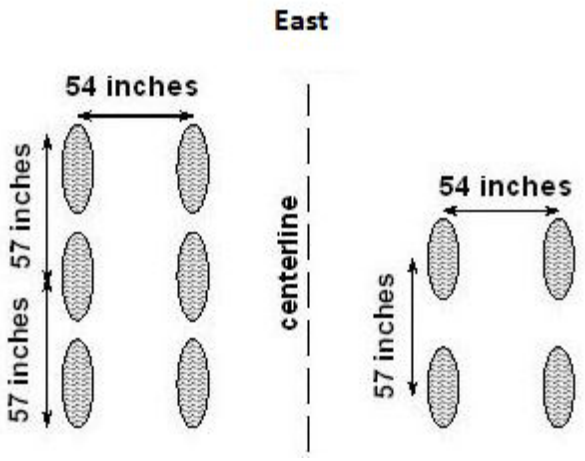

Figure 18: Dimensions of CC3 Test Vehicle [26]

The test vehicle can be placed at different positions in the north-south direction relative to the centerline. These positions, known as wander positions or track numbers, are numbered from -4 to 4, with zero being over the centerline of the wander track. The wander pattern simulates a normal distribution of taxiway traffic, with the track numbers closer to zero having a greater total number of passes along that track. The different wander positions are given below in Figure 19, with the pass numbers on the first day of testing, February 14, 2000, being given at the right of the figure. Note that pass number 1 is event number 5, since the first four passes were test runs and were excluded from the data. Therefore, to obtain the event number (referred to as the "pass number" for the remainder of this thesis), add four to each pass number listed in Figure 19. The wander pattern listed for CC1 is also used for CC3, since the same loading configuration is used for both construction cycles.

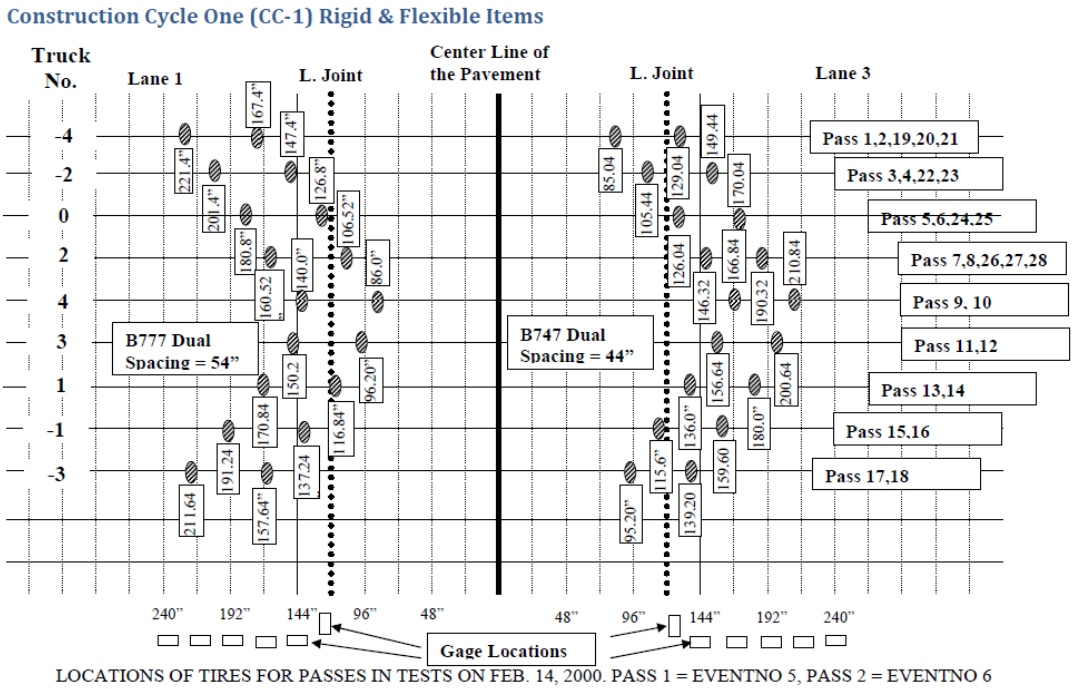

Figure 19: Wander pattern for CC-1 tests [26]

The wander pattern for CC5 is given in Figure 20 for a six-wheel and a four-wheel load together (Sections LFC-1 and LFC-2), and in Figure 21 for a six-wheel load only (Sections LFC-3 and LFC-4). Like in CC1 and CC3, there are nine tracks numbered from -4 to 4, with the wheels being centered within the wheel track in Track 0.

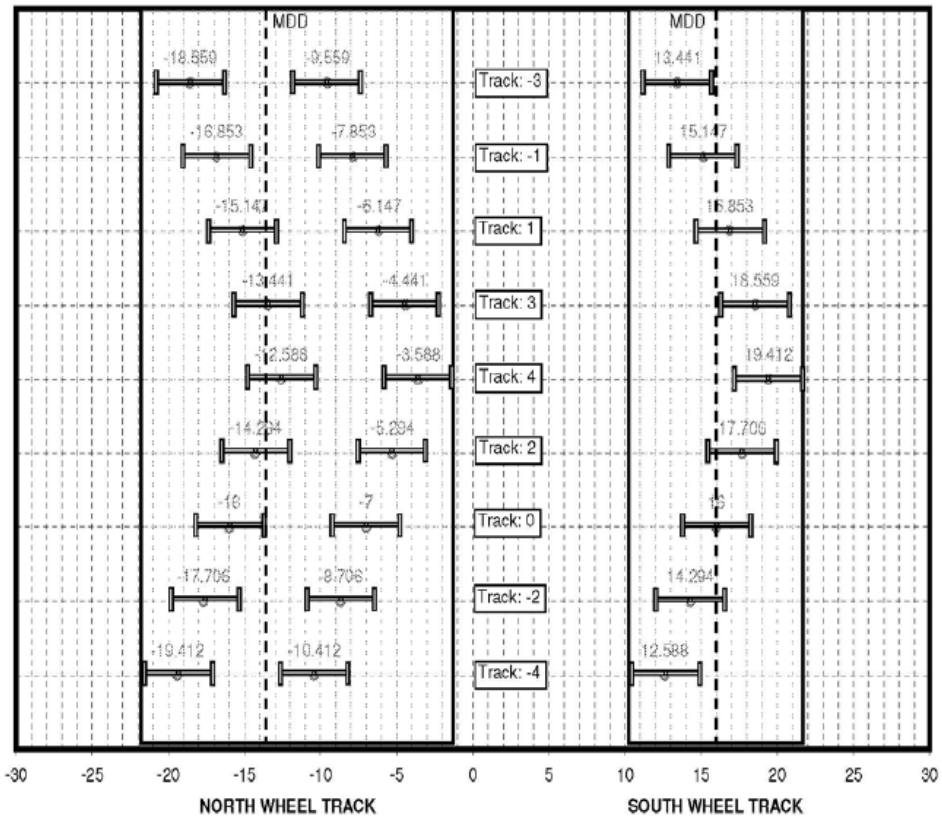

Figure 20: Wander pattern for CC-5 with 6-wheel and 4-wheel load [26]

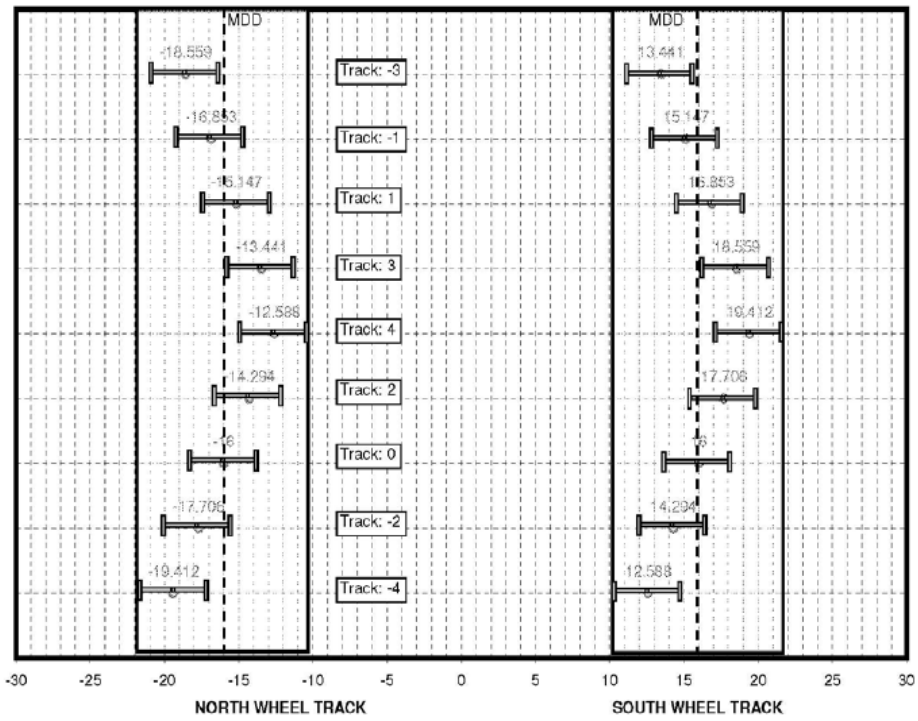

Figure 21: Wander pattern for CC-5 with 6-wheel load only [26]

Not all pavement sections were tested in all loading passes. Table 2 lists whether sections were loaded in different CC1 loading passes; and Table 3 lists the same for CC3. These tables were created from querying traffic data on the NAPTF website. The querying process is outlined in Appendix A. Note that in the later passes, especially in CC3, the section may have been loaded but strain gage data is not available. This is because many of the strain gages fail before loading is complete. Table 4 lists trafficking information for CC5. Note that for CC5, different sections were trafficked at different times, and the pass numbering for each section begins at one.

Table 2: Load pass summary for CC1 [26]

Pass Numbers	LFS Loaded?	LFC Loaded?	MFS Loaded?	MFC Loaded?
5-32	Yes	Yes	Yes	Yes
33-2795	No	No	No	No
2796-15758	Yes	Yes	Yes	Yes
15759-22679	Yes	Yes	Yes	No
22680-22745	Yes	Yes	No	No
22746-26031	Yes	No	No	No
26032-48882	Yes	Yes	No	No

Table 3: Load pass summary for CC3 [26]

Pass Numbers	LFC-1 Loaded?	LFC-2 Loaded?	LFC-3 Loaded?	LFC-4 Loaded?
1-990	Yes	Yes	Yes	Yes
991-3168	No	Yes	Yes	Yes
3169-23826	No	No	Yes	Yes

Table 4: Load pass summary for CC5

Section	Pass Numbers	Trafficking Start Date	Trafficking End Date
LFC-1 through 4 North	1-12540	August 14, 2008	November 7, 2008
LFC-1 South	1-12936	July 12, 2010	August 11, 2010
LFC-2 South	1-8646	August 21, 2012	October 26, 2012
LFC-3 and 4 South	1-12804	September 15, 2010	November 15, 2010
	12805-19890	August 21, 2012	October 18, 2012

3.6 Materials

The pavement sections constructed during CC1 were constructed on three different subgrade types which included low strength (Design California Bearing Ratio, CBR = 3-4), medium strength (Design CBR = 7-9), and high strength (Design CBR = 30-40) [26]. One flexible pavement section on each subgrade type was constructed utilizing a stabilized HMA base (FAA designation P-401) and a dense-graded aggregate subbase (FAA designation P-209), while another was constructed using a crushed aggregate base

(FAA designation P-209) and a dense-graded aggregate subbase (FAA designation P-154). The surface layer for all flexible pavements constructed during CC1 was prepared using a P-401 HMA binder mix [26]. It is noted that only the data collected from the flexible pavement sections placed on low-strength and medium strength subgrade layers was considered in this paper. Mixture volumetric and gradation properties for CC1 that will be used in the RDEC equations from Shen and Carpenter are given in Table 5 [26]. These values are averaged material properties taken from the NAPTF website. The raw NAPTF values are presented in Tables B-1 through B-8 of Appendix B.

Table 5: Binder mix properties of P-401 in CC1 pavement

Mix Property	LFS	LFC	MFS	MFC
Percent Air Voids	4.65	4.8	4.7	5.4
Percent Volumetric Binder Content	10.88	10.74	10.48	10.74
Percent Passing Nominal Maximum Sieve Size	93.2	93.0	93.0	93.0
Percent Passing Primary Control Sieve	58.8	60.0	58.4	59.9
Percent Passing No. 200 Sieve	6.0	5.9	5.9	5.9

The materials utilized in constructing all of the four CC3 flexible pavement sections were the same for all sections. This material consisted of a P-401 HMA surface layer, a P-209 dense graded aggregate base, a P-154 dense graded aggregate subbase, and finally a low-strength subgrade having a design CBR of approximately 3 to 4 [26]. The FAA-designated materials are as previously detailed when describing the CC1 layout. Mix properties for P-401 are the same as for section LFC of CC1 pavement.

For CC5, the P-401 is the same as for sections labeled LFC in CC1 and CC3, and the P-209 crushed aggregate base is also the same as that for CC1 and CC3 LFC sections. For the P-154 subbase, a quarry subbase is used for all sections except the north tracks of

LFC-3 and LFC-4, which use the dense-graded subbase used in CC1 and CC3. The low-strength subgrade used in CC5 was DuPont clay. [26]

The FAA designations P-401, P-209, and P-154 each signify a type of asphalt concrete or aggregate mixture material with certain specifications designated by the FAA. Materials in the P-4xx range are asphalt concrete materials, materials in the P-2xx range are base materials, and materials in the P-15x range are subbase materials. P-401 HMA uses binder that is AC-20 asphalt concrete (a PG grade is not specified) and aggregates consisting of crushed stone, gravel, or slag [27]. P-209 crushed aggregate base uses coarse aggregates consisting of crushed stone, gravel, or slag, and all fine aggregates are the result of crushing the stone or gravel [28]. P-209 should have 30 to 60 percent passing the No. 4 sieve and no more than 8 percent passing the No. 200 sieve [28]. P-154 crushed aggregate base uses granular aggregates mixed with fine sand, stone, or clay. This has a much finer gradation than P-209, with 20 to 100 percent passing the No. 10 sieve [29]. Since the actual aggregate types used in CC1 and CC3 pavement construction are not known, the specifications are given to provide the possible aggregate types that may have been used in the construction of CC1 and CC3.

Chapter 4

Methodology

4.1 Introduction

Several tests were conducted by the FAA to characterize the behavior of the flexible pavement sections that were placed and compacted during CC1, CC3, and CC5. These tests included: (1) measuring the transverse surface profiles at various times and locations to characterize rutting, (2) performing FWD tests to quantify the stiffness of each layer as loading progresses, and (3) measuring the longitudinal and transverse tensile strains to characterize fatigue cracking. In this thesis, both FWD test results along with tensile strain data from strain gages placed within the pavement were used to estimate a field-based fatigue endurance limit.

Shen and Carpenter reported that fatigue failure occurs when the flexural stiffness of the HMA layer in a pavement structure is reduced to 50 percent of its initial value [6]. This is a typical arbitrary definition for fatigue failure based on laboratory observations, since it is impossible to specifically define at what loading pass failure truly occurs. [30] Based on this definition and since the FWD test was conducted throughout the life of the pavement sections, FWD data can be analyzed at various points in time to determine the point at which the 50 percent modulus reduction occurs. Since flexural stiffness is equal to the modulus multiplied by the moment of inertia, and the cross sectional area remains fairly constant (meaning a constant moment of inertia can be assumed), using backcalculated modulus to predict fatigue behavior appears to be a valid approach. In addition, knowing when the modulus of the HMA layer reaches 50 percent of its initial

value would allow for determining the number of passes (N_{f50}) to failure by querying the trafficking data on the NAPTF website. The N_{f50} tensile strain is then defined as the peak tensile strain in the strain gage sensors for the loading pass corresponding to N_{f50}. The details of this approach are summarized in this chapter.

4.2 Estimate the Fatigue Endurance Limit Using Field Data

The falling weight deflectometer (FWD) test was conducted on the flexible pavement sections laid during CC1, CC3, and CC5. FWD was performed in order to back-calculate the modulus of each pavement layer. FWD tests were conducted before the initial loading was applied as well as during the period of trafficking. The deflection results of the FWD test were back-calculated to estimate the modulus of each layer in the pavement structure. Back-calculation of modulus values was performed using a computer program developed by the FAA known as BAKFAA, which stands for BAcKcalculation-Federal Aviation Administration [26]. The BAKFAA display is presented in Figure 22. Inputs into BAKFAA include the Poisson's ratio of each layer (the default value of 0.35 is used, as that is a typical Poisson's ratio for pavement layers), the interface parameter which ranges from 0 for fully unbonded to 1 for fully bonded (the actual bonding cannot be accurately determined, and so the fully-bonded case is used), and the layer thickness of each layer. BAKFAA assumes that the layer beneath the subgrade is infinitely stiff and infinitely deep (bedrock). For this thesis, a layer with a very high modulus, e.g. 100,000,000 psi, is placed below the subgrade. This layer is input with a layer thickness of zero, which the program treats as infinitely thick. The check marks to the right of each layer in Figure 22 denote that the program will allow the moduli of these layers to vary. If a box is unchecked, the modulus value is "locked" during the back-calculation process.

The deflection numbers from the FWD are then entered into the lower left part of the BAKFAA display. The top row is where the offset in inches of each deflection sensor from the load is input. The second row is where the deflection values in mils obtained from the FWD are entered. The third row is where the calculated deflection values based on the output moduli are displayed. Below the deflection values is a graph that shows the actual and calculated deflections plotted against distance from the load. To the right of this graph is where the plate load is input for each test run. The plate radius is always 5.91 inches (11.82 inch diameter, as stated in section 2.4), and the evaluation depth is assumed to be the default value. The “Function RMS” is the root mean square between the actual and calculated deflection values, which is what the BAKFAA program attempts to minimize. Table 6 summarizes the BAKFAA inputs and the values typically input for them.

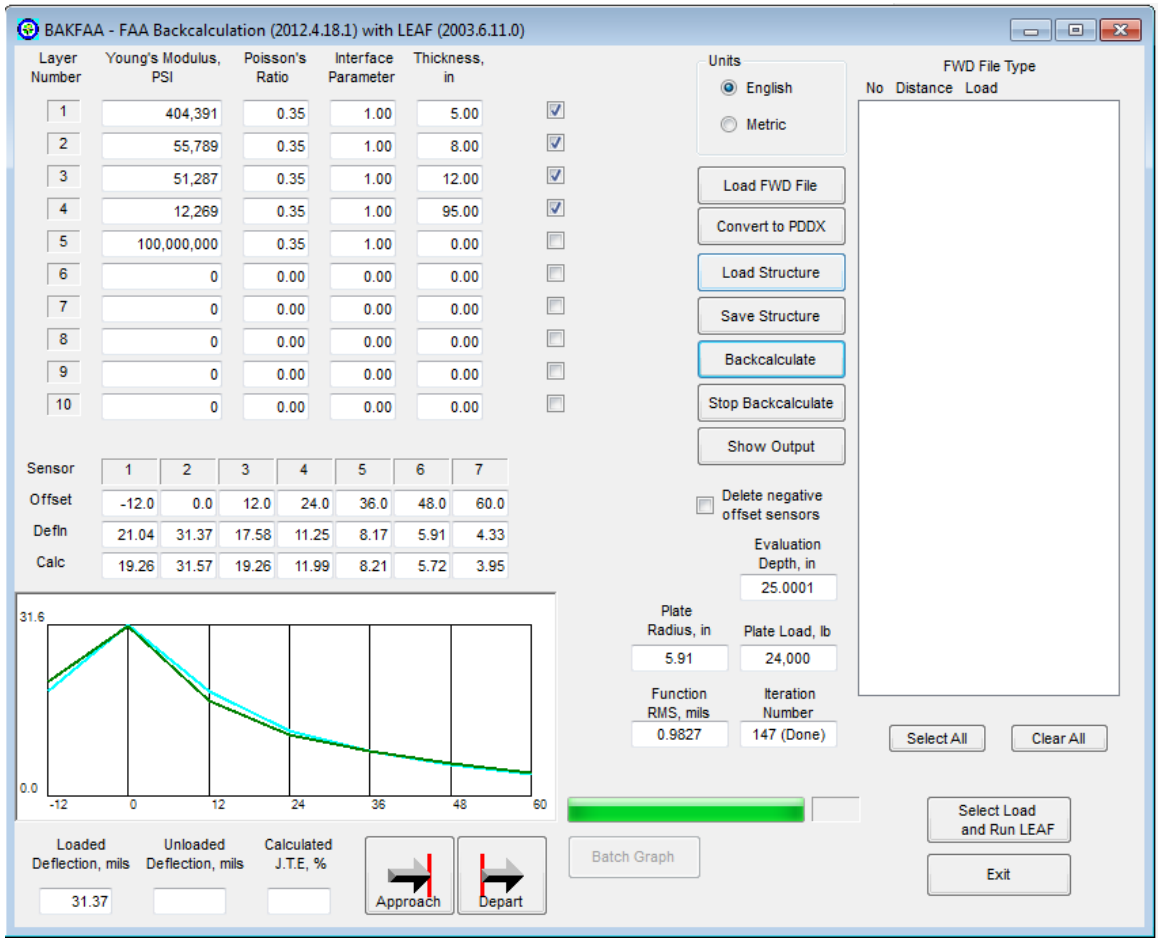

Figure 22: BAKFAA computer program display

Table 6: BAKFAA computer program inputs

Input	Value
Poisson's Ratio	0.35 (all layers)
Interface Parameter	1.00 (all layers)
Layer Thickness	Thickness of pavement layer in inches
Stiffness	Initial guess 100,000,000 psi input below subgrade (Assumed bedrock at the bottom)
Check-marked Boxes	Check if modulus allowed to vary
Offset	Offset of deflection sensors from load
Deflection	Deflection given in FWD data results
Plate Radius	5.91 inches
Plate Load	Load applied, in pounds

Analysis of FWD data using back-calculation requires several iterations in order to ensure accuracy of the modulus values obtained. In this thesis, FWD data were collected from the FAA's NAPTF website [26] by querying available FWD data for CC1, downloading FWD data off of a database provided by the FAA for CC3, and using FWD data files provided by the FAA for CC5. This data consisted of deflections measured at various dates, which correspond to loading passes, and at various positions along the NAPTF test track. Several FWD tests were conducted before testing, and then the remaining tests were conducted during various points during the application of loading, so not all loading passes have corresponding FWD data. Therefore, the N_{f50} value that is calculated is an approximate value.

Four sets of deflection values were measured by applying different plate loads at each test track position and loading pass for which FWD testing was conducted. The first and fourth sets of deflection values were measured by applying a plate load that is 32 to 36 kip. The second set of FWD deflection values were measured by applying a 10-12 kip load while the third set was measured by applying a plate load of 22-24 kip. The deflections from the first set were used to back-calculate seeding modulus values, which were then used as first guess values in the back-calculation of the modulus values using the second through fourth sets of deflections. The modulus values obtained from these deflection sets were averaged once the subgrade modulus was known and locked into place. These average values were considered to be the modulus values for the analyzed pavement structure after applying a particular number of loading passes.

Once the back-calculated modulus values have been obtained, the N_{f50} tensile strain was then estimated by first determining the load pass number after which the modulus of the pavement, as back-calculated from FWD data, reaches 50 percent of its initial value, known as N_{f50}. Strain data, collected from the NAPTF website or database as outlined in Appendix A, were then used to determine the peak tensile strain values as obtained from the various sensors placed within the HMA layer for crushed aggregate base sections or stabilized base layer for stabilized base sections, for the loading pass in question. The N_{f50} tensile strain was then computed as the average of the peak tensile strain values, at the N_{f50} loading pass, for each pavement section. This process is not perfect, however, as many factors can also attribute to changes in modulus, such as temperature, rutting, and the structure itself changing over time. A step-by-step procedure for estimating the N_{f50} tensile strain for FWD data is given as follows:

- Step 1: Determine the first estimate of back-calculated modulus by running BAKFAA until the program determines that RMSE is minimized.
- Step 2: In the current load pass, if the subgrade modulus values are fairly consistent (within about 10 percent), take the average of the subgrade values and repeat the back-calculation for each load, but lock the subgrade modulus to the average value obtained after step 1 and allow the higher layers to vary.
- Step 3: If consistent results in the surface, base, and/or subbase layers are seen (within about 20 percent), the average of the moduli values are considered as the modulus for each layer in the pavement structure. If swapping (i.e., one layer increases while another neighboring layer decreases, and vice versa) is seen between two layers, then another iteration is performed with the two layers combined and an equivalent value is obtained for these two layers.
- Step 4: The deflection values themselves are plotted against position for each load for different loading passes to examine behavior and to ensure that the back-calculation is giving meaningful results. For example, if the subgrade modulus increases, there should be a corresponding decrease in the outermost deflection.
- Step 5: Repeat steps 1 through 4 until a 50% reduction in the HMA modulus values are obtained.
- Step 6: Determine the number of passes for the HMA modulus to reach 50% of its initial value using the time and date of the FWD tests.
- Step 7: Determine the critical tensile strain as the average for the peak tensile strain values obtained from the strain gages for the load pass determined in Step 6. The fatigue endurance limit is a material property that cannot be determined

from field data. Since modulus degradation is taking place, all that can be concluded is that the load-induced tensile strain is higher than the fatigue endurance limit.

4.3 Compare Cycles to Failure from Backcalculation Results to RDEC Model

In order to verify the proposed approach for estimating the strain-based fatigue endurance limit from field FWD and tensile strain data, the N_{f50} tensile strain values obtained from the suggested approach were compared to those obtained from the refined RDEC model developed by Shen and Carpenter [6]. The RDEC model was used because it models the entire fatigue life of the pavement structure, and the binder mixes used to develop the RDEC model were similar to those used at the NAPTF. The RDEC model is defined by Equations 7 through 12 as presented previously in Chapter 2. Equations 8 and 9 are used in the procedure given below, and these equations will be re-stated here.

$$PV = 61.336\epsilon^{5.052}S^{2.749}VP^{1.643}GP^{-0.094} \quad \textit{Equation 8}$$

$$N_f = 0.4801PV^{-0.9007} \quad \textit{Equation 9}$$

To compute the RDEC model theoretical N_{f50} tensile strains that are representative of the pavement sections considered in this paper, the N_{f50} values determined from the FWD analysis were used in Equation 9 to obtain plateau values for each section. This equation represents a unique relationship between number of cycles to failure and plateau value that was determined by Shen and Carpenter [6]. The necessary mixture properties to compute VP and GP, the volumetric and gradation parameters, for the computation of the plateau values are presented in Table 5, found in section 3.5 of

this thesis. The plateau values obtained from Equation 9 are then used in Equation 8 to calculate the corresponding tensile strain which is considered the RDEC-based theoretical N_{f50} tensile strain. This strain is the theoretical tensile strain that would cause fatigue failure in the number of cycles determined from FWD testing. In addition, Equation 8 is used to calculate the theoretical fatigue endurance limit by entering $6.74x10^{-9}$ for PV and solving for the tensile strain.

4.4 Verify N_{f50} Tensile Strain Based on Backcalculated Moduli Using Strain Variability

To verify the FWD estimated N_{f50} tensile strains and make sure the obtained strain values are reasonable, the peak strain was plotted versus the number of loading cycles for all good strain data. The process of separating good strain data from bad strain data will be detailed in Appendix C. Using these plots, the pass number at which the variability in the data increased was used as an estimate of possible fatigue failure. The theory behind this process is that an increase in strain variability could be due to the strain gage recording the deformations caused by the development of a fatigue crack, or that the crack has caused the strain gage to fail. While variability increase may also be due to a number of other factors, such as an increase in rutting, temperature increase, or failure of the strain gage itself, the main purpose of examining variability was to serve as a check of whether the peak tensile strains, obtained for the loading pass where the variability increases, were similar to those obtained from the FWD data and the RDEC analyses. This check is performed due to the limited data available from the NAPTF.

In this study, the increase in strain data variability is objectively quantified utilizing changes in standard deviation of peak strain values. Specifically, the strain

values are separated into several sets. Each set constitutes of 1000 peak values obtained from their corresponding loading passes. For each set, the peak strain values are further subdivided into subsets; each consisting of 100 values, however, only the Track 0 passes are used from these subsets in order to account for variability due to wander track position. The standard deviation for each subset is then computed resulting in a total of 10 standard deviation values for each set. A two sample t-test is then conducted to compare the means of standard deviations for two consecutive sets of peak strain data. If the difference is determined to be significant, then the variability increase is said to occur at the loading pass where the significant difference in the mean of the standard deviation occurs.

Chapter 5

Analysis of Falling Weight Deflectometer Data

5.1 Introduction

The deflection data obtained from the Falling Weight Deflectometer (FWD) is utilized to estimate the modulus values of each layer in a pavement structure. The moduli can be obtained through the use of a back-calculation program such as BAKFAA, which was developed by the Federal Aviation Administration (FAA). Moduli can also be obtained through performing several iterations of a linear elastic program such as KENPAVE using a trial-and-error process. This process, however, is very tedious and that is why back-calculation programs are used. The use of such back-calculation programs, however, comes with limitations. For example, the program is simply a curve-fitting program which determines the modulus values that produce the least root-mean square difference between deflections obtained from linear elastic analysis and deflections obtained from the FWD. Therefore, it is important to not use BAKFAA or any other back-calculation program as a "black box", and instead ensure that the program is yielding realistic results; otherwise the outputs will not be reasonable and considered useless.

Loads distributed through soils are in the form of a cone. Therefore, at lower layers the load is distributed over a wider area. This means that the subgrade will affect the results of all deflection sensors, while upper layers will only have an effect on deflection sensors placed close to the applied load. Therefore, it is important to have confidence in the subgrade modulus before predicting the modulus values of higher layers.

The FWD device used by the FAA in this analysis is referred to as a Heavy Weight Deflectometer (HWD) due to the high plate loads applied. The HWD consists of seven deflection sensors, numbered D_0 through D_6. The deflection sensor labeled D_0 is located directly under the load, while the remaining sensors are offset from the load as given in Table 7. The locations of these loads are important because different pavement layers affect the deflections at various distances from the applied load. In the HWD analysis done on CC3 and CC5, there is also an eighth deflection sensor, D_7, which is 70.88 inches from the load. The locations of these loads are important because different pavement layers affect the deflections at various distances from the applied load.

Table 7: Offsets of FWD sensors from load

Sensor	D1	D0	D2	D3	D4	D5	D6
Offset (in.)	-11.81	0	11.81	23.62	35.43	47.24	59.06

In this chapter, a detailed approach for estimating the N_{f50} tensile strain using FWD and tensile strain data are presented. The value of N_{f50}, the number of cycles to failure, is determined from FWD analysis. From the number of cycles to failure, the corresponding tensile strain is determined from the strain gage data queried from the NAPTF website. The results of this analysis are then compared to the analysis of strain profile data, where the variability of peak strain data is examined. This additional analysis is completed in order to ensure that the tensile strain values obtained are reasonable.

5.2 FWD Raw Deflection Values

Raw FWD deflection data was obtained by querying FWD data from the NAPTF website for CC1 or from the database provided by the FAA for CC3. An example of raw FWD deflection data that was obtained for the pavement section labeled MFS is presented in Figure 23. As can be seen from this figure, the data was collected from FWD tests conducted at multiple times throughout the section's life. The deflection values obtained in June 1999 were lower than those obtained in June 2000. This was expected because in June 1999, this pavement section was first constructed with no loading applied. The modulus values obtained from this set of deflection data were considered the initial modulus values. These two dates were chosen to minimize temperature effects on backcalculated modulus values (pavement temperature on both dates is 73 degrees Fahrenheit). Temperature has a very large effect on backcalculated modulus, even more so than fatigue considering that winter modulus values were double those measured in summer. The 50 percent modulus reduction must therefore be calculated under similar temperature conditions.

As loading progressed, the FWD deflection values increased. This increase in deflection values suggests that there could be a reduction in the layer moduli of the pavement structure. Raw deflection graphs for MFC, LFS, and LFC in section CC1 are displayed in Figure 24 through Figure 26. Raw deflection graphs for sections LFC-1 and LFC-2 of CC3 are displayed in Figure 27 and Figure 28. The raw deflection graphs for section LFC-2 of CC5 are displayed in Figure 29 and Figure 30. Sections HFS and HFC in CC1 and LFC-3 and LFC-4 in both CC3 and CC5 were not examined, since no signs of fatigue were noticed in these sections. In each of these figures, deflections increase

from their initial values, signifying that a reduction in the modulus of the pavement layers have occurred in these layers as well. However, whether these pavement sections have reached N_{f50} must be determined through the use of BAKFAA.

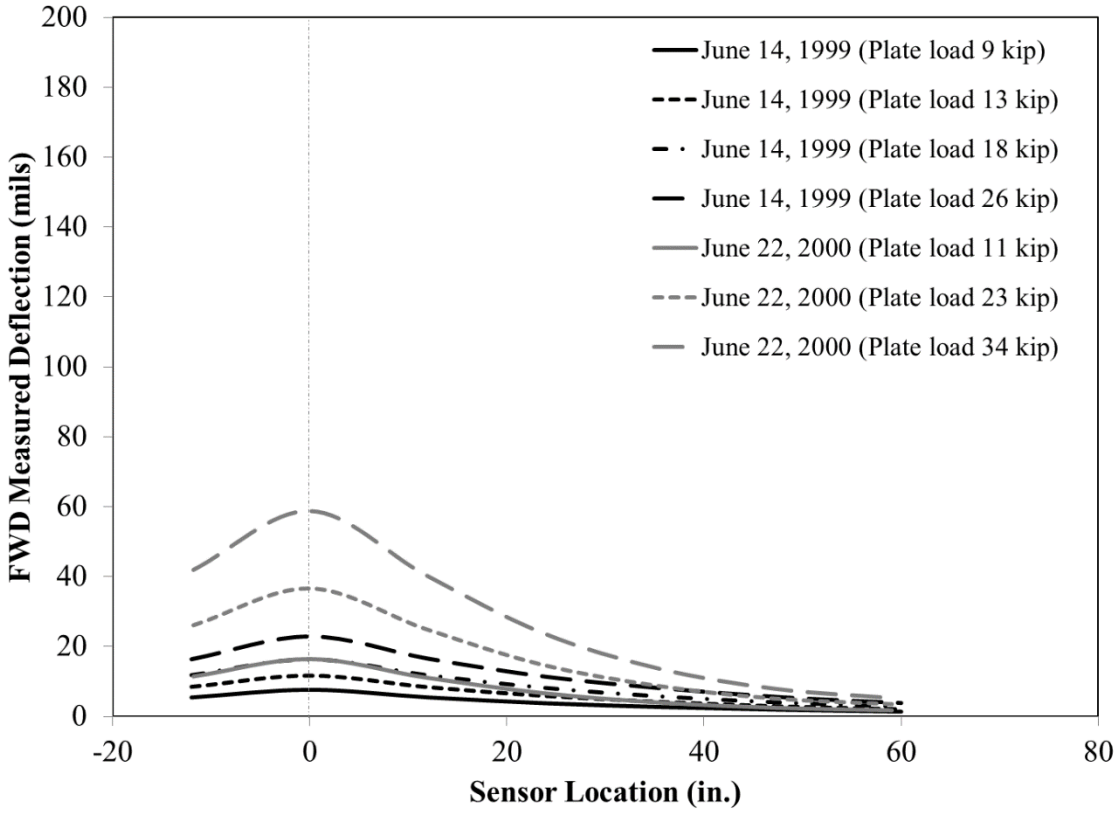

Figure 23: FWD raw deflection data for section MFS

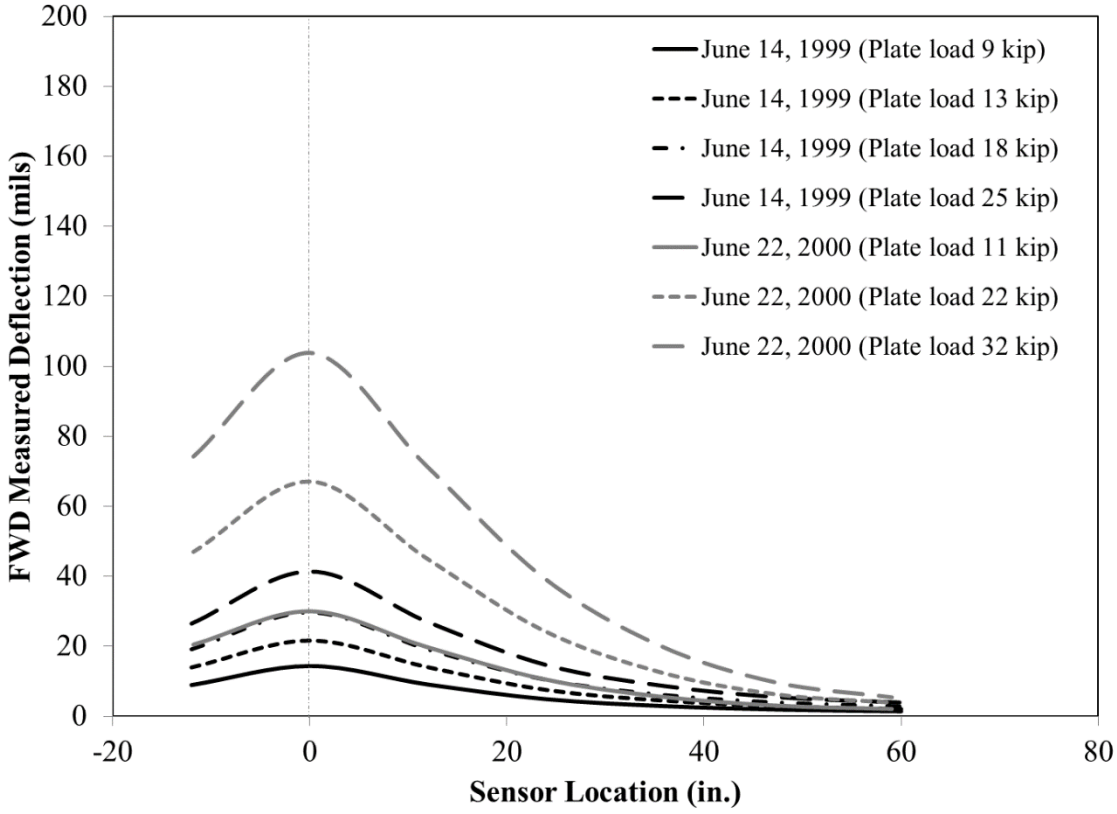

Figure 24: FWD raw deflection data for section MFC

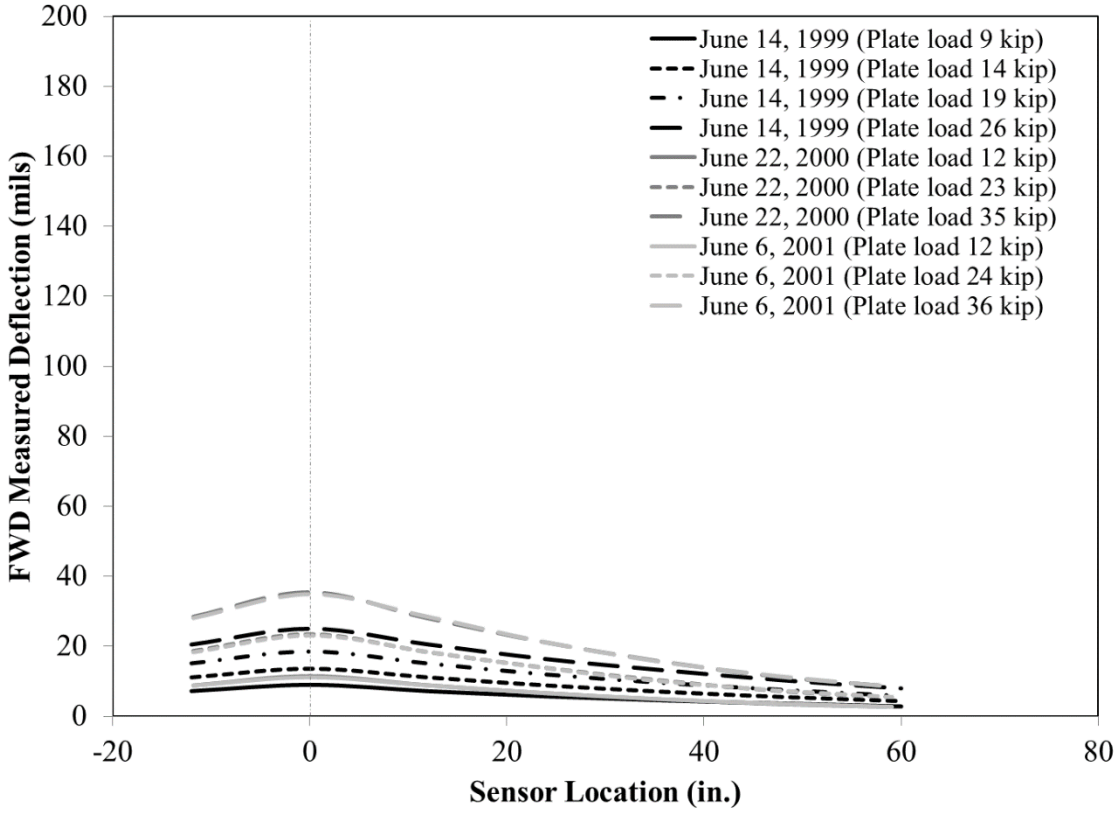

Figure 25: FWD raw deflection data for section LFS

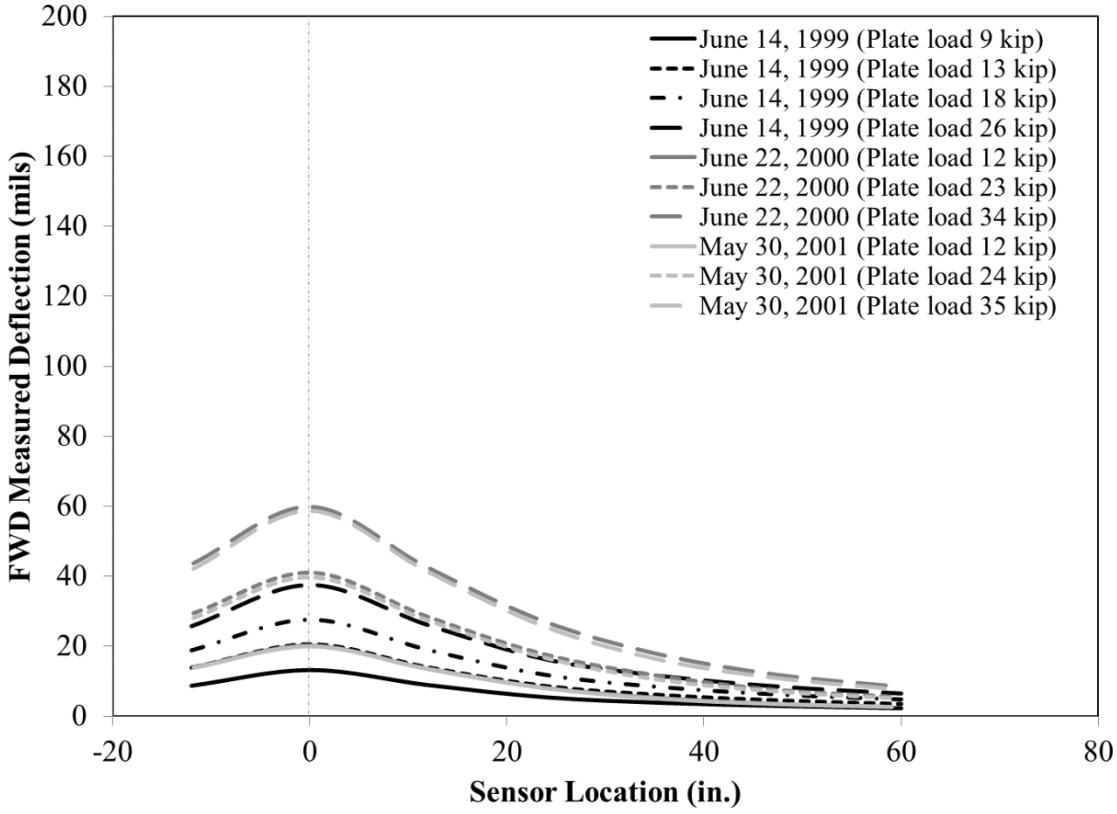

Figure 26: FWD raw deflection data for section LFC

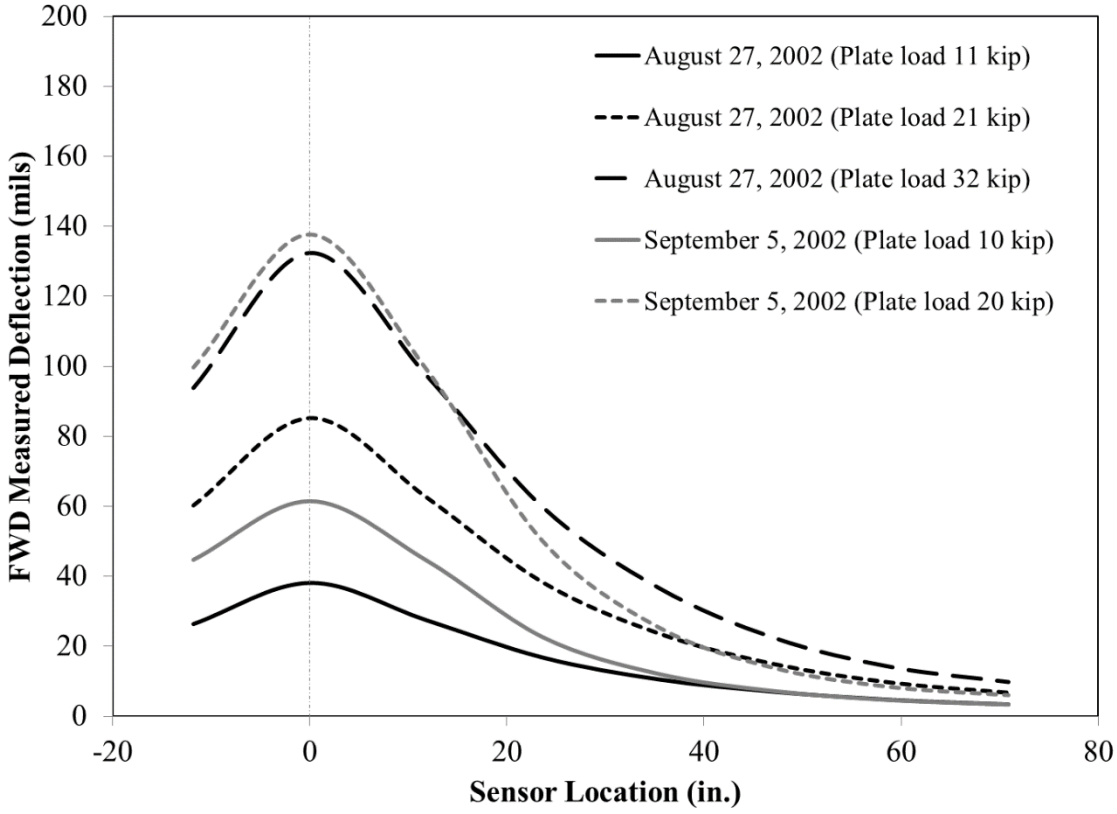

Figure 27: FWD raw deflection data for section LFC-1 (CC3)

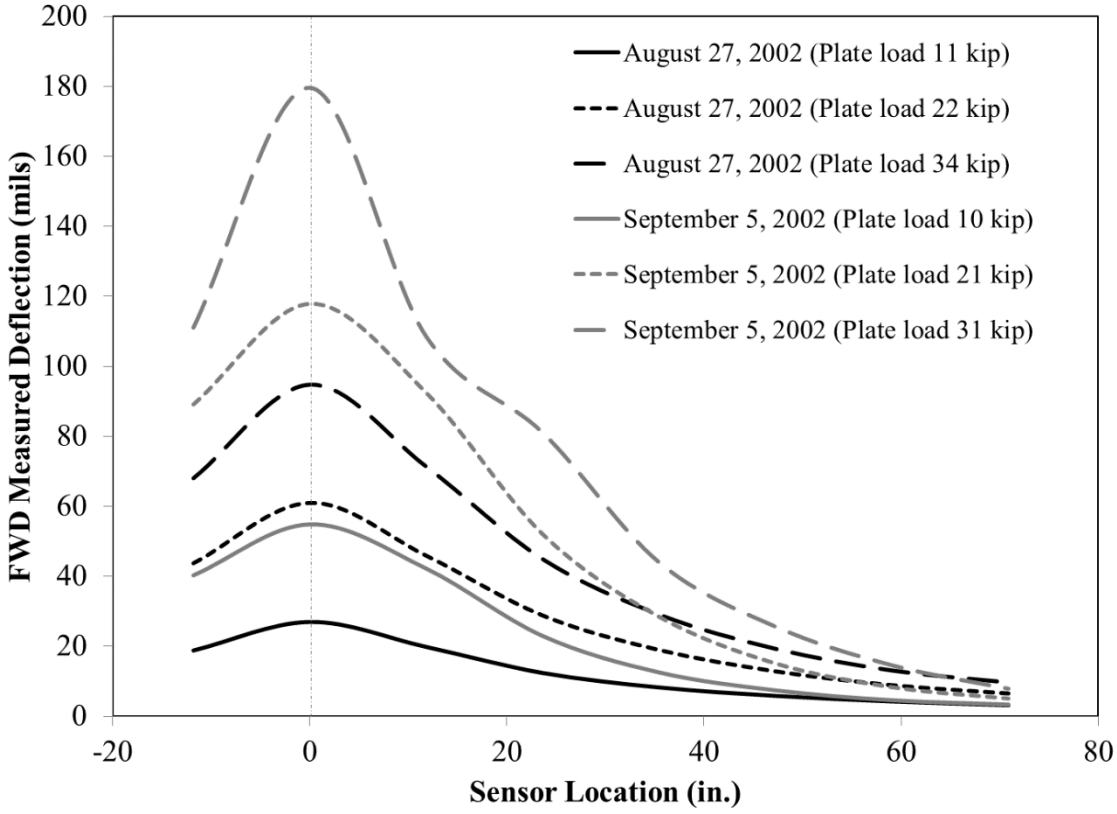

Figure 28: FWD raw deflection data for section LFC-2 (CC3)

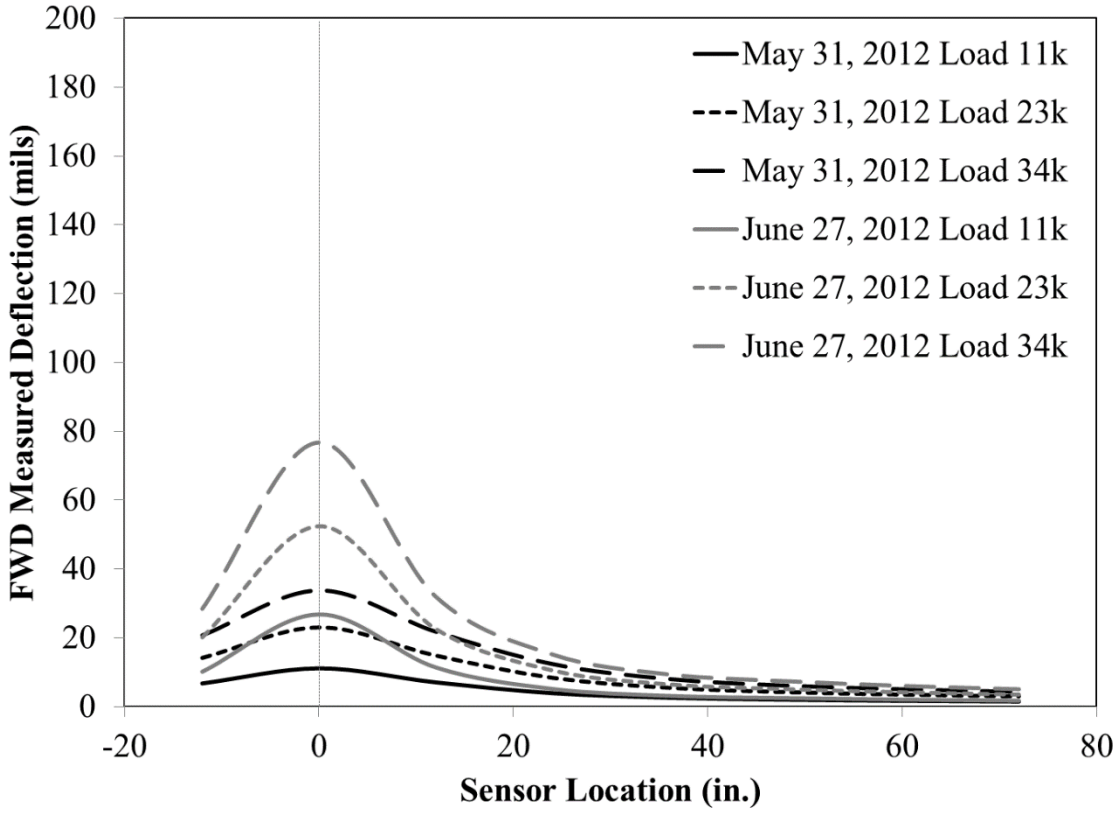

Figure 29: FWD raw deflection data for section LFC-2 SW (CC5)

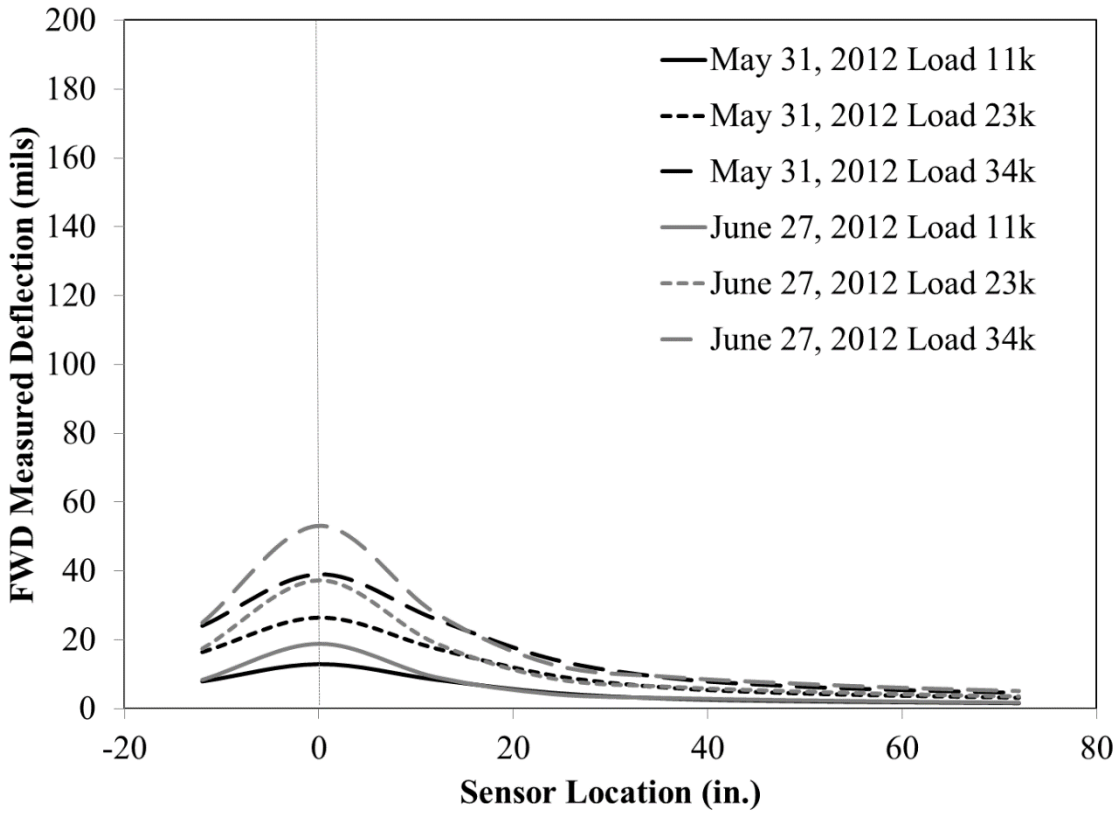

Figure 30: FWD raw deflection data for section LFC-2 SE (CC5)

5.3 Backcalculated Moduli

5.3.1 Pavement Section MFS (CC1)

Table 8 and Table 9 present the back-calculated moduli values computed for the MFS pavement section at various FWD testing times. The results presented in this table show that the modulus values decreased as loading progressed; confirming the observations made from Figure 23. Table 9 also shows a reduction of approximately 50 percent in the HMA layer modulus, signifying that for the MFS pavement section, fatigue failure occurred after applying about 14,688 loading passes, corresponding to the FWD testing on June 22, 2000. Pavement temperature on both dates was 73 degrees Fahrenheit.

Note also that the subbase modulus decreases over time, this could be attributed to a weakening asphalt layer reducing the confinement of the subbase.

Table 8: Modulus Values for MFS Pavement Section on June 14, 1999

Load (lb.)	HMA Modulus (psi)	Subbase Modulus (psi)	Subgrade Modulus (psi)
13,474	516,383*	30,674	14,500
18,444	505,944*	29,400	14,500
25,799	498,902*	29,771	14,500
Average	≈ 507,000	≈ 30,500	14,500

Table 9: Modulus Values for MFS Pavement Section on June 22, 2000

Load (lb.)	HMA Modulus (psi)	Subbase Modulus (psi)	Subgrade Modulus (psi)
11,243	269,325*	9,396	16,300
22,934	254,803*	6,494	16,300
34,069	240,732*	5,023	16,300
Average	≈ 255,000	≈ 7,000	16,300

*Combined surface and stabilized base HMA modulus.

5.3.2 Pavement Section LFC-1 (CC3)

Table 10 and Table 11 present the back-calculated moduli for the LFC-1 pavement section in CC3. This section experiences an approximately 50 percent reduction in the HMA layer modulus. Therefore, fatigue failure occurs on September 5, 2002, corresponding to 329 loading passes. Pavement temperatures on these dates were 81 degrees Fahrenheit on August 27 and 77 degrees Fahrenheit on September 5. The low number of passes to failure occurs due to the very thin subbase layer, causing poor support over a relatively weak subgrade layer.

Table 10: Modulus Values for LFC-1 Pavement Section on August 27, 2002

Load (lb.)	HMA Modulus (psi)	Base Modulus (psi)	Subbase Modulus (psi)	Subgrade Modulus (psi)
10,524	354,728	12,133	9,601	4,625
21,429	411.078	7,979	7,484	4,625
32,216	435,432	5,870	7,649	4,625
Average	≈400,000	≈8,700	≈8,200	4,625

Table 11: Modulus Values for LFC-1 Pavement Section on September 5, 2002

Load (lb.)	HMA Modulus (psi)	Base Modulus (psi)	Subbase Modulus (psi)	Subgrade Modulus (psi)
10,304	262,564	2,379	6,497	4,625
20,119	213,856	3,292		4,625
19,874	214,480	2,761		4,625
Average	≈230,000	≈2,900		4,625

5.3.3 Pavement Section LFC-2 (CC3)

Table 12 and Table 13 present the back-calculated moduli for the LFC-2 pavement section in CC3. Like section LFC-1, this section experiences 50 percent reduction in the HMA layer modulus. Therefore, fatigue failure also occurs on September 5, 2002, corresponding to 329 loading passes. Like in the case of section LFC-1, the subbase is very thin, resulting in poor support, which causes the HMA pavement layer to fail quickly.

Table 12: Modulus Values for LFC-2 Pavement Section on August 27, 2002

Load (lb.)	HMA Modulus (psi)	Base Modulus (psi)	Subbase Modulus (psi)	Subgrade Modulus (psi)
10,779	559,133	15,350		5,300
22,361	617,069	12,026		5,300
33,599	624,213	10,961		5,300
Average	≈600,000	≈13,000		5,300

Table 13: Modulus Values for LFC-2 Pavement Section on September 5, 2002

Load (lb.)	HMA Modulus (psi)	Base Modulus (psi)	Subbase Modulus (psi)	Subgrade Modulus (psi)
10,433	336,036	4,198		4,700
20,922	381,374	3,067		4,700
31,409	227,456	5,723		4,700
Average	≈315,000	≈4,300		4,700

5.3.4 Pavement Section MFC (CC1)

Table 14 and Table 15 present the back-calculated moduli for the MFC pavement section. While the previous three sections reached $N_{f50,}$ this section and the two that follow it do not reach N_{f50}. In this pavement section, the HMA layer modulus is not reduced by 50 percent. This signifies that fatigue cracking likely did not occur in this pavement section.

Table 14: Modulus Values for MFC Pavement Section on June 14, 1999

Load (lb.)	HMA Modulus (psi)	Base Modulus (psi)	Subbase Modulus (psi)	Subgrade Modulus (psi)
13,346	561,271	20,759	30,711	13,700
18,292	604,279	16,051	41,134	13,700
25,510	613,971	15,955	40,399	13,700
Average	≈593,000	≈17,500	≈37,500	13,700

Table 15: Modulus Values for MFC Pavement Section on June 22, 2000

Load (lb.)	HMA Modulus (psi)	Base Modulus (psi)	Subbase Modulus (psi)	Subgrade Modulus (psi)
10,983	484,491	11,686	5,444	13,700
21,850	364,251	19,926	3,221	13,700
32,197	392,361	18,061	2,710	13,700
Average	≈414,000	≈16,500	≈3,800	13,700

5.3.5 Pavement Section LFS (CC1)

Table 16 and Table 17 present the back-calculated moduli for the LFS pavement section. Like in section MFC, the HMA layer modulus does not experience a 50 percent reduction in modulus. Therefore, fatigue cracking most likely did not occur in this section. The reason this section did not reach N_{f50} while section MFS did is likely due to the fact that the LFS pavement section has a significantly thicker subbase layer, 29.6 inches thick compared to the MFS pavement which has a subbase that is only 8.5 inches thick.

Table 16: Modulus Values for LFS Pavement Section on June 14, 1999

Load (lb.)	HMA Modulus (psi)	Subbase Modulus (psi)	Subgrade Modulus (psi)
13,654	627,910*	32,244	9,600
18,741	609,465*	31,519	9,600
25,875	614,417*	31,637	9,600
Average	≈617,000	≈31,800	9,600

Table 17: Modulus Values for LFS Pavement Section on June 6, 2001

Load (lb.)	HMA Modulus (psi)	Subbase Modulus (psi)	Subgrade Modulus (psi)
12,452	732,435*	25,405	10,500
24,353	704,261*	22,195	10,500
36,407	760,932*	19,228	10,500
Average	≈732,000	≈22,000	10,500

*Combined surface and stabilized base HMA modulus.

5.3.6 Pavement Section LFC (CC1)

Table 18 and Table 19 present the back-calculated moduli for the LFC pavement section in CC1. Like the two previous pavement sections, no reduction of 50 percent of HMA modulus took place. However, when looking at the back-calculated modulus values for the un-trafficked center lane on May 30, 2001, they are double the modulus values in the wheel path, suggesting a possible N_{f50}; however, this can be attributed to rutting in the trafficked pavement section, changes in temperature, and possible stiffening over time of the un-trafficked center lane. For this thesis, it will be stated that no N_{f50} value occurs here, as the modulus of the trafficked lane does not decrease by 50 percent. As will be seen in the next subsection, no good strain data is available for the LFC pavement section on May 30, 2001, corresponding to 35,763 loading passes, so an N_{f50} tensile strain cannot be calculated even if this date is taken to be the date where N_{f50} occurs.

Table 18: Modulus Values for LFC Pavement Section on June 14, 1999

Load (lb.)	HMA Modulus (psi)	Base Modulus (psi)	Subbase Modulus (psi)	Subgrade Modulus (psi)
8,847	683,575	28,670		7,100
13,456	725,491	26,774		7,100
18,350	784,358	26,595		7,100
Average	≈731,000	≈27,300		7,100

Table 19: Modulus Values for LFC Pavement Section on May 30, 2001

Load (lb.)	HMA Modulus (psi)	Base Modulus (psi)	Subbase Modulus (psi)	Subgrade Modulus (psi)
12,222	749,501	20,834		9,700
23,875	822,508	19,298		9,700
35,384	904,571	18,626		9,700
Average	≈826,000	≈19,500		9,700

5.3.7 Pavement Section LFC-2 (CC5)

Table 20 and Table 21 present the back-calculated moduli for section LFC-2 SW of CC5, while Table 22 and Table 23 present the back-calculated moduli for section LFC-2 SE. Both of these sections appear to reach N_{f50} on June 27, 2012, when compared to FWD testing performed on May 31, 2012. Trafficking on LFC-2 did not begin until August 21, 2012. Therefore, the drop in modulus may be due to pre-trafficking tests performed on the section.

Table 20: Modulus Values for LFC-2 SW Pavement Section on May 31, 2012

Load (lb.)	HMA Modulus (psi)	Base Modulus (psi)	Subbase Modulus (psi)	Subgrade Modulus (psi)
11,815	841,998	43,042	50,966	14,000
23,835	818,639	48,815	43,939	14,000
35,065	842,160	46,428	44,991	14,000
Average	≈834,000	≈46,100	≈46,600	14,000

Table 21: Modulus Values for LFC-2 SW Pavement Section on June 27, 2012

Load (lb.)	HMA Modulus (psi)	Base Modulus (psi)	Subbase Modulus (psi)	Subgrade Modulus (psi)
11,276	91,402	27,907	25,957	14,000
22,669	92,668	30,053	25,843	14,000
33,275	82,163	32,247	26,928	14,000
Average	≈88,700	≈30,100	≈26,200	14,000

Table 22: Modulus Values for LFC-2 SE Pavement Section on May 31, 2012

Load (lb.)	HMA Modulus (psi)	Base Modulus (psi)	Subbase Modulus (psi)	Subgrade Modulus (psi)
11,680	749,900	39,651	36,080	14,000
23,570	770,640	41,369	33,285	14,000
34,647	717,850	47,481	31,588	14,000
Average	≈746,000	≈42,800	≈33,700	14,000

Table 23: Modulus Values for LFC-2 SE Pavement Section on June 27, 2012

Load (lb.)	HMA Modulus (psi)	Base Modulus (psi)	Subbase Modulus (psi)	Subgrade Modulus (psi)
11,291	263,678	20,766	46,713	14,000
23,030	190,783	42,154	31,303	14,000
33,907	234,686	36,294	34,149	14,000
Average	≈230,000	≈33,100	≈37,400	14,000

5.4 Determination of N_{f50} Tensile Strain

Three of the six pavement sections examined reached a 50 percent reduction in HMA modulus, while the other three did not. The sections that reached N_{f50} are section MFS in CC1 and sections LFC-1 and LFC-2 in CC3. For each of these pavement sections, the tensile strain at N_{f50} will be determined based on the tensile strain data at the loading pass where N_{f50} occurs.

5.4.1 Pavement Section MFS (CC1)

To determine the value of the N_{f50} tensile strain for section MFS in CC1, which is the only CC1 pavement section that reached N_{f50}, the strain profiles obtained from good longitudinal sensors (i.e., MBS1, MBS2, and MBS3) located in the MFS pavement section were plotted (Figure 31) for load pass number 14,688, which is the loading pass that corresponds to the date June 22, 2000, when N_{f50} was reached. As can be seen from Figure 31, the peak strain values obtained from all sensors were averaged and the computed N_{f50} tensile strain was determined to be approximately 658 με for section MFS.

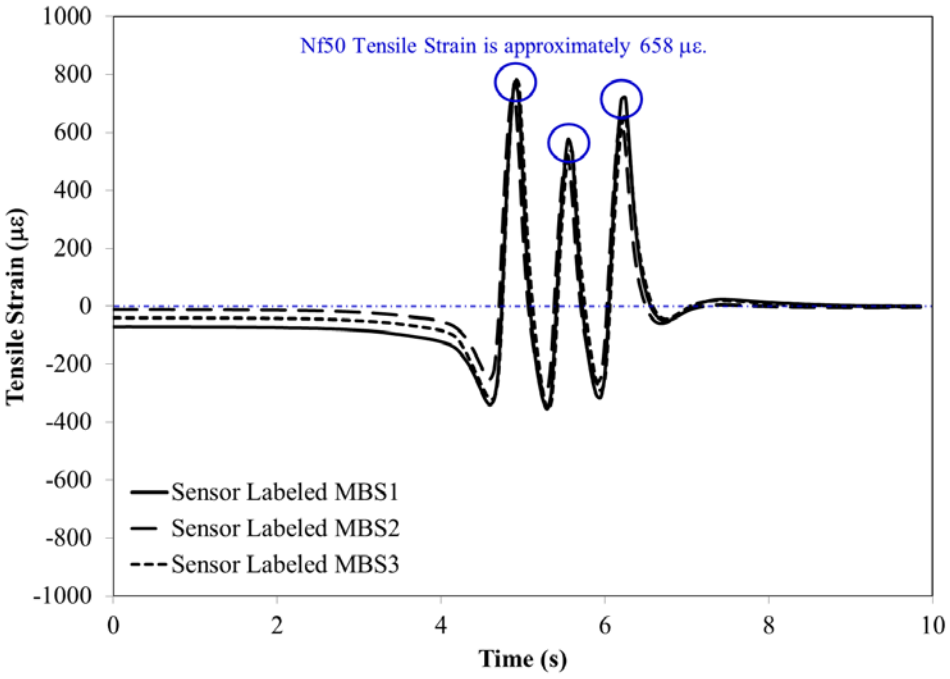

Figure 31: Strain profiles obtained at loading pass number 14688 for MFS pavement section

5.4.2 Pavement Section LFC-1 (CC3)

The pavement section labeled LFC-1 in CC3 reached a 50 percent reduction in modulus on September 5, 2002, corresponding to 329 loading passes. However, strain data for sensors in this pavement section are only available for up to about 100 loading passes, so a tensile strain at N_{f50} cannot be calculated for this pavement section.

5.4.3 Pavement Section LFC-2 (CC3)

To determine the value of the N_{f50} tensile strain for section LFC-2 in CC3, the strain profile obtained from the longitudinal sensor on the LFC-2 north track, sensor ASG-18, was plotted (Figure 32) for load pass number 329, which is the loading pass that corresponds to the date September 5, 2002, when N_{f50} was reached. As can be seen from

Figure 32, the peak strain values obtained from all sensors were averaged and the N_{f50} tensile strain was determined to be approximately 459 με for section LFC-2.

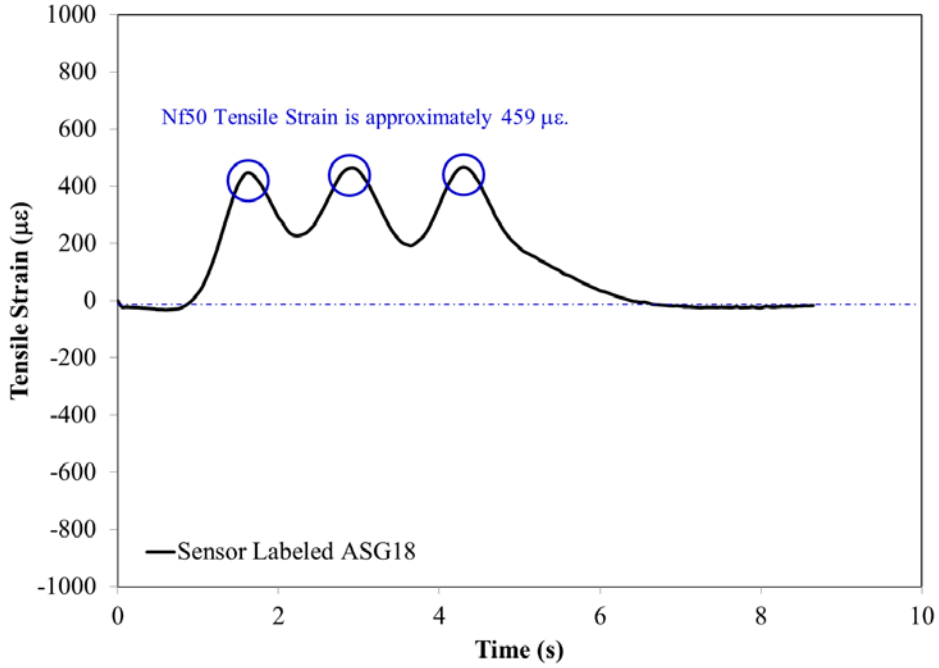

Figure 32: Strain profiles obtained at loading pass number 329 for LFC-2 pavement section

5.5 Comparison of FWD Results to Strain Data Variability

In addition to the FWD analysis, variability of peak tensile strain was analyzed as a tool to identify initiation of cracking. After about 23,000 loading passes in low-strength subgrade (Figure 33) and about 9,000 loading passes in medium-strength subgrade (Figure 34), the peak strains start to become more variable. For the MFS section, this variability increase corresponds to approximately 500 με. This value is slightly lower than what was determined using the proposed FWD approach (about 658 με) and the

RDEC model (580 με). For the LFC-2 section in CC3, strain variability increases after only 100 loading passes (Figure 35). This corresponds to a tensile strain of 650 με.

To quantify the point at which there is a significant increase in variability, the standard deviation approach described in Chapter 4 was followed. Table 24 displays the pass groups where there is a significant difference in the mean of the standard deviation for selected CC1 sensors, while Table 25 displays the pass groups where there is a significant difference in the mean of the standard deviation for selected CC3 sensors. Table 26 displays the standard deviation test results for selected CC5 sensors. Note that in some sensors there is no significant variability increase. Strain values at which the standard deviation increases are given in Table 27, and are also illustrated in Figure 33 through Figure 35. The significance of the increase in variability in relation to the tensile strain at N_{f50} is that an increase in strain variability is a possible indicator of cracking. This can be only used as a check; however, since variability increase can also be attributed to temperature changes and strain gage failure or de-bonding.

Table 24: Standard Deviation Test Results from Selected CC1 Sensors

Sensor	Pass Group 1	Avg. of Std. Dev.	Pass Group 2	Avg. of Std. Dev.
LBS3 (LFS)	21000-22000	35.1	23000-24000	63.4
LBS11 (LFS)	21000-22000	17.0	23000-24000	43.0
MBS2 (MFS)	7000-8000	13.7	9000-10000	29.0
MBS10 (MFS)	7000-8000	16.0	9000-10000	28.8
LSC3 (LFC)	5000-6000	68.1	7000-8000	152.6

Table 25: Standard Deviation Test Results from Selected CC3 Sensors

Sensor	Pass Group 1	Avg. of Std. Dev.	Pass Group 2	Avg. of Std. Dev.
ASG-23 (LFC-3)	3200-4200	25.2	4200-5200	37.7
ASG-28 (LFC-4)	3500-4500	56.9	4500-5500	80.2
ASG-33 (LFC-4)	3500-4500	98.7	4500-5500	127.4
ASG-35 (LFC-4)	3600-4600	18.6	4600-5600	25.7

Table 26: Standard Deviation Test Results from Selected CC5 Sensors

Sensor	Pass Group 1	Avg. of Std. Dev.	Pass Group 2	Avg. of Std. Dev.
ASG-1 (LFC-1N)	No variability increase	None	No variability increase	None
ASG-2 (LFC-1N)	No variability increase	None	No variability increase	None
ASG-9 (LFC-3S)	12000-13000	57.5	13000-14000	118.8
ASG-10 (LFC-3S)	12000-13000	86.3	13000-14000	179.7

Table 27: Strain Values at Variability Increase

Section	Loading Passes of Std. Dev. Increase	Strain at Std. Dev. Increase (με)
LFS (CC1)	23000	520
MFS (CC1)	9000	500
LFC-2 (CC3)	100	650

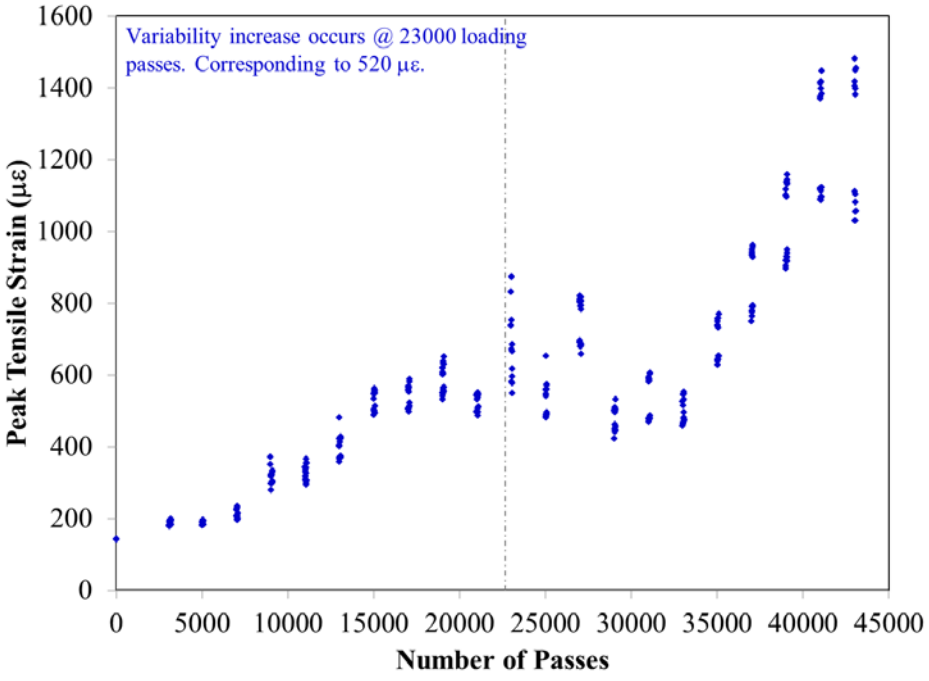

Figure 33: Peak tensile strain variability for LFS pavement section

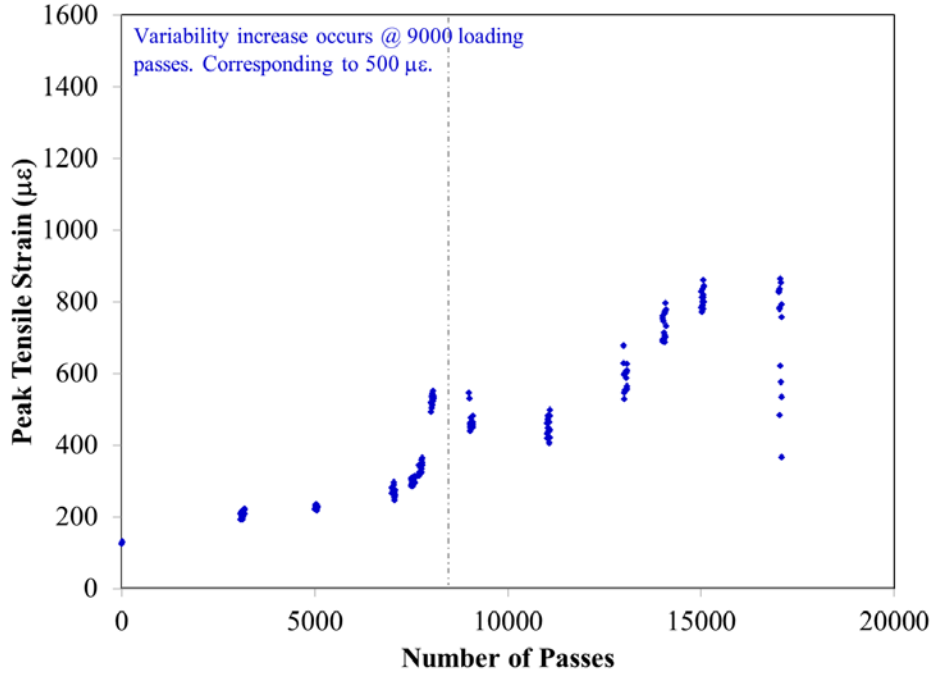

Figure 34: Peak tensile strain variability for MFS pavement section

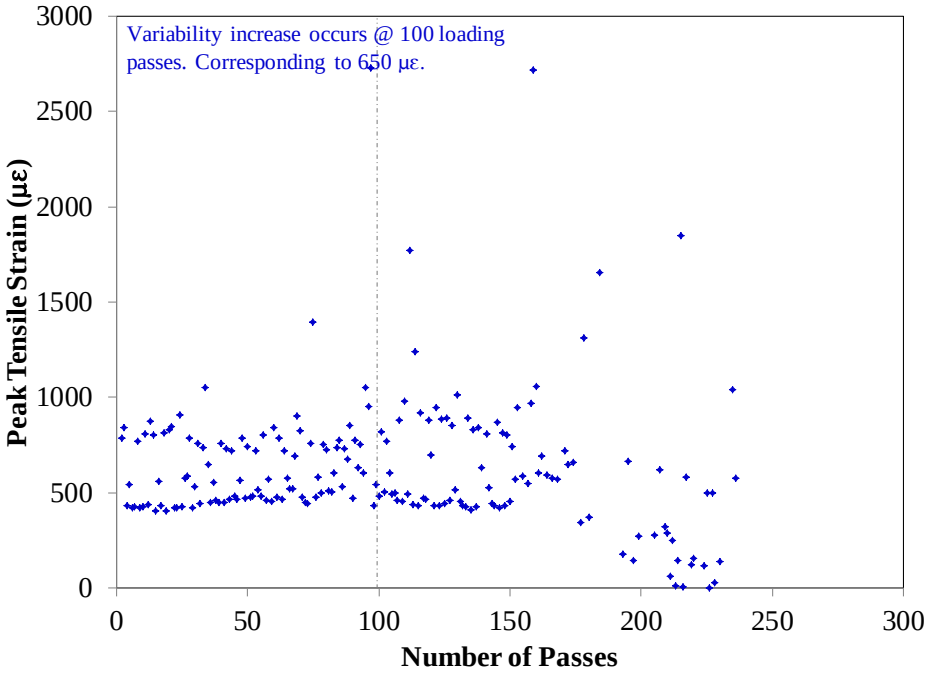

Figure 35: Peak tensile strain variability for section LFC-2.

Chapter 6

Comparison of RDEC Model to Proposed Approach

6.1 Introduction

This chapter discusses the RDEC model and how the theoretical N_{f50} tensile strain is determined from the model equations given the number of cycles to failure obtained from the FWD-based approach. Once the theoretical tensile strain is obtained, it will be compared to the N_{f50} tensile strain obtained from the FWD-based approach and the strain value obtained from the strain data variability approach.

6.2 Obtaining Theoretical N_{f50} Tensile Strain from RDEC Model

6.2.1 Calculation of Stiffness using Witczak Predictive Equation for HMA

To get the stiffness values for the RDEC equations, a set of calculations using the Witczak predictive equation was utilized. This equation, which is Equation 13 below, takes the material properties of the asphalt and predicts the modulus value E*. [7]

$$\log E^* = 3.750063 + 0.02932\rho_{200} - 0.001767\rho_{200}^2 - 0.002841\,\rho_4 - 0.058097V_a - 0.802208 * \frac{V_{b,eff}}{V_{b,eff}+V_a} + \frac{3.871977-0.0021\rho_4+0.003958\rho_{38}-0.000017\rho_{38}^2+0.00547\rho_{34}}{1+e^{-0.603313-0.313351\log f-0.393532\log \eta}} \qquad \textit{Equation 13}$$

The variables ρ_{34},ρ_{38}, and $\rho_4$stand for the percent of particles *retained* on the ¾ inch, 3/8 inch, and No. 4 sieves, respectively, while the variable ρ_{200}stands for the percent of particles *passing* the No. 200 sieve. The variable V_a is the volumetric percent of air voids, while the variable $V_{b,eff}$is the volumetric percent effective binder content. The variable f stands for frequency in Hertz (10 Hz is used for the RDEC model), while η is the dynamic viscosity in millions of Poise, calculated using Equation 14. Values

were obtained based on P-401 properties in section LFS in CC1, found in Tables B-1 and B-5 in Appendix B. Average values were used for base and surface.

$$\eta = \log(\log(A + VTS \log T_R)) \qquad \textit{Equation 14}$$

The parameters A and VTS are obtained based on the type of asphalt. [8] In this case, AC-20 asphalt is assumed. T_R is the temperature in Rankine, which is an absolute temperature scale with units equal to Fahrenheit degrees. T_R is equal to the temperature in Fahrenheit plus 459. 20 degrees Celsius, used for the RDEC model, is equivalent to 68 degrees Fahrenheit or 527 Rankine degrees. A table of inputs is given in Table 28 and Table 29 below. Viscosity is obtained in centipoise, which must be divided by 10^8 to obtain millions of Poise for Equation 13.

Table 28: Inputs for Witczak equation

Parameter	Value
Frequency (Hz)	10
Percent air voids	2.8
Percent effective binder content	10.88
Percent retained on ¾" sieve	0.4
Percent retained on 3/8" sieve	12.4
Percent retained on No. 4 sieve	41.2
Percent passing No. 200 sieve	6

Table 29: Inputs for viscosity equation

Parameter	Value
A	10.7709
VTS	-3.6017
Temperature (Fahrenheit)	68
Temperature (Rankine)	527
Viscosity (cP)	1.924E+07
Viscosity (x10^6 Poise)	19.24

Equation 13 is broken into four parts:

$$\mathrm{A} = 3.750063 + 0.02932\rho_{200} - 0.001767\rho_{200}^2 - 0.002841\,\rho_4 - 0.058097V_a$$

$$B = 0.802208 * \frac{V_{b,eff}}{V_{b,eff}+V_a}$$

$$C = 3.871977 - 0.0021\rho_4 + 0.003958\rho_{38} - 0.000017\rho_{38}^2 + 0.00547\rho_{34}$$

$$D = -0.603313 - 0.313351\log f - 0.393532\log\eta$$

The equations are then combined in the following way:

$$\log E^* = A - B + \frac{C}{1+e^D} \qquad \textit{Equation 15}$$

Calculations:

$$\mathrm{A} = 3.750063 + 0.02932(6) - 0.001767(6)^2 - 0.002841\,(41.2) - 0.058097(2.8) = 3.58265$$

$$B = 0.802208 * \frac{10.88}{10.88+2.8} = 0.638013$$

$$C = 3.871977 - 0.0021(41.2) + 0.003958(12.4) - 0.000017(12.4)^2 + 0.00547(0.4) = 3.83411$$

$$\eta = \log\{\log[10.7709 + (-3.6017)\log(527)]\} = 19.24946\ Poise \times 10^6$$

$$D = -0.603313 - 0.313351\log(10) - 0.393532\log(19.24946) = -1.42212$$

Now that the parameters *A*, *B*, *C*, and *D* have been calculated, Equation 15 is then used to find the stiffness.

$$\log E^* = 3.58265 - 0.638013 + \frac{3.83411}{1+e^{-1.42212}} = 6.033669$$

$$E = 1080610\ psi = 7450\ MPa$$

Based on the results of the Witczak equation, the stiffness should be equal to about 1,080,000 psi, or 7450 MPa. With a frequency of 0.5 Hz, the stiffness is only about 573,000 psi, or 3950 MPa. This explains why the stiffness values input to the RDEC equations in Table 30 are approximately double the back-calculated modulus values determined from using BAKFAA on initial testing. Pavement temperatures when back-calculating the modulus values on the dates listed in Chapter 5 range from 73 to 81 degrees Fahrenheit (23 to 27 degrees Celsius), which is near 20 degrees Celsius. As a result, the back-calculated moduli have to be adjusted by a factor of about 7450/3950, or 1.886, when used in the RDEC equations.

6.2.2 Pavement Section MFS (CC1)

The N_{f50} tensile strain determined for the MFS pavement section was compared to the RDEC theoretical N_{f50} tensile strain. The RDEC plateau value was computed using Equation 9 assuming that the number of cycles to crack failure (N_f) was equal to 14,688. Equation 8 was then used to compute the RDEC theoretical tensile strain. The parameters used in Equation 8 (which include stiffness, volumetric parameter, gradation parameter, air voids, binder content, and percent passing nominal maximum sieve, critical sieve, and No. 200 sieve) for all sections considered in this paper are summarized in Table 30. Stiffness (S parameter in Equation 8 of RDEC model) values are converted to 10 Hz and

20 degrees Celsius through the use of the Witczak predictive equation. This process was outlined in the previous subsection. It is noted that this process was used for all sections when computing the RDEC theoretical N_{f50} tensile strain. Calculations used to determine the theoretical tensile strain at N_{f50} for section MFS are given below:

$$N_f = 0.4801 PV^{-0.9007}$$

$$14688 = 0.4801 PV^{-0.9007}$$

$$PV = 1.05 \times 10^{-5}$$

$$PV = 61.336 \epsilon^{5.052} S^{2.749} VP^{1.643} GP^{-0.094}$$

$$1.05 \times 10^{-5} = 6.1336 \epsilon^{5.052} (6550\ MPa)^{2.749} (0.310)^{1.643} (5.864)^{-0.094}$$

$$\epsilon = 0.000580 = 580\ \mu\epsilon$$

The RDEC theoretical N_{f50} tensile strain (580 με) was 11.8 percent lower than the FWD N_{f50} tensile strain (658 με). These results indicate that the suggested approach might be a viable method for estimating the tensile strain at N_{f50} of asphalt pavements. It is noted that the N_{f50} tensile strains using the proposed FWD-based approach and the RDEC model are higher than the fatigue endurance limit range defined by Shen and Carpenter (i.e., 70 to 350 με). This is could be attributed to the lower rate of loading and longer rest periods utilized in the accelerated testing facility causing the NAPTF sections to fail at a higher fatigue endurance limit than those in the laboratory. In addition, when the plateau value is plotted versus number of cycles to failure, as will be seen in the next section, the data points fall within the normal strain regime.

6.2.3 Pavement Sections LFC-1 and LFC-2 (CC3)

Since these pavement sections have the same input properties (the same as section LFC of CC1) and the same value for N_{f50}, they have the same theoretical N_{f50} tensile strain, which is calculated below:

$$N_f = 0.4801 PV^{-0.9007}$$

$$329 = 0.4801 PV^{-0.9007}$$

$$PV = 7.10 \times 10^{-4}$$

$$PV = 61.336 \epsilon^{5.052} S^{2.749} VP^{1.643} GP^{-0.094}$$

$$7.10 \times 10^{-4} = 6.1336 \epsilon^{5.052} (8160\ MPa)^{2.749} (0.310)^{1.643} (5.593)^{-0.094}$$

$$\epsilon = 0.001186 = 1186\ \mu\epsilon$$

Using the RDEC equations, this theoretical N_{f50} tensile strain was determined to be 1186 με. This value is much higher than that obtained from the FWD-based method (459 με). This high value is attributed to the low number of cycles to failure obtained from back-calculation of FWD deflection data. These results suggest that the RDEC model may not be a good predictor of fatigue cracking when the number of cycles to failure is very low, i.e. only a few hundred loading passes.

Table 30: Plateau values and tensile strains using RDEC model corresponding to N_{f50} obtained from FWD testing

Parameter	LFS*	LFC	MFS	MFC*	LFC-1 and 2
PV	2.75E-06	3.93E-06	1.05E-05	9.68E-06	7.10E-04
S** (ksi)	1180.6	1183.5	950.0	956.0	1183.5
VP	0.299	0.310	0.310	0.335	0.310
GP	5.733	5.593	5.864	5.610	5.593
Theoretical N_{f50} Tensile Strain (με)	400	424	580	555	1186
N_{f50}	48882	35463	14688	15758	329
AV (%)	4.7	4.8	4.7	5.4	4.8
V_b (%)	10.88	10.68	10.48	10.74	10.74
P_{NMS} (%)	93.2	93.0	93.0	93.0	93.0
P_{PCS} (%)	58.8	60.0	58.4	59.9	60.0
P_{200} (%)	6.0	5.9	5.9	5.9	5.9

* Section did not reach N_{f50}. Values were computed using final loading pass after trafficking was completed.

** Stiffness is for a frequency of 10 Hz and 20 °C. Loading was performed at 0.5 Hz and various temperatures. Equations used units of MPa, but English units are presented for consistency.

6.3 RDEC Fatigue Endurance Limit

For the sections that reached N_{f50} (section MFS of CC1 and section LFC-2 of CC3), the theoretical RDEC fatigue endurance limit was also calculated using a plateau value of 6.74×10^{-9}. These results are displayed in Table 31. Based on this table, the average FEL for the NAPTF mix is 128 με. The two values in the table come as the result of slight differences in the material properties of the different lifts of the NAPTF mix.

Table 31: RDEC theoretical fatigue endurance limits

Parameter	MFS	LFC1
PV	6.74E-09	6.74E-09
S^* (ksi)	950.0	1183.5
VP	0.309618	0.30888
GP	5.864407	5.59322
Fatigue Endurance Limit (με)	136	120
N_{f50}	10996583	10996583
AV (%)	4.7	4.8
Vb (%)	10.48	10.74
PNMS (%)	93	93
PPCS (%)	58.4	60
P200 (%)	5.9	5.9

* Stiffness is for a frequency of 10 Hz and 20 °C. Loading was performed at 0.5 Hz and various temperatures. Equations used units of MPa, but English units are presented for consistency.

The calculated RDEC fatigue endurance limit falls within the literature-defined range of 70-350 με. The RDEC model therefore appears to become useful in predicting the fatigue endurance limit for a wide range of mixtures with the limited amount of field data and inability to predict the fatigue endurance limit using field data.

Figure 36 presents the plateau value for each section plotted against the number of cycles to failure. All points fall within the normal strain regime. The plateau value of $6.74x10^{-9}$, corresponding to the fatigue endurance limit, is also displayed on this plot for reference. Figure 37 presents the RDEC and FWD-based tensile strains versus number of cycles to failure.

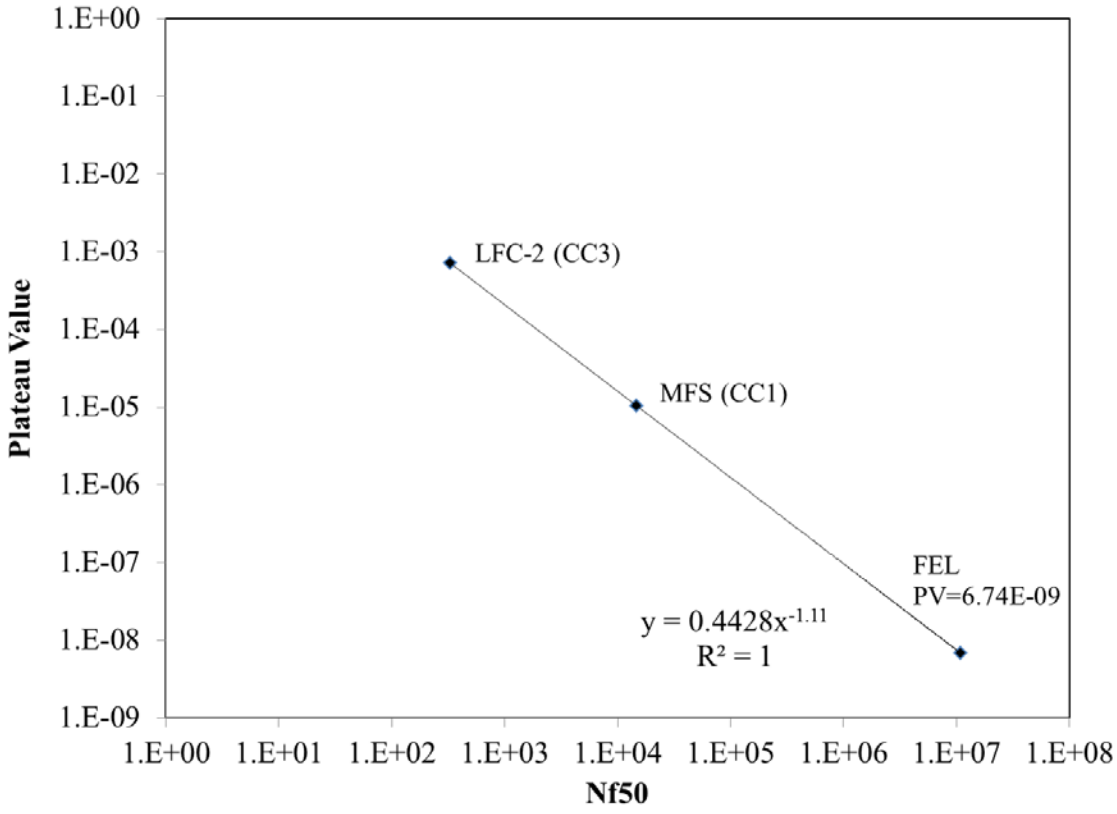

Figure 36: Plateau value versus number of cycles to failure

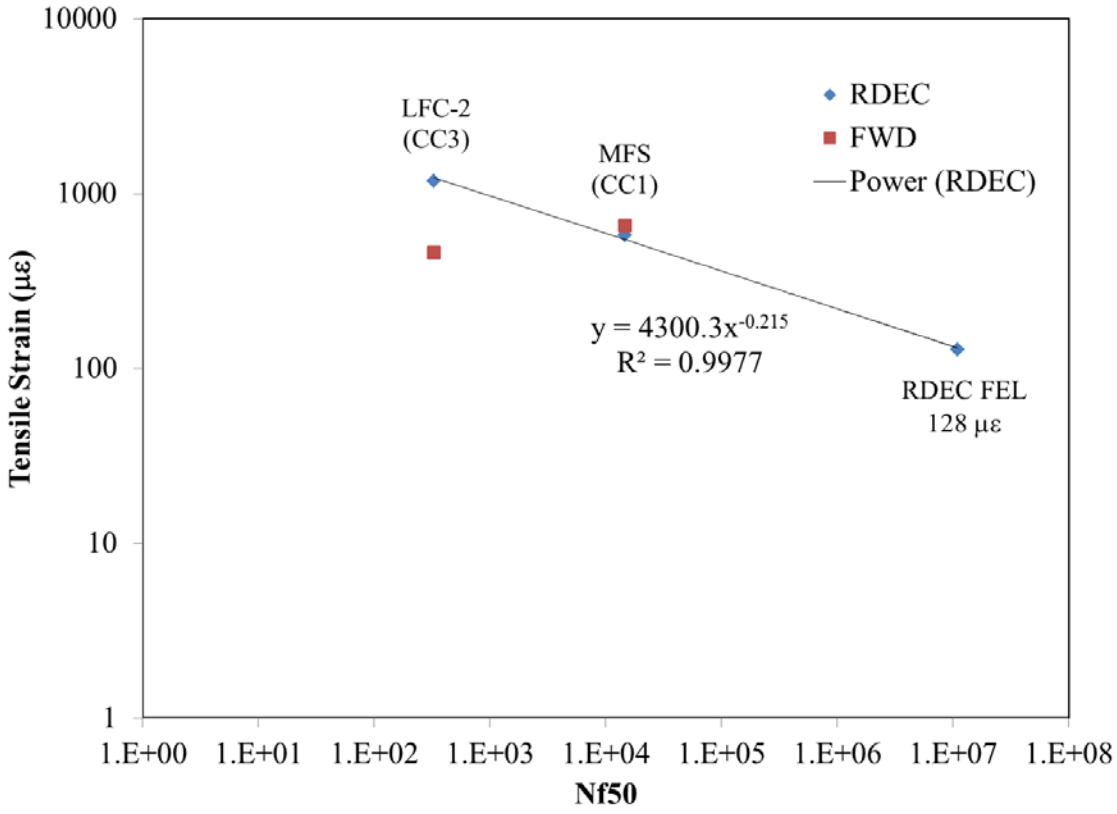

Figure 37: Tensile strain versus number of cycles to failure

As seen from Figure 36 and Figure 37, this thesis is concerned with normal strains only and not low strain levels below the fatigue endurance limit. While a true fatigue endurance limit cannot be estimated from field data, the fact that the field data results are close to the RDEC model results suggest that the RDEC method is viable for calculation of the fatigue endurance limit.

6.4 Summary of Findings

Table 32 presents a summary of the N_{f50} tensile strains estimated for all pavement sections using the FWD, variability, and RDEC approaches. As can be seen from this table, FWD results for section MFS showed that a 50% reduction in HMA modulus was reached during the application of loading passes. However, for the remaining CC1

sections the 50% reduction in the HMA layer modulus was not reached even after applying all the planned loading passes. These results indicate that these sections likely did not experience fatigue cracking, and either did not fail or failed in rutting or another failure mode.

The results presented in Table 32 for the MFS pavement section show that the N_{f50} tensile strains determined from FWD analysis and the RDEC model were 658 με and 580 με, respectively. In addition, it can be seen from this table that the N_{f50} tensile strain estimated using tensile strain variability was about 500 με. These results show that all three strain levels are relatively within 20 percent of one another. Table 32 also presents the results for the LFC pavement section. For this section, N_{f50} was not reached. The N_{f50} tensile strain estimated through the tensile strain variability approach for the LFC pavement section was about 450 με. This value was found to be comparable to that estimated using the RDEC model based on 35,463 cycles to failure (i.e., 424 με). This value was based on a 50 percent difference in the HMA modulus of the loaded test track and the unloaded centerline track, but this is not a true N_{f50}.

In the case of pavement sections constructed during CC3 (LFC-1 and LFC-2), the analysis of FWD data showed that both sections reached N_{f50}. However, the strain gages embedded in the LFC-1 pavement section had no good available strain data that could be used to determine the tensile strain at the N_{f50} loading pass. In the LFC-2 pavement section, the N_{f50} tensile strain was about 459 με, which is significantly lower than the theoretical value calculated using the RDEC model (i.e., 1186 με). The significant difference between these results is mainly attributed to the low N_{f50} values obtained from the FWD analysis. This low N_{f50} indicates that both CC3 pavement sections might have

failed due to failure modes other than fatigue cracking. In addition, the N_{f50} tensile strain estimated through the strain variability approach for the LFC-2 pavement section (i.e., 650 με) was higher than that estimated using the FWD approach.

Overall, the results presented in Table 32 show that the proposed FWD approach might be a viable method for determining the tensile strain at N_{f50} for asphalt pavements using full-scale accelerated pavement testing. It is important to note that this is the case as long as good strain sensor data is available and the number of cycles to failure is not very low. The fatigue endurance limit can then be calculated using the RDEC equations.

Table 32: Summary of findings table

Construction Cycle	Pavement Section	Subbase Thickness (in.)	N_{f50} Pass Number	50% Modulus reduction reached?	FWD Tensile Strain @ N_{f50} (με)	RDEC Theoretical N_{f50} Tensile Strain (με)	Average Strain Variability Limit (με)	Percent Difference between FWD and RDEC	RDEC Fatigue Endurance Limit (με)
One	**LFS**[1]	29.6	48,882[2]	No	--[4]	400	--[6]	-	-
One	**LFC**[1]	36.4	35,463[3]	No	--[4]	424	450[3]	-	-
One	**MFS**[1]	8.5	14,688	Yes	658	580	500	-11.8%	136
One	**MFC**[1]	12.1	15,758[2]	No	--[4]	555	--[6]	-	-
Three	**LFC-1**	16	329	Yes	--[5]	1186	--[5]	-	-
Three	**LFC-2**	24	329	Yes	459	1186	650	+158.3%	120

[1] North loading track only.
[2] Last recorded loading pass.
[3] Loading pass number based on approach where loaded lane modulus was compared to unloaded center lane modulus.
[4] N_{f50} was not reached.
[5] No valid strain data available for given loading pass.
[6] Variability only examined for sections that reached N_{f50}.

Chapter 7

Conclusions and Recommendations

7.1 Conclusions

A method for comparing the RDEC model approach for characterizing fatigue behavior of flexible airfield pavements to a proposed approach using field data was presented in this thesis. This proposed method was based on the concept that a reduction in HMA layer modulus of a pavement structure by 50 percent would indicate the fatigue failure. Falling weight deflectometer (FWD) testing results obtained for NAPTF Construction Cycle One (CC1), Construction Cycle Three (CC3), and Construction Cycle Five (CC5) flexible pavement sections were analyzed to determine at which loading pass each of these sections had a 50 percent reduction in their HMA layer modulus, i.e. to determine the value of N_{f50}. In addition, tensile strain data collected from strain gages embedded in each of these pavement sections were used to determine the N_{f50} tensile strain by averaging the peak tensile strain obtained from all sensors at the loading pass where N_{f50} occurred. To verify the proposed approach, comparisons between the N_{f50} tensile strain estimated using the proposed approach and those determined using the RDEC model were also conducted. The tensile strain at which the variability of the peak strain increases versus the number of loading passes was also used as a check for further verifying the proposed approach.

Based on the results of the analyses conducted, the following conclusions were made:

1) In the absence of performance data, such as crack maps and/or width and length of crack, the approach of determining number of passes to reach 50 percent reduction in

modulus from FWD data in conjunction with analysis of strain profile and its variability appears to be a viable method of determining the N_{f50} tensile strain in the field.

2) The N_{f50} tensile strains in the field estimated using the proposed approach were 658 με for section MFS of CC1 and 459 με for section LFC-2 of CC3. These values are higher than the fatigue endurance limit range of 70-350 με determined based on previous studies. This is due to the fact that field testing was done at normal strain levels where failure will occur, while lab testing to determine fatigue endurance limit occurred at low strains where failure will not realistically occur.
3) Analysis of FWD testing results showed that a 50% reduction in HMA layer modulus for the MFS pavement section was reached after 14,688 passes. The analysis of tensile strain data showed that, at this pass, the N_{f50} tensile strain for this section is approximately 658 με.
4) The FWD analysis showed that the LFC section reached N_{f50} after applying 35,463 loading passes; however, no valid strain data was available at that loading pass. Therefore, no N_{f50} tensile strain was determined for the LFC section. Furthermore, these results indicate that the MFS and LFC sections of CC1 might have experienced fatigue cracking.
5) Analysis of FWD testing results for the LFS and MFC sections showed that a 50% reduction in HMA layer modulus was not reached even after applying all of the planned passes (i.e., 48,882 for LFS and 15,758 for MFC). These results might indicate that fatigue cracking was not a major concern in either of these sections. These sections either did not fail or failed with a distress mode other than fatigue.

6) Sections LFC-2 SW and LFC-2 SE of CC5 appear to reach N_{f50} on June 27, 2012, when compared to FWD testing performed on May 31, 2012. Trafficking on LFC-2 did not begin until August 21, 2012. Therefore, the drop in modulus may be due to pre-trafficking tests performed on the section, since pre-trafficking tests are typically performed in a short period of time, and the HMA modulus was drastically reduced over a one-month period.
7) The peak strain data for CC1 pavement sections becomes variable around 400 to 500 με, which agrees with the results from using the RDEC equations; however for CC3 pavement, the peak strain data becomes variable around 650 με, which is lower than the theoretical N_{f50} tensile strain for CC3 obtained from RDEC model.
8) The N_{f50} tensile strain for the MFS section was comparable (within 12 percent) to the value estimated using the RDEC model. This shows that the RDEC model is a good predictor of the tensile strain value at N_{f50}. However, additional research might be needed to further verify the proposed approach because of the limited testing results.
9) The N_{f50} tensile strains estimated for section LFC-2 of CC3 are much higher than those in CC1. This is mainly attributed to the low number of loading passes after which 50% reduction in HMA modulus was reached for the LFC-2 section. There is a possibility that this section failed prematurely due to modes of failure other than fatigue cracking.
10) Overall, pavements with a thick subbase layer of at least 29 inches; such as LFS and LFC of CC1, LFC-3 and LFC-4 of CC3, and all CC5 sections, have performed better than pavements with a thin subbase layer. For example, LFC-1 and LFC-2 failed at only 329 loading passes and MFS failed at 14,688 loading passes, and while MFC did

not reach N_{f50}, it was only tested to about 15,000 loading passes. LFS and LFC with thicker subbase layers did not fail during the application of over 35,000 loading cycles.

7.2 Recommendations

Based on the analysis and the conclusions presented above, the following recommendations are suggested for future work on this study:

1) Out of 12 sections in CC1, CC3, and CC5 that were analyzed, N_{f50} tensile strains could be calculated for only two sections (MFS in CC1 and LFC-2 in CC3) using the proposed approach. Data was not available for many of the strain gages, and there was a large amount of "bad data" for CC1 and CC3 NAPTF data. Therefore, for future analysis, more pavement sections are needed to further determine if the RDEC approach is a viable method for calculating the fatigue endurance limit.
2) The proposed approach is limited due to lack of performance data, such as crack maps. The reduction in modulus could be due to other modes of failure such as rutting. Therefore, it is recommended to collect crack maps to be able to verify that cracking is occurring due to fatigue.
3) Pavement testing was done on standard HMA pavement. Testing on perpetual pavements is also recommended in order to determine the effectiveness of these pavements in improving fatigue life. The use of thicker HMA layers, for example, will cause fewer strain sensors to fail as they are placed further from the surface. This will cause better results, and will also provide data useful to evaluate the RDEC model's ability to predict fatigue behavior of perpetual-type pavements. Therefore,

this study should be performed on CC7, which includes perpetual pavement sections, when this construction cycle is completed.

4) Pavements with a thin subbase layer of less than 29 inches, such as sections LFC-1 and LFC-2 of CC3 and MFS and MFC of CC1, will fail faster in fatigue than sections with thick subbase layers of 29 inches or greater.
5) Relaxation and healing has an effect on fatigue behavior. Airport pavements typically experience longer rest periods than highway pavements. Tests should be performed with shorter and longer periods of rest between loading cycles to examine the effect of relaxation on airfield pavements in fatigue.

References

[1] B. Lane, A. W. Brown and S. Tighe, "Perpetual Pavements: The Ontario Experiment," in *International Conference on Perpetual Pavements*, Ohio, 2006.

[2] S. Carpenter, K. Ghuzlan and S. Shen, "Fatigue Endurance Limit for Highway and Airport Pavements," *Transportation Research Record 1832,* pp. 131-138, 2003.

[3] W. Van Dijk, "Practical Fatigue Characterization of Bituminous Mixes.," *Proceedings of the Association of Asphalt Paving Technologists (AAPT),* vol. 44, p. 38, 1975.

[4] W. Van Dijk and W. Visser, "The Energy Approach to Fatigue for Pavement Design," *Proceedings of the Association of Asphalt Paving Technologists (AAPT),* vol. 46, pp. 1-40, 1977.

[5] G. Chomton and P. J. Valayer, "Applied Rheology of Asphalt Mixes Practical Application," in *Proceedings of Third International Conference on the Structural Design of Asphalt Pavements*, London, 1972.

[6] S. Shen and S. Carpenter, "Dissipated Energy Concepts for HMA Performance: Fatigue and Healing," Technical Report of Research Supported by the Cooperative Agreement DOT 05-C-AT-UIUC-COE, 2007.

[7] D. Brill, *Personal communication,* 2014.

[8] P. S. Pell, "Fatigue of Asphalt Pavement Mixes," *Proceedings of the Second International Conference on the Structural Design of Asphalt Pavements, Ann Arbor, Mich.*, pp. 577-594, 1967.

[9] C. L. Monismith, J. A. Epps and F. N. Finn, "Improved Asphalt Mix Design," *Journal of AAPT,* vol. 55, pp. 347-406, 1985.

[10] Y. R. Kim, D. N. Little and F. Benson, "Chemical and Mechanical Evaluation on Healing Mechanism on Asphalt Concrete," *Journal of the Association of Asphalt Paving Technologists (AAPT),* vol. 59, pp. 240-276, 1990.

[11] Y. R. Kim, H. J. Lee and D. N. Little, "Fatigue Characterization of Asphalt Concrete Using Viscoelasticity and Continuum Damage Theory," *Journal of the Association of Asphalt Paving Technologists (AAPT),* vol. 66, pp. 520-569, 1997.

[12] Y. R. Kim, H. J. Lee and D. N. Little, "Fundamental Properties of Asphalts and Modified Asphalts," Texas A&M University, 1998.

[13] R. A. Schapery, "Correspondence Principles and a Generalized J Integral for Large Deformation and Fracture Analysis of Viscoelastic Media," *International Journal of Fracture,* vol. 25, 1984.

[14] D. Roylance, "Engineering Viscoelasticity," Massachusetts Institute of Technology, Cambridge, Mass., 2001.

[15] S. W. Park, Y. R. Kim and et al., "A Viscoelastic Continuum Damage Model and Its Application to Uniaxial Behavior of Asphalt Concrete," *Mechanics of Materials,* vol. 24, no. 4, pp. 241-255, 1996.

[16] H. J. Lee, "Uniaxial Constitutive Modeling of Asphalt Concrete Using Viscoelasticity and Continuum Damage Theory," North Carolina State University, Raleigh, N.C., 1996.

[17] R. A. Schapery, "On the Mechanics of Crack Healing," *International Journal of Fracture,* 1988.

[18] R. L. Lytton and et al., "Development and Validation of Performance Prediction Model and Specifications for Asphalt Binders and Paving Mixes," The Strategic Highway Research Program Report SHRP-A-357, 1993.

[19] C. W. Chen, "Mechanistic Approach to the Evaluation of Microdamage in Asphalt Mixes," Texas A&M University, 1997.

[20] D. A. Anderson, Y. M. LeHir, M. O. Marasteanu, J. P. Planche and D. Martin, "Evaluation of fatigue criteria for asphalt binders," *Transportation Research Record,* vol. 1766, pp. 48-56, 2001.

[21] J. P. Planche, D. A. Anderson, G. Gauthier, M. Hir and D. Martin, "Evaluation of Fatigue Properties of Bituminous Binders," *Materials and Construction,* vol. 37, no. June 2004, pp. 356-359, 2004.

[22] K. A. Ghuzlan and S. H. Carpenter, "An Energy-Derived/Damage-Based Failure Criteria for Fatigue Testing," *Transportation Research Record: Journal of the Transportation Research Board,* vol. 1723, pp. 131-141, 2000.

[23] Y. Mehta, "Development of the Rate of Dissipated Energy Change (RDEC) Based Fatigue Model Calibrated Using Mechanical Response Data and Field Performance from CC1 and CC3 Test Items at the National Airport Pavement Test Facility," Rowan University, Glassboro, N.J., 2013.

[24] Y. Mehta and R. Roque, "Evaluation of FWD Data for Determination of Layer Moduli of Pavements".

[25] "Pavement Testing: Falling Weight Deflectograph," Testconsult Ltd., [Online]. Available: http://www.testconsult.co.uk/itemdetail.aspx?dept=pavement-testing&id=31. [Accessed 29 July 2014].

[26] Federal Aviation Administration, "National Airport Pavement Testing Facility," 2013. [Online]. [Accessed 26 August 2013].

[27] Federal Aviation Administration, "Part 5, Flexible Surface Courses, of AC 150/5370-10F," Washington, D.C., 2011.

[28] Federal Aviation Administration, "Part 3, Item P-209 Crushed Aggregate Base Course, of AC 150/5370-10F," Washington, D.C., 2011.

[29] Federal Aviation Administration, "Part 2, Item P-154 Subbase Course, of AC 150/5370-10F," Washington, D.C., 2011.

[30] E. J. Yoder and M. Witczak, "Principles of Pavement Design," Hoboken, N.J., John Wiley and Sons, Inc., 1975, p. 284.

Appendix A

Querying the NAPTF Website and Database

A.1 Querying the NAPTF Website

In order to determine the strain behavior of CC1 test pavement, data was retrieved from the NAPTF website. When visiting the website, which can be found at http://www.airporttech.tc.faa.gov/naptf/cc1.asp, click on the "Query" button at the bottom center of the page, then click on the "Dynamic Sensor Data" link, and then in the "Query Dynamic Data" dialog box, select "Asphalt Strain" for Sensor Type, "LFS-1" for Test Item, and the date in question, beginning with February 14, 2000. To get specific pass numbers, one can use Structured Query Language (SQL) in the "SQL Query Dynamic Data" dialog box below. For example, to get data for strain gage LBS5 passes 3101 to 3200, enter the following SQL command:

Select * from dynamic_data where sensorid in (select sensorid from spus where sensorname in ('LBS5')) and eventno >3100 and eventno <3201

In order to extract the Track 0 data from this information, go to "Traffic Data" under "Query", and then select the date(s) in question. The column "TrackNo" tells you the wander position of the test vehicle for the given pass. When the number is equal to zero, record the "EventNo" and include only these passes in the analysis.

To obtain the time-strain data for a given event, when looking in the query search results, go to the far right column and click the "Download" link. It will give a comma-separated list, where the first value is the number of readings, the second value is the time interval in seconds between readings, and the remaining numbers are the readings in millistrains.

A.2 Querying the NAPTF Database

In order to obtain the strain behavior of CC3 test pavement, a database provided by FAA personnel was used to obtain strain data. This database requires the use of Microsoft SQL Server to extract the data that is within the database. To obtain strain data for a given loading pass or group of passes, the Sensor ID for the strain sensors in question must be known, along with the track number in question (Track 0 for this thesis). An example of an SQL query for CC3 is given as follows, where the Track 0 data for sensor ASG-36, which has a Sensor ID of 138, is given as follows:

```
SELECT *
FROM dbo.dynamic_data
JOIN dbo.Traffic ON dbo.Traffic.EventNo = dbo.dynamic_data.EventNo
WHERE SensorID =138 AND TrackNo =0
```

This query will retrieve all Track 0 strain data from sensor ASG-36. To obtain the time-strain data for a given event, when looking in the query search results, look for a column titled “Sensor Record.” It will give a comma-separated list, where the first value is the number of readings, the second value is the time interval in seconds between readings, and the remaining numbers are the readings in millistrains.

Appendix B

Material Properties and Gradations

Table B-1: P-401 Field Core Density Testing for LFS [26]

Item	Material	Date	Lift No.	Spec. ID	Station	CL Offset, ft.	Thickness, in.	Gmm	Gmb (field)	Gmb (lab)	% Compaction	Air Voids, %
LFS	P-401 Base	2/19/1999	1	M-1			2.25	2.591	2.488	2.516	98.9	4.0
LFS	P-401 Base	2/19/1999	1	M-2			2.19	2.591	2.463	2.516	97.9	4.9
LFS	P-401 Base	2/19/1999	1	M-3			2.25	2.591	2.422	2.516	96.3	6.5
LFS	P-401 Base	2/19/1999	1	M-4			2.25	2.591	2.450	2.516	97.4	5.4
LFS	P-401 Base	2/19/1999	1	J-1			2.19	2.591	2.438	2.516	96.9	5.9
LFS	P-401 Base	2/19/1999	1	J-2			2.25	2.591	2.444	2.516	97.1	5.7
LFS	P-401 Base	2/19/1999	1	J-3			2.25	2.591	2.410	2.516	95.8	7.0
LFS	P-401 Base	2/19/1999	1	J-4			2.00	2.591	2.412	2.516	95.9	6.9
LFS	P-401 Base	3/5/1999	2	M-1	1+44	8R	2.75	2.582	2.505	2.510	99.8	3.0
LFS	P-401 Base	3/5/1999	2	M-2	1+97	18L	2.94	2.582	2.518	2.510	100.3	2.5
LFS	P-401 Base	3/5/1999	2	M-3	1+92	7R	2.50	2.582	2.504	2.510	99.8	3.0
LFS	P-401 Base	3/5/1999	2	M-4	1+55	25L	2.63	2.582	2.499	2.510	99.6	3.2
LFS	P-401 Base	3/5/1999	2	J-1	1+62	22L	2.63	2.582	2.493	2.510	99.3	3.4
LFS	P-401 Base	3/5/1999	2	J-2	1+94	9L	2.63	2.582	2.506	2.510	99.8	2.9
LFS	P-401 Base	3/5/1999	2	J-3	1+61	4R	2.25	2.582	2.484	2.510	99.0	3.8
LFS	P-401 Base	3/5/1999	2	J-4	1+80	19R	2.63	2.582	2.498	2.510	99.5	3.3
LFS	P-401 Surface	3/17/1999	1	M-1			2.38	2.580	2.487	2.512	99.0	3.6
LFS	P-401 Surface	3/17/1999	1	M-2			2.75	2.580	2.507	2.512	99.8	2.8
LFS	P-401 Surface	3/17/1999	1	M-3			2.38	2.580	2.498	2.512	99.4	3.2
LFS	P-401 Surface	3/17/1999	1	M-4			2.50	2.580	2.496	2.512	99.4	3.3
LFS	P-401 Surface	3/17/1999	1	J-1			2.38	2.580	2.375	2.512	94.5	7.9
LFS	P-401 Surface	3/17/1999	1	J-2			2.56	2.580	2.478	2.512	98.6	4.0
LFS	P-401 Surface	3/17/1999	1	J-3			2.63	2.580	2.404	2.512	95.7	6.8
LFS	P-401 Surface	3/17/1999	1	J-4			2.88	2.580	2.415	2.512	96.1	6.4
LFS	P-401 Surface	3/19/1999	2	M-1			2.44	2.586	2.504	2.518	99.4	3.2
LFS	P-401 Surface	3/19/1999	2	M-2			2.50	2.586	2.514	2.518	99.8	2.8
LFS	P-401 Surface	3/19/1999	2	M-3			2.69	2.586	2.509	2.518	99.6	3.0
LFS	P-401 Surface	3/19/1999	2	M-4			2.50	2.586	2.498	2.518	99.2	3.4
LFS	P-401 Surface	3/19/1999	2	J-1			2.63	2.586	2.454	2.518	97.5	5.1
LFS	P-401 Surface	3/19/1999	2	J-2			2.50	2.586	2.405	2.518	95.5	7.0
LFS	P-401 Surface	3/19/1999	2	J-3			2.63	2.586	2.377	2.518	94.4	8.1
LFS	P-401 Surface	3/19/1999	2	J-4			2.75	2.586	2.423	2.518	96.2	6.3

Table B-2: P-401 Field Core Density Testing for LFC [26]

Item	Material	Date	Lift No.	Spec. ID	Station	CL Offset, ft.	Thickness, in.	Gmm	Gmb (field)	Gmb (lab)	% Compaction	Air Voids, %
LFC	P-401 Surface	3/17/1999	1	M-1			2.38	2.580	2.487	2.512	99.0	3.6
LFC	P-401 Surface	3/17/1999	1	M-2			2.75	2.580	2.507	2.512	99.8	2.8
LFC	P-401 Surface	3/17/1999	1	M-3			2.38	2.580	2.498	2.512	99.4	3.2
LFC	P-401 Surface	3/17/1999	1	M-4			2.50	2.580	2.496	2.512	99.4	3.3
LFC	P-401 Surface	3/17/1999	1	J-1			2.38	2.580	2.375	2.512	94.5	7.9
LFC	P-401 Surface	3/17/1999	1	J-2			2.56	2.580	2.478	2.512	98.6	4.0
LFC	P-401 Surface	3/17/1999	1	J-3			2.63	2.580	2.404	2.512	95.7	6.8
LFC	P-401 Surface	3/17/1999	1	J-4			2.88	2.580	2.415	2.512	96.1	6.4
LFC	P-401 Surface	3/19/1999	2	M-1			2.44	2.586	2.504	2.518	99.4	3.2
LFC	P-401 Surface	3/19/1999	2	M-2			2.50	2.586	2.514	2.518	99.8	2.8
LFC	P-401 Surface	3/19/1999	2	M-3			2.69	2.586	2.509	2.518	99.6	3.0
LFC	P-401 Surface	3/19/1999	2	M-4			2.50	2.586	2.498	2.518	99.2	3.4
LFC	P-401 Surface	3/19/1999	2	J-1			2.63	2.586	2.454	2.518	97.5	5.1
LFC	P-401 Surface	3/19/1999	2	J-2			2.50	2.586	2.405	2.518	95.5	7.0
LFC	P-401 Surface	3/19/1999	2	J-3			2.63	2.586	2.377	2.518	94.4	8.1
LFC	P-401 Surface	3/19/1999	2	J-4			2.75	2.586	2.423	2.518	96.2	6.3

Table B-3: P-401 Field Core Density Testing for MFC [26]

Item	Material	Date	Lift No.	Spec. ID	Station	CL Offset, ft.	Thickness, cm	Gmm	Gmb (field)	Gmb (lab)	% Compaction	Air Voids, %
MFC	P-401 Surface	3/17/1999	1	M-1			3.13	2.580	2.497	2.512	99.4	3.2
MFC	P-401 Surface	3/17/1999	1	M-2			2.44	2.580	2.482	2.512	98.8	3.8
MFC	P-401 Surface	3/17/1999	1	M-3			2.25	2.580	2.483	2.512	98.8	3.8
MFC	P-401 Surface	3/17/1999	1	M-4			2.63	2.580	2.477	2.512	98.6	4.0
MFC	P-401 Surface	3/17/1999	1	J-1			2.75	2.580	2.388	2.512	95.1	7.4
MFC	P-401 Surface	3/17/1999	1	J-2			2.75	2.580	2.373	2.512	94.5	8.0
MFC	P-401 Surface	3/17/1999	1	J-3			2.50	2.580	2.439	2.512	97.1	5.5
MFC	P-401 Surface	3/17/1999	1	J-4			2.38	2.580	2.446	2.512	97.4	5.2
MFC	P-401 Surface	3/19/1999	2	M-1			2.75	2.586	2.498	2.518	99.2	3.4
MFC	P-401 Surface	3/19/1999	2	M-2			2.75	2.586	2.471	2.518	98.1	4.4
MFC	P-401 Surface	3/19/1999	2	M-3			2.44	2.586	2.487	2.518	98.8	3.8
MFC	P-401 Surface	3/19/1999	2	M-4			2.50	2.586	2.485	2.518	98.7	3.9
MFC	P-401 Surface	3/19/1999	2	J-1			2.69	2.586	2.359	2.518	93.7	8.8
MFC	P-401 Surface	3/19/1999	2	J-2			2.75	2.586	2.360	2.518	93.7	8.7
MFC	P-401 Surface	3/19/1999	2	J-3			2.38	2.586	2.466	2.518	97.9	4.6
MFC	P-401 Surface	3/19/1999	2	J-4			2.56	2.586	2.376	2.518	94.4	8.1

Table B-4: P-401 Field Core Density Testing for MFS [26]

Item	Material	Date	Lift No.	Spec. ID	Station	CL Offset, ft.	Thickness, cm	Gmm	Gmb (field)	Gmb (lab)	% Compaction	Air Voids, %
MFS	P-401 Base	3/5/1999	1	M-1	4+32	9R		2.589	2.480	2.521	98.4	4.2
MFS	P-401 Base	3/5/1999	1	M-2	4+60	22R		2.589	2.486	2.521	98.6	4.0
MFS	P-401 Base	3/5/1999	1	M-3	4+50	11L		2.589	2.486	2.521	98.6	4.0
MFS	P-401 Base	3/5/1999	1	M-4	4+14	2L		2.589	2.478	2.521	98.3	4.3
MFS	P-401 Base	3/5/1999	1	J-1	4+20	20R		2.589	2.474	2.521	98.1	4.4
MFS	P-401 Base	3/5/1999	1	J-2	4+56	6R		2.589	2.458	2.521	97.5	5.1
MFS	P-401 Base	3/5/1999	1	J-3	4+38	21L		2.589	2.468	2.521	97.9	4.7
MFS	P-401 Base	3/5/1999	1	J-4	4+25	6L		2.589	2.482	2.521	98.5	4.1
MFS	P-401 Base	3/10/1999	2	M-1	4+74	1.3R	2.13	2.573	2.506	2.527	99.2	2.6
MFS	P-401 Base	3/10/1999	2	M-2	4+19	16.4R	1.94	2.573	2.460	2.527	97.3	4.4
MFS	P-401 Base	3/10/1999	2	M-3	4+56	19.2L	1.94	2.573	2.491	2.527	98.6	3.2
MFS	P-401 Base	3/10/1999	2	M-4	4+36	22.5L	2.25	2.573	2.474	2.527	97.9	3.8
MFS	P-401 Base	3/10/1999	2	J-1	4+68		2.13	2.573	2.463	2.527	97.5	4.3
MFS	P-401 Base	3/10/1999	2	J-2	4+59		2.50	2.573	2.482	2.527	98.2	3.5
MFS	P-401 Base	3/10/1999	2	J-3	4+24		2.13	2.573	2.484	2.527	98.3	3.5
MFS	P-401 Base	3/10/1999	2	J-4	4+46		2.13	2.573	2.480	2.527	98.1	3.6
MFS	P-401 Surface	3/17/1999	1	M-1			3.13	2.580	2.497	2.512	99.4	3.2
MFS	P-401 Surface	3/17/1999	1	M-2			2.44	2.580	2.482	2.512	98.8	3.8
MFS	P-401 Surface	3/17/1999	1	M-3			2.25	2.580	2.483	2.512	98.8	3.8
MFS	P-401 Surface	3/17/1999	1	M-4			2.63	2.580	2.477	2.512	98.6	4.0
MFS	P-401 Surface	3/17/1999	1	J-1			2.75	2.580	2.388	2.512	95.1	7.4
MFS	P-401 Surface	3/17/1999	1	J-2			2.75	2.580	2.373	2.512	94.5	8.0
MFS	P-401 Surface	3/17/1999	1	J-3			2.50	2.580	2.439	2.512	97.1	5.5
MFS	P-401 Surface	3/17/1999	1	J-4			2.38	2.580	2.446	2.512	97.4	5.2
MFS	P-401 Surface	3/19/1999	2	M-1			2.75	2.586	2.498	2.518	99.2	3.4
MFS	P-401 Surface	3/19/1999	2	M-2			2.75	2.586	2.471	2.518	98.1	4.4
MFS	P-401 Surface	3/19/1999	2	M-3			2.44	2.586	2.487	2.518	98.8	3.8
MFS	P-401 Surface	3/19/1999	2	M-4			2.50	2.586	2.485	2.518	98.7	3.9
MFS	P-401 Surface	3/19/1999	2	J-1			2.69	2.586	2.359	2.518	93.7	8.8
MFS	P-401 Surface	3/19/1999	2	J-2			2.75	2.586	2.360	2.518	93.7	8.7
MFS	P-401 Surface	3/19/1999	2	J-3			2.38	2.586	2.466	2.518	97.9	4.6
MFS	P-401 Surface	3/19/1999	2	J-4			2.56	2.586	2.376	2.518	94.4	8.1

Table B-5: Mix Properties and Gradation for LFS [26]

Item	Material	Date	Lift No.	Thickness, in.	Sample No.	% Pass 3/4"	% Pass 1/2"	% Pass 3/8"	% Pass #4	% Pass #8	% Pass #16	% Pass #30	% Pass #50	% Pass #100	% Pass # 200	% Asphalt
LFS	P-401 Base	2/19/1999	1	2.5	1	100.00	96.30	88.80	60.30	41.60	29.40	20.20	13.20	9.20	6.60	5.54
LFS	P-401 Base	2/19/1999	1	2.5	2	98.30	91.70	86.50	57.30	41.60	29.90	20.20	13.00	8.60	5.80	5.33
LFS	P-401 Base	2/19/1999	1	2.5	3	100.00	95.50	89.20	60.20	43.30	30.80	21.10	13.40	8.90	6.10	5.55
LFS	P-401 Base	2/19/1999	1	2.5	4	99.30	94.20	88.40	56.30	40.70	29.10	20.00	12.50	8.20	5.60	5.26
LFS	P-401 Base	3/5/1999	2	2.5	1	100.00	93.70	87.20	59.10	41.00	28.90	20.00	12.80	8.90	6.20	5.44
LFS	P-401 Base	3/5/1999	2	2.5	2	100.00	90.80	86.30	58.60	40.20	28.30	19.50	12.50	8.50	6.00	5.40
LFS	P-401 Base	3/5/1999	2	2.5	3	100.00	91.00	86.60	59.70	41.00	28.70	19.70	12.60	8.60	5.80	5.44
LFS	P-401 Surface	3/17/1999	1	2.5	1	100.00	92.40	88.70	61.60	42.80	30.00	20.40	12.80	8.60	5.80	5.59
LFS	P-401 Surface	3/17/1999	1	2.5	2	100.00	91.30	84.90	56.10	39.40	28.00	19.10	12.00	8.10	5.70	5.14
LFS	P-401 Surface	3/17/1999	1	2.5	3	100.00	91.10	88.00	60.10	42.50	29.70	20.30	12.80	8.60	6.00	5.32
LFS	P-401 Surface	3/17/1999	1	2.5	4	100.00	92.80	86.60	59.90	42.20	29.80	20.30	12.70	8.50	5.90	5.34
LFS	P-401 Surface	3/17/1999	1	2.5	5	100.00	89.70	86.90	60.10	41.80	29.60	20.00	12.40	8.10	5.60	5.37
LFS	P-401 Surface	3/19/1999	2	2.5	1	100.00	97.10	92.40	63.90	44.70	30.80	20.80	13.20	8.90	6.30	5.55
LFS	P-401 Surface	3/19/1999	2	2.5	2	100.00	95.90	90.20	59.40	41.20	29.00	19.90	14.70	8.70	6.00	5.30
LFS	P-401 Surface	3/19/1999	2	2.5	3	100.00	92.60	85.40	57.30	40.60	28.50	19.70	12.60	8.50	5.90	5.22
LFS	P-401 Surface	3/19/1999	2	2.5	4	100.00	96.00	88.70	61.40	42.80	29.50	20.10	12.90	8.70	6.00	5.42
LFS	P-401 Surface	3/19/1999	2	2.5	5	100.00	91.50	85.70	59.60	42.40	29.70	20.30	13.10	8.80	6.00	5.49

Table B-6: Mix Properties and Gradation for LFC [26]

Item	Material	Date	Lift No.	Thickness, in.	Sample No.	% Pass 3/4"	% Pass 1/2"	% Pass 3/8"	% Pass #4	% Pass #8	% Pass #16	% Pass #30	% Pass #50	% Pass #100	% Pass # 200	% Asphalt
LFC	P-401 Surface	3/17/1999	1	2.5	1	100.00	92.40	88.70	61.60	42.80	30.00	20.40	12.80	8.60	5.80	5.59
LFC	P-401 Surface	3/17/1999	1	2.5	2	100.00	91.30	84.90	56.10	39.40	28.00	19.10	12.00	8.10	5.70	5.14
LFC	P-401 Surface	3/17/1999	1	2.5	3	100.00	91.10	88.00	60.10	42.50	29.70	20.30	12.80	8.60	6.00	5.32
LFC	P-401 Surface	3/17/1999	1	2.5	4	100.00	92.80	86.60	59.90	42.20	29.80	20.30	12.70	8.50	5.90	5.34
LFC	P-401 Surface	3/17/1999	1	2.5	5	100.00	89.70	86.90	60.10	41.80	29.60	20.00	12.40	8.10	5.60	5.37
LFC	P-401 Surface	3/19/1999	2	2.5	1	100.00	97.10	92.40	63.90	44.70	30.80	20.80	13.20	8.90	6.30	5.55
LFC	P-401 Surface	3/19/1999	2	2.5	2	100.00	95.90	90.20	59.40	41.20	29.00	19.90	14.70	8.70	6.00	5.30
LFC	P-401 Surface	3/19/1999	2	2.5	3	100.00	92.60	85.40	57.30	40.60	28.50	19.70	12.60	8.50	5.90	5.22
LFC	P-401 Surface	3/19/1999	2	2.5	4	100.00	96.00	88.70	61.40	42.80	29.50	20.10	12.90	8.70	6.00	5.42
LFC	P-401 Surface	3/19/1999	2	2.5	5	100.00	91.50	85.70	59.60	42.40	29.70	20.30	13.10	8.80	6.00	5.49

Table B-7: Mix Properties and Gradation for MFC [26]

Item	Material	Date	Lift No.	Thickness, in.	Sample No.	% Pass 3/4"	% Pass 1/2"	% Pass 3/8"	% Pass #4	% Pass #8	% Pass #16	% Pass #30	% Pass #50	% Pass #100	% Pass # 200	% Asphalt
MFC	P-401 Surface	3/17/1999	1	2.5	1	100.00	92.40	88.70	61.60	42.80	30.00	20.40	12.80	8.60	5.80	5.59
MFC	P-401 Surface	3/17/1999	1	2.5	2	100.00	91.30	84.90	56.10	39.40	28.00	19.10	12.00	8.10	5.70	5.14
MFC	P-401 Surface	3/17/1999	1	2.5	3	100.00	91.10	88.00	60.10	42.50	29.70	20.30	12.80	8.60	6.00	5.32
MFC	P-401 Surface	3/17/1999	1	2.5	4	100.00	92.80	86.60	59.90	42.20	29.80	20.30	12.70	8.50	5.90	5.34
MFC	P-401 Surface	3/17/1999	1	2.5	5	100.00	89.70	86.90	60.10	41.80	29.60	20.00	12.40	8.10	5.60	5.37
MFC	P-401 Surface	3/19/1999	2	2.5	1	100.00	97.10	92.40	63.90	44.70	30.80	20.80	13.20	8.90	6.30	5.55
MFC	P-401 Surface	3/19/1999	2	2.5	2	100.00	95.90	90.20	59.40	41.20	29.00	19.90	14.70	8.70	6.00	5.30
MFC	P-401 Surface	3/19/1999	2	2.5	3	100.00	92.60	85.40	57.30	40.60	28.50	19.70	12.60	8.50	5.90	5.22
MFC	P-401 Surface	3/19/1999	2	2.5	4	100.00	96.00	88.70	61.40	42.80	29.50	20.10	12.90	8.70	6.00	5.42
MFC	P-401 Surface	3/19/1999	2	2.5	5	100.00	91.50	85.70	59.60	42.40	29.70	20.30	13.10	8.80	6.00	5.49

Table B-8: Mix Properties and Gradation for MFS [26]

Item	Material	Date	Lift No.	Thickness, in.	Sample No.	% Pass 3/4"	% Pass 1/2"	% Pass 3/8"	% Pass #4	% Pass #8	% Pass #16	% Pass #30	% Pass #50	% Pass #100	% Pass # 200	% Asphalt
MFS	P-401 Base	3/5/1999	1	2.5	1	100.00	92.50	85.70	56.40	39.10	28.20	19.60	12.50	8.50	5.80	5.24
MFS	P-401 Base	3/5/1999	1	2.5	2	100.00	90.80	85.70	57.20	39.70	27.90	19.30	12.50	8.60	5.90	5.28
MFS	P-401 Base	3/5/1999	1	2.5	3	100.00	98.80	83.70	55.40	38.80	27.80	19.30	12.20	8.30	5.90	5.22
MFS	P-401 Base	3/10/1999	2	2.4	1	100.00	93.70	87.10	59.20	42.30	30.10	20.70	13.20	9.00	6.40	5.72
MFS	P-401 Base	3/10/1999	2	2.4	2	100.00	90.50	85.00	55.30	38.90	27.60	19.00	12.20	8.30	5.80	5.37
MFS	P-401 Base	3/10/1999	2	2.4	3	100.00	91.00	82.70	51.30	35.50	26.10	18.60	12.00	8.20	5.70	5.20
MFS	P-401 Surface	3/17/1999	1	2.5	1	100.00	92.40	88.70	61.60	42.80	30.00	20.40	12.80	8.60	5.80	5.59
MFS	P-401 Surface	3/17/1999	1	2.5	2	100.00	91.30	84.90	56.10	39.40	28.00	19.10	12.00	8.10	5.70	5.14
MFS	P-401 Surface	3/17/1999	1	2.5	3	100.00	91.10	88.00	60.10	42.50	29.70	20.30	12.80	8.60	6.00	5.32
MFS	P-401 Surface	3/17/1999	1	2.5	4	100.00	92.80	86.60	59.90	42.20	29.80	20.30	12.70	8.50	5.90	5.34
MFS	P-401 Surface	3/17/1999	1	2.5	5	100.00	89.70	86.90	60.10	41.80	29.60	20.00	12.40	8.10	5.60	5.37
MFS	P-401 Surface	3/19/1999	2	2.5	1	100.00	97.10	92.40	63.90	44.70	30.80	20.80	13.20	8.90	6.30	5.55
MFS	P-401 Surface	3/19/1999	2	2.5	2	100.00	95.90	90.20	59.40	41.20	29.00	19.90	14.70	8.70	6.00	5.30
MFS	P-401 Surface	3/19/1999	2	2.5	3	100.00	92.60	85.40	57.30	40.60	28.50	19.70	12.60	8.50	5.90	5.22
MFS	P-401 Surface	3/19/1999	2	2.5	4	100.00	96.00	88.70	61.40	42.80	29.50	20.10	12.90	8.70	6.00	5.42
MFS	P-401 Surface	3/19/1999	2	2.5	5	100.00	91.50	85.70	59.60	42.40	29.70	20.30	13.10	8.80	6.00	5.49

Appendix C

Data Cleaning and Filtering

As mentioned in Chapter 3, twelve strain gages were placed in each of the CC1 pavement sections for measuring the tensile strains upon loading. Table , Table , and Table present the availability and type of data (i.e. good or bad) that can be obtained from sensors placed in flexible pavement sections constructed during CC1 for low-strength, medium-strength, and high-strength subgrade sensors, respectively. As can be seen from these tables, data obtained from the sensors was classified into four different categories. These categories include (1) Data Available and Good, (2) Not All Data Available, (3) Data Available but Bad, and (4) No Data Available. Availability of the data for a particular CC1 sensor was determined through going on to the NAPTF website (http://www.airporttech.tc.faa.gov/naptf/cc1.asp) and querying the CC1 database, as outlined in Appendix A. CC3 data availability was determined through the use of the database provided by the FAA. The quality of the data for a particular sensor was determined through plotting the strain values obtained from that sensor versus the time at a specific loading pass. Peak strains were also plotted versus loading passes as an additional check.

Figure C-1 and Figure C-2 present good and bad data, respectively, obtained from plotting strain versus time for each sensor at loading pass number 3087. As can be seen from Figure C-1, good sensor data has one, two, or three strain peaks/valleys whereas for the bad data, shown in Figure C-2, no strain peaks/valleys were identified. Additional filtering was done by plotting the peak strain profiles for passes along Track 0 of the

wander pattern and determining if the sensor failed during loading. For example, sensor LBS8 failed after about 11000 loading cycles, which can be seen in Figure C-3, as the recorded strain gage values dropped to near zero. The same cleaning and filtering procedure was applied for all sensors placed in CC1 flexible pavement sections.

Table C-4 presents the availability and quality of CC3 data for each strain gage sensor. All sensors in LFC-1 and LFC-2 (i.e. up to sensor ASG-18) are classified as bad due to the limited data available for these passes. Table C-5 presents the availability and quality of CC5 data for each strain gage sensor.

Table C-1: Availability and Type of Data for Low-Strength Subgrade Sensors

Sensor	Good/ Bad	Sensor	Good/ Bad	Sensor	Good/ Bad
LBS1	Good	LSS1	N/A	LSC1	Bad
LBS2	N/A	LSS2	N/A	LSC2	Bad
LBS3	Good	LSS3	Bad	LSC3	Good
LBS4	Good	LSS4	N/A	LSC4	N/A
LBS5	Bad	LSS5	N/A	LSC5	Bad
LBS6	Good	LSS6	N/A	LSC6	Bad
LBS7	Good	LSS7	N/A	LSC7	N/A
LBS8	Bad	LSS8	N/A	LSC8	Bad
LBS9	Bad	LSS9	Good	LSC9	N/A
LBS10	Good	LSS10	N/A	LSC10	N/A
LBS11	Good	LSS11	Good*	LSC11	Bad
LBS12	N/A	LSS12	N/A	LSC12	Bad

*Not all data available.

Table C-2: Availability and Type of Data for Medium-Strength Subgrade Sensors

Sensor	Good/ Bad	Sensor	Good/ Bad	Sensor	Good/ Bad
MBS1	Good	MSS1	N/A	MSC1	N/A
MBS2	Good	MSS2	N/A	MSC2	Good
MBS3	Good	MSS3	N/A	MSC3	Bad
MBS4	Good	MSS4	N/A	MSC4	Bad
MBS5	Bad	MSS5	N/A	MSC5	Bad
MBS6	Bad	MSS6	Good	MSC6	Bad
MBS7	Good	MSS7	Good	MSC7	Bad
MBS8	Good	MSS8	Good	MSC8	Bad
MBS9	Bad	MSS9	N/A	MSC9	Bad
MBS10	Good	MSS10	N/A	MSC10	Good
MBS11	Bad	MSS11	N/A	MSC11	Bad
MBS12	Good	MSS12	N/A	MSC12	Good

Table C-3: Availability and Type of Data for High-Strength Subgrade Sensors

Sensor	Good/ Bad	Sensor	Good/ Bad	Sensor	Good/ Bad
HBS1	Good	HSS1	N/A	HSC1	N/A
HBS2	Good	HSS2	N/A	HSC2	N/A
HBS3	Good	HSS3	N/A	HSC3	N/A
HBS4	Good	HSS4	N/A	HSC4	N/A
HBS5	Bad	HSS5	N/A	HSC5	N/A
HBS6	Good	HSS6	N/A	HSC6	N/A
HBS7	Good	HSS7	N/A	HSC7	Good
HBS8	Bad	HSS8	Good	HSC8	Bad
HBS9	Bad	HSS9	Good*	HSC9	Bad
HBS10	Good	HSS10	Good*	HSC10	Good
HBS11	Good	HSS11	Good	HSC11	Bad
HBS12	Bad	HSS12	Bad	HSC12	N/A

*Not all data available.

Table C-4: Availability and Type of Data for CC3 Sensors

Sensor	Good/ Bad	Sensor	Good/ Bad	Sensor	Good/ Bad
ASG1	Bad	ASG13	Bad	ASG25	Bad
ASG2	Bad	ASG14	N/A	ASG26	Bad
ASG3	Bad	ASG15	Bad	ASG27	Bad
ASG4	Bad	ASG16	Bad	ASG28	Good
ASG5	Bad	ASG17	Bad	ASG29	Bad
ASG6	N/A	ASG18	Bad	ASG30	Bad
ASG7	Bad	ASG19	Good	ASG31	Bad
ASG8	Bad	ASG20	Good	ASG32	Bad
ASG9	Bad	ASG21	Good	ASG33	Good
ASG10	N/A	ASG22	Good	ASG34	Bad
ASG11	Bad	ASG23	Good	ASG35	Good
ASG12	N/A	ASG24	Bad	ASG36	Good

Table C-5: Availability and Type of Data for CC5 Sensors

Sensor	Good/ Bad	Sensor	Good/ Bad
ASG1	Good	ASG11	Bad
ASG2	Good	ASG12	N/A
ASG3	Bad	ASG13	Good
ASG4	Bad	ASG14	Bad
ASG5	N/A	ASG15	Bad
ASG6	Bad	ASG16	Bad
ASG7	Bad	ASG17	Good
ASG8	N/A	ASG18	Good
ASG9	Good	ASG19	Bad
ASG10	Good	ASG20	Good

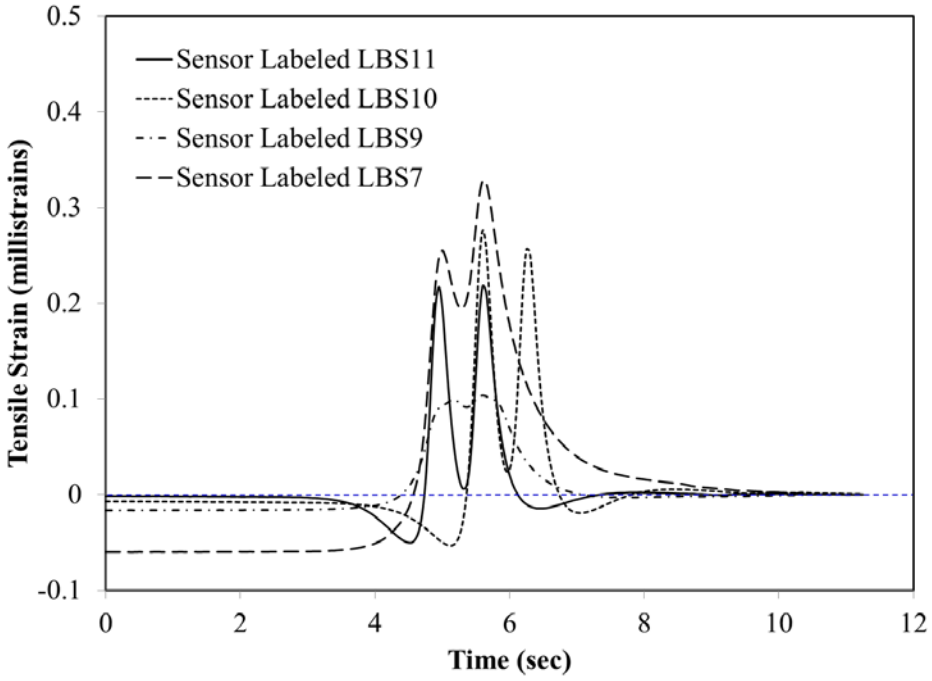

Figure C-1: Example of Good Data Obtained from CC1 Sensors at Loading Pass Number 3087

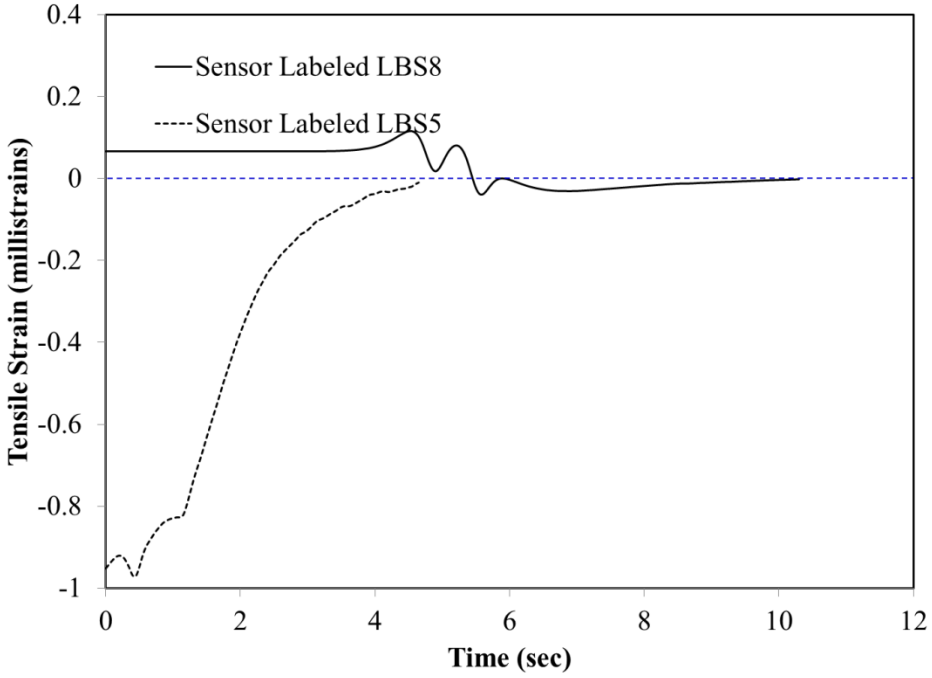

Figure C-2: Example of Bad Strain Data Obtained from CC1 Sensors at Loading Pass Number 3087

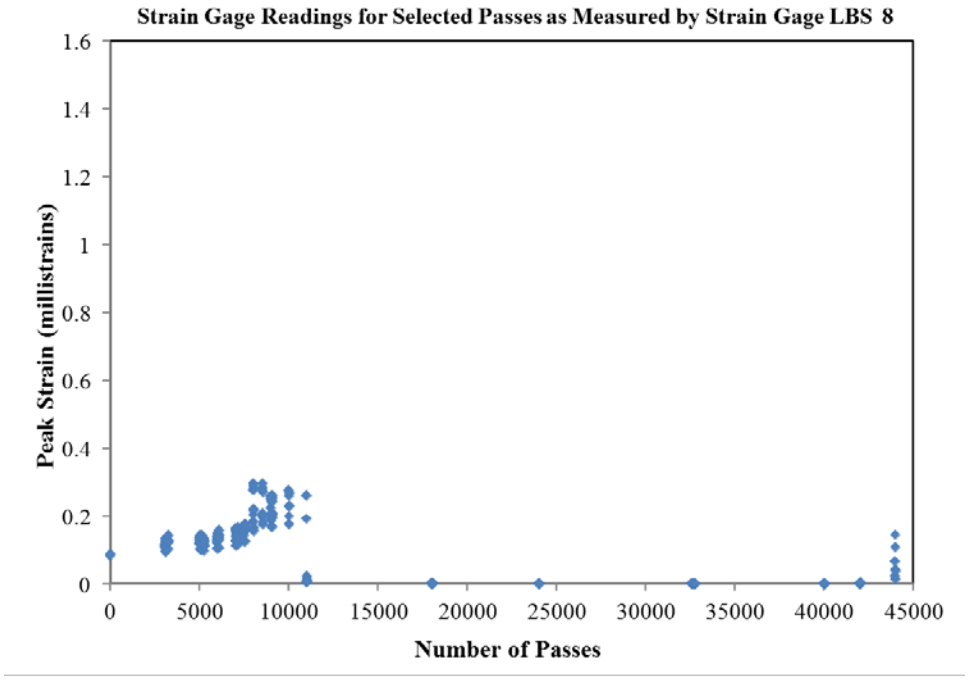

Figure C-3: Example of Bad Data Obtained due to Strain Gage Sensor Failure